THREE-AXIS FLEXIBLE TACTILE SENSOR ARRAY FOR PRESSURE AND SHEAR MAPPING

by

Rajesh Surapaneni

A dissertation submitted to the faculty of
The University of Utah
in partial fulfillment of the requirements for the degree of

Doctor of Philosophy

Department of Electrical and Computer Engineering

The University of Utah

December 2013

UMI Number: 3600310

All rights reserved

INFORMATION TO ALL USERS
The quality of this reproduction is dependent upon the quality of the copy submitted.

In the unlikely event that the author did not send a complete manuscript
and there are missing pages, these will be noted. Also, if material had to be removed,
a note will indicate the deletion.

UMI 3600310

Published by ProQuest LLC (2013). Copyright in the Dissertation held by the Author.

Microform Edition © ProQuest LLC.
All rights reserved. This work is protected against
unauthorized copying under Title 17, United States Code

ProQuest LLC.
789 East Eisenhower Parkway
P.O. Box 1346
Ann Arbor, MI 48106 - 1346

Copyright © Rajesh Surapaneni 2013

All Rights Reserved

The University of Utah Graduate School

STATEMENT OF DISSERTATION APPROVAL

The dissertation of **Rajesh Surapaneni**

has been approved by the following supervisory committee members:

Name	Role	Date Approved
Carlos Mastrangelo	, Chair	**08-09-2013**
Massood Tabib-Azar	, Member	**08-09-2013**
Darrin Young	, Member	**08-21-2013**
Stacy Bamberg	, Member	**08-09-2013**
Prashant Tathireddy	, Member	**08-09-2013**

and by **Gianluca Lazzi** , Chair/Dean of

the Department/College/School of **Electrical and Computer Engineering**

and by David B. Kieda, Dean of The Graduate School.

ABSTRACT

Tactile sensors are a group of sensors that are widely being developed for transduction of touch, force and pressure in the field of robotics, contact sensing and gait analysis. These sensors are employed to measure and register interactions between contact surfaces and the surrounding environment. Since these sensors have gained usage in the field of robotics and gait analysis, there is a need for these sensors to be ultra flexible, highly reliable and capable of measuring pressure and two-axial shear simultaneously. The sensors that are currently available are not capable of achieving all the aforementioned qualities.

The goal of this work is to design and develop such a flexible tactile sensor array based on a capacitive sensing scheme and we call it the flexible tactile imager (FTI). The developed design can be easily multiplexed into a high-density array of 676 multi-fingered capacitors that are capable of measuring pressure and two-axial shear simultaneously while maintaining sensor flexibility and reliability. The sensitivity of normal and shear stress for the FTI are 0.74/MPa and 79.5/GPa, respectively, and the resolvable displacement and velocity are as low as 60 μm and 100 μm/s, respectively. The developed FTI demonstrates the ability to detect pressure and shear contours of objects rolling on top of it and capability to measure microdisplacement and microvelocities that are desirable during gait analysis.

To Friends and Family

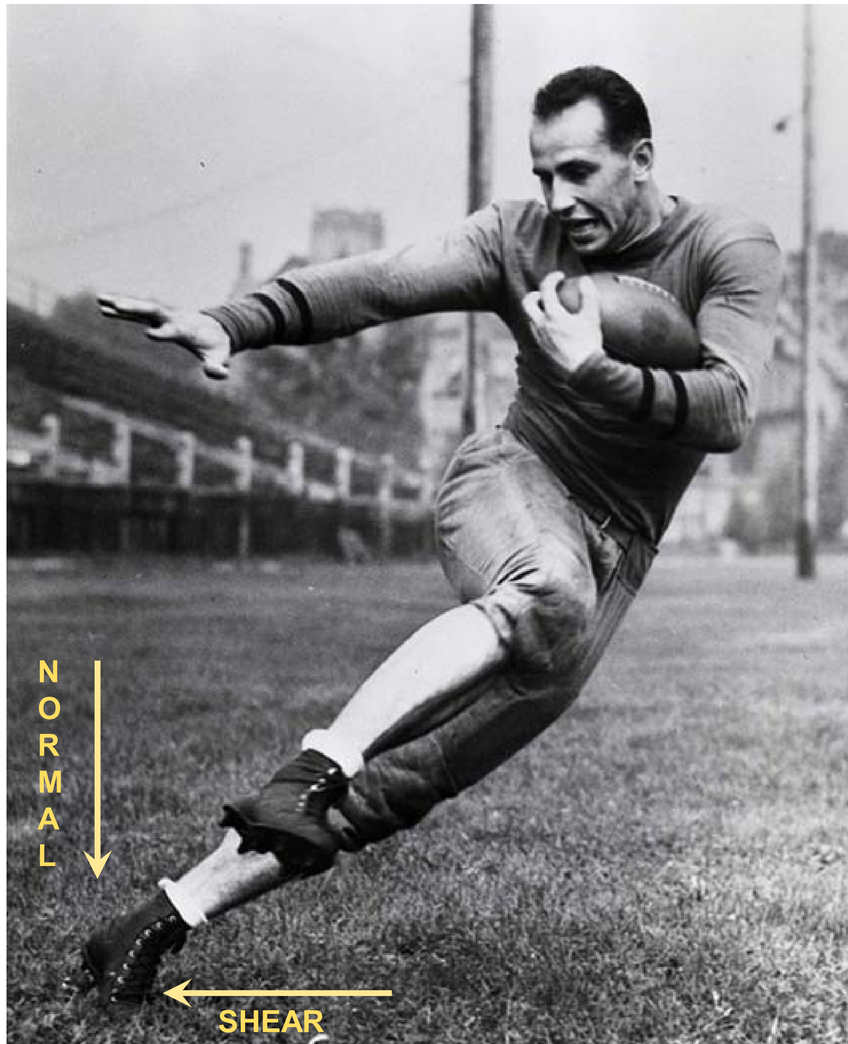

Image Courtesy: Department of Special Collections and University Archives, Marquette University Libraries

TABLE OF CONTENTS

ABSTRACT………………………………………………………………………. iii

ACKNOWLEDGEMENTS…………………………………………………………. ix

Chapters

1. INTRODUCTION…………………………………………………………….. 1

1.1 Tactile sensors...................……………………………………………… 1
1.2 Flexible tactile sensors……………………………………………….. 4
1.2.1 Resistive sensing scheme….……………………………………... 4
1.2.2 Capacitive sensing scheme……………………………………….. 11
1.2.2.1 Single axis tactile sensing…………………………... 11
1.2.2.2 Three axis tactile sensing………………………….... 17
1.2.3 Commercially available sensors……………………….……..... 22
1.3 Problem statement………………………………………………………... 23
1.3.1 Auxiliary sensor in pedestrian navigation.……………………..... 24
1.3.2 Gripping feedback in robotics……………………..…………..... 27
1.3.3 Gripping feedback in prostheses…………………..…………..... 28
1.4 Thesis overview………………………………………..………..... 29
1.5 References……………………………………..……………..... 31

2. A THREE-AXIS HIGH-RESOLUTION CAPACITIVE FLEXIBLE TACTILE IMAGER ………………………..………..…………………….. 38

2.1 Introduction……………………………………………………….……… 38
2.2 FTI design…………………………………………………….…….…..... 39
2.2.1 Simple design..………………………………………………… 39
2.2.2 Alternate cell arrangement design………………………….…... 43
2.3 FTI Fabrication………………………………………………………… 46
2.3.1 Conductive-polydimethylsiloxane (PDMS) electrodes on parylene substrate based on simple design…………………….. 46
2.3.2 Thin-film metallization on parylene substrate based on

simple design …… 52
2.3.3 Thin-film metallization on polyimide substrate based on alternative cell arrangement …… 55
2.4 Experimental setup…… 58
2.5 Results and discussion…… 58
2.6 FTI to readout circuitry packaging…… 62
2.7 Summary…… 62
2.8 References…… 63

3. HIGHLY SENSITIVE MULTIFINGERED CAPACITIVE FLEXIBLE TACTILE IMAGER …… 65

3.1 Introduction…… 65
3.2 Sensor design and fabrication…… 65
3.3 Results and discussion…… 76
3.4 FTI to readout circuitry packaging…… 77
3.5 Summary…… 80

4. A SELF-REPAIRING HIGH-RESOLUTION FLEXIBLE TACTILE IMAGER WITH LIQUID-METAL ELECTRODES…… 82

4.1 Introduction…… 82
4.2 Metallization issues…… 82
4.3 Sensor design and fabrication…… 85
4.4 Results and discussion…… 88
4.5 Summary…… 90
4.6 References…… 90

5. A HIGHLY RELIABLE FLEXIBLE TACTILE IMAGER WITH FLOATING ELECTRODE SCHEME…… 92

5.1 Introduction…… 92
5.2 Floating electrode scheme and proof-of-concept testing …… 93
5.3 FTI design …… 100
5.4 FTI fabrication…… 104
5.5 Readout circuitry…… 107
5.5 Object motion via centroid interpolation …… 110
5.6 Experiments and results…… 114
5.6.1 Normal stress measurement system…… 115
5.6.2 Shear stress measurement system…… 120
5.6.3 Testing during walk…… 125
5.7 Summary…… 126
5.8 References…… 129

6. CONCLUSION…… 131

Appendices

A. INSTRUCTIONS FOR EXPERIMENTAL SETUP………………………….. 135

B. PHIDGET STEPPER MOTOR CONTROLLER PROGRAM……….………. 147

C. PROGRAM FOR THE MICROCONTROLLER……….……….………..…… 152

Supplementary files

D. SOURCE FILES FOR CAPTURING AND DISPLAYING PRESSURE AND SHEAR CONTOURS……….……….……….…………….……….…. 155

E. SOURCE FILES FOR DISPLAYING PRESSURE CONTOURS WHILE CAPTURING VOLTAGE CHANGES CORRESPONDING TO BOTH PRESSURE AND SHEAR……….……….……….…………….……….….. 241

ACKNOWLEDGEMENTS

Sincere thanks to my advisor, Dr. Carlos Mastrangelo, for his support and guidance without which this work would not have been possible. I would like to thank Dr. Darrin Young for his useful comments and feedback on this research. I thank my committee members, Dr. Massood Tabib-Azar, Dr. Stacy Bamberg and Dr. Prashant Tathireddy, for their constant motivation. I would like to thank Dr. Renny Fernandez, Dr. Yan Xie, Dr Michel Suster and Qingbo Guo for their valuable suggestions and help. I will take this opportunity to thank DARPA for providing me with this interesting project. Thanks to Brian Baker and the lab staff at the Microfab of University of Utah for timely maintenance of the lab equipment despite me breaking them every now and then. My thanks goes to Lori Sather from the Electrical and Computer Engineering department for always welcoming me with a big smile on her face every time I go to her office. Special thanks to my best friends, Rohini Pantangi, Rohit Sharma, Tanya Abaya (and the list keeps going) and family, Rajeev Surapaneni, Sri Koduri, Chola Alluri and Deepthi Addala, for the constant blabbering they did in my ears (and of course for all the fun and emotional support). I thank all the locally brewed beers for the mental support provided during the preparation of this manuscript. Finally, I thank my beloved parents for everything.

CHAPTER 1

INTRODUCTION

1.1 Tactile sensors

The advancements in the field of microelectromechanical systems (MEMS) paved a path for design and development of microsensors. Tactile sensors are one such group of sensors that are widely being developed for transduction of touch, force and pressure in the field of robotics, contact sensing and gait analysis. Sensors that are employed to measure and register interactions between contact surfaces and the surrounding environment are called tactile sensors. Tactile sensors are used in a wide variety of applications from elevator buttons to measuring contact forces on gripping surfaces in robotics to sensors used in automobiles (brakes, door seals, seat belts detectors, automatic speed adjustment in windshield wipers). The early tactile sensors were realized using very large scale integration (VLSI) fabrication techniques, first described by Ralbert and Tanner in 1982 [1]. They proposed a 3 × 3 element impedance measuring electrode array realized on silicon substrate covered with a pressure-sensitive conductive rubber sheet. An applied pressure induced a compressive force on the conductive rubber, reducing the sheet resistance. This further reduced the resistance between adjacent electrodes. The sensor response to different pressures, however, was not discussed in the literature. A modified variant of this sensor was introduced in 1984 that was comprised of 6 × 8

sensor elements [2]. Each sensor element consisted of a non-pressure-sensitive conductive rubber removed in a triangular pattern over the metal electrodes. During the application of pressure, spatial progression of a contact front between the overlying rubber and the exposed electrodes varied depending on the amount of pressure applied. The measurements were not quite reproducible as the position of the contact front was not a repeatable function of applied stress.

The first three-axis tactile sensor was developed by Fan *et al.* in 1984 [3]. The design consisted of two metal layers separated by a deformable polymer realized on a silicon substrate. The planar bottom electrodes of the sensors are coated with a deformable polymer and another layer of metal is realized on top of the deformable polymer, such that the top electrode overlaps bottom electrodes forming parallel plate capacitors. The differential output of the capacitances from the two adjacent capacitors results in shear sensing. Many silicon-based tactile arrays were built after these initial efforts. Tactile sensors were built depending on the transduction scheme. Sensors have been used to determine surface textures [4-6] by estimating frictional properties during microslip at the point of contact. Curvature of objects and their shapes were measured by cylindrical tactile sensors and linear elastic tactile sensors [7-8]. Arrays were developed to identify edges, corners and holes using recognition algorithms [9-10]. In 1985, Kent Wise and his group from University of Michigan developed a capacitive sensing scheme with single crystal silicon [11-13]. The design implemented a high density of sensing elements (1024) with a pitch size of 0.5 mm. The element of the array was formed by bonding glass substrate to a layer of single crystal silicon (that has been selectively diffused by boron). The scheme gained popularity due to its ease of fabrication and multiplexing

architecture. Later various designs with composite layers of silicon were developed to realize a plate structure suspended above an insulated silicon layer forming capacitive elements [14-17].

Due to the piezoresistive characteristics of semiconductors, cantilever beams based on a piezoresistive sensing scheme were realized in silicon [18-20]. Both doped single crystal silicon and polysilicon-based strain gauges gained momentum due to their higher gauge factor compared to metal-based piezoresistive sensors. Furthermore, fabrication of these sensor elements was CMOS compatible [21-24]. In 1995, Kane *et al.* developed a sensor array realized in silicon wafer [25]. The sensor consisted of a central plate suspended on a micromachined pit by four piezoresistor-embedded bridge elements. Independent measurements of the four bridges provided three-axis stress information. An improved variant of this sensor array consisting of about 4100 sensors in about 2×2 cm^2 was developed in 2000 [26]. Figure 1.1 shows the fabricated stress-sensing element and its cross-sectional view design.

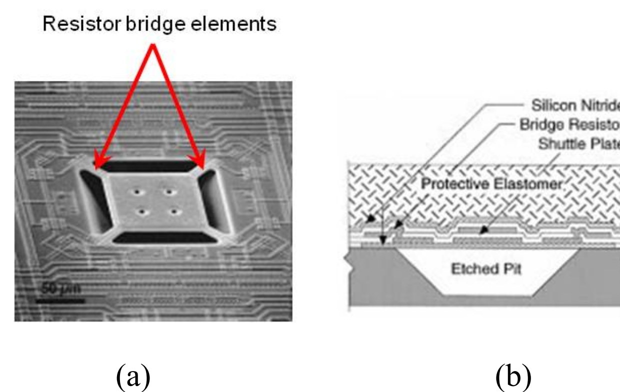

(a) (b)

Figure 1.1. Four resistor bridge elements. (a) Image of the fabricated stress-sensing element with four poly silicon resistor bridge elements. (b) Cross-sectional view of the element [26].

Emerging MEMS technology facilitated the development of silicon-substrate-based tactile sensors [1-26]. However, sensors and sensor arrays realized on silicon substrate have significant disadvantages. The sensors were unable to gain access to the contact points of nonuniform surfaces due to the substrate's rigidity. Furthermore, silicon posed sensor failure risks due to brittleness. This paved path to semiflexible substrates such as printed circuit boards (PCB) [27-28] and flexible substrates such as polyimide, parylene, silicones etc.

1.2 Flexible tactile sensors

Durable flexible mechanical sensors that can withstand millions of deformation cycles are needed in many harsh “rubber-meets-ground” type systems like robotic grippers, gait analysis and other contact/impact sensors [29-35]. Some of the common applications include robotic grippers, wearable sensor systems, impact, tactile and other proximity sensors. Flexible tactile sensors can be categorized into two groups based on the sensing scheme: resistive and capacitive sensing schemes. Sensors related to each of these sensing schemes are discussed in sections 1.2.1 and 1.2.2.

1.2.1 Resistive sensing scheme

The basis for the detection of stress in a resistive scheme is similar to the ones in silicon-based piezoresistive sensors. However, the doped silicon is replaced by flexible piezoresistive material. Initial transition from Si-based substrates to flexible substrates was a hybrid of both technologies. The sensor array developed by Kim *et al.* [36] makes use of the sensing elements that are fabricated by conventional bulk micromachining.

These elements are then assembled on a flexible PCB using epoxy adhesive. The sensing element is a set of four strain gauges arranged over a diaphragm. The diaphragm is formed by anisotropic wet etching of silicon using KOH solution. A bump (small cylindrical structure) is placed at the center of the diaphragm using SU-8 patterning. The bump layer facilitates three axis stress measurement. Depending on the direction of the stress, one or all of the strain gauges will show an output response. The fabricated sensing elements were then attached to the flexible PCB and electrically wire bonded to the metal on the flexible PCB below (see Figure 1.2). It is important to make sure the adhesive bond does not crack or suffer from creep for the proper functioning of sensor elements. This restricts the sensor performance due to lack of robustness.

A similar technique based on hybrid technology was developed by Beccai *et al.* in 2005 [37]. The micromachined silicon structure used by Beccai involved a complicated fabrication procedure despite its superior response to stress. SEM images of the structure and the sensing elements are shown in Figure 1.3 (a). A fabricated structure assembled with flexible PCB shown in Figure 1.3 (b) required nine readout lines per sensor. An array of these elements may results in very complicated readout circuitry and is highly undesired.

Nadvi in 2010 [38] developed a hybrid structure which involved spin-coatable nanocomposite using carbon nanotube (CNT) and polyimide on an aluminum oxide membrane for pressure-sensing application. Piezoresistive structures were formed by spin-coating CNT/polyimide nanocomposite and patterning the composite using reactive ion etching (RIE) and liftoff process on an aluminum oxide membrane. The nanocomposite piezoresistive structure is connected across a Wheatstone bridge network

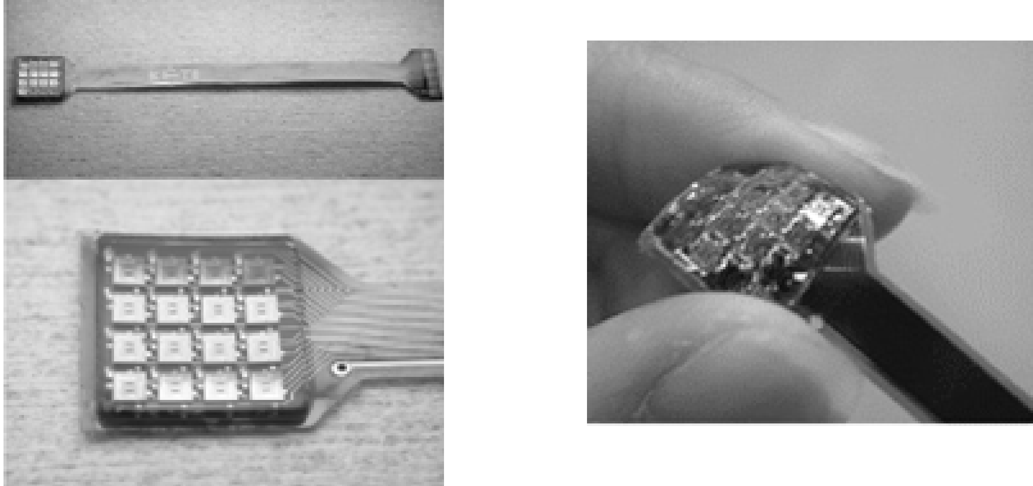

Figure 1.2. Images of the 4 × 4 sensor array assembled on a flexible PCB substrate [36].

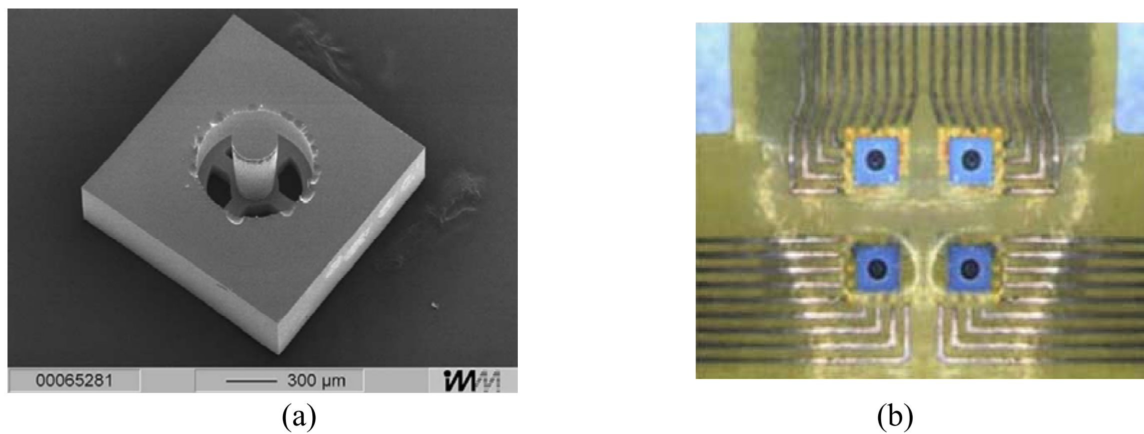

Figure 1.3. Micromachined silicon-based tactile sensor. (a) SEM of the fabricated device. (b) Assembled device consisting of nine readout lines per sensor [37].

to measure resistance. Under strain, the nanocomposite changes the resistivity and this information is translated to pressure applied on the membrane. The sensor was considered delicate due to the brittle nature of the aluminum oxide membrane and could be used to map low pressure ranges.

Unlike the hybrid methods which involves rigid substrates like silicon, the first piezoresistive tactile sensor array based solely on a polymer substrate was first introduced by Engel *et al.* in 2003 [39]. This fabrication technique involved lower processing temperatures (<350°C). Additionally, polymer substrate material not only improved robustness but also decreased fabrication costs and complexity. Due to the flexible nature of the sensor, it was able to form continuous and conformal tactile sensors (previously not possible with silicon-based sensors). The sensing element consisted of a bump layer and tensile/compression metal strain gauges embedded into the polyimide material. The bump layer was formed by curing polyimide in a silicon wafer mold. The strain gauges were realized by Ni-chrome alloy (NiCr, 80:20) deposition on the polyimide. Electrical interconnects were formed by Cr and Au deposition and patterning. The strain gauge embedded polymer tactile sensor (10 × 10) array was only 23 μm thick. The entire tactile structure was glued and flip-chip bonded to a flexible PCB with copper traces for device characterization. A variant of this sensor was developed in 2005 [40] where a patterned photoresist acted as bump layer and a cavity was formed by backside etching of the polymer.

In 2005, Engel *et al.* [41] also developed a tactile sensor than can measure both surface hardness and surface temperature using individual hardness sensing and temperature sensing elements. The developed sensor array formed artificial skin that

could measure both surface temperature and hardness of the environment in contact. Each sensing element consisted of a measured hardness sensor, reference hardness sensor, measured temperature sensor and reference temperature sensor. The temperature sensor incorporated a nickel resistance temperature device (RTD) and the hardness sensor incorporated Ni-chrome alloy metallization to form strain gauges. The testing of the sensor element was independently performed to measure hardness and temperature. The temperature dependence of piezoresistive material can be ignored due to the presence of a reference sensor.

Hwang *et al.* [42] in 2007 developed a three-axial resistive tactile sensor by implementing four thin metal strain gauges (Cu-Ni) on a polyimide and polydimethylsiloxane (PDMS) substrate. The devices were fabricated without the need for diaphragm-like structures. The bump layer formed by SU-8 photoresist, however, was critical for measurement of normal and shear stress. The bump layer was placed over the strain gauges such that when normal load was applied, all the strain gauges showed equal response. When there was an application of shear load, one of the strain gauges had expansion and the other contraction. The difference in the sensor output determined the amount of shear applied, as shown in Figure 1.4 (a). The number readout interconnects was proportional to the number of sensors and can get complex with a higher number of sensor elements, as shown in Figure 1.4 (b).

Kim *et al.* [43] in 2009 proposed the use of a multiplexing scheme to address individual sensor elements with a minimum number of readout interconnects. The fabrication involved complex steps to form a cavity in the structure. The fabrication is very similar to the one proposed by Engel *et al.* [39], the difference being the bump layer

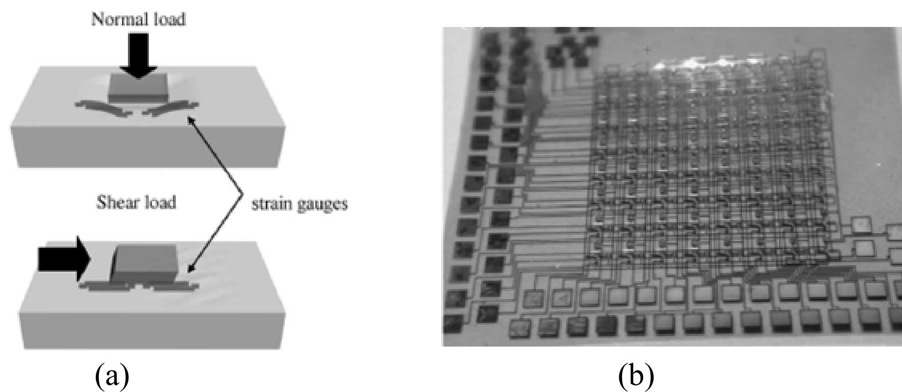

(a) (b)

Figure 1.4. A three-axial resistive tactile sensor. (a) Sensing principle for normal and shear loads applied on the sensor. (b) Fabricated tactile sensor array [42].

realization by UV epoxy instead of the use of a silicon mold. Finally, the UV epoxy is covered in a protective layer formed by PDMS. The fabricated sensor array consisted of 32 × 32 sensor elements and was assembled with the readout PCB. The sensors were, however, insensitive to shear stress.

In 2009, Jin developed a CNT strain sensor on a flexible polyimide substrate. A layer of CNT was first deposited on a donor wafer with SiO_2 using either a liquid-based spin-coating method or direct chemical vapor deposition (CVD) growth [44]. A polyimide was then spin-coated and cured on top of the CNT layer. Sacrificial etching of SiO_2 released the CNT/polyimide layer. An excimer laser photoablation process was performed to pattern via holes on the CNT/polymer layer to release mechanical stress in the layer. Metal contacts were realized on the either ends of the CNT/polymer layer. Under stress, the CNT mesh on the polymer experienced compression, increasing the electrical conductivity (due to increased contact area within the CNT mesh). The sensor was characterized under different applied stresses. Individual sensor elements were realized by this method and array characterization was not available.

Shimojo *et al.* [45] in 2004 developed a pressure-conductive rubber with stitched electrical wires. The material consisted of uniformly dispersed carbon particles in a silicone rubber matrix. Similar to a sensor developed by Jin [44], carbon particles are apart from each other in the matrix. As pressure was applied, the distance between the particles reduced, forming a chain of contacting CNTs increasing the conductivity. The conductivity depended on the amount of pressure applied on the material. Electrical wires of 0.125mm diameter made of beryllium copper (coated with gold) were stitched into the rubber material such that two interlaced wires were separated by the rubber, as shown in Figure 1.5. The resistance between the two wires reduces as pressure increased. The sensor formed arrays by such stitched interlaced wires of beryllium copper. Proper care should be taken to make sure the beryllium copper wire is not applying any stress on the rubber by default. These sensors could easily be multiplexed; however, they still were incapable of shear detection.

The resistive sensing scheme is the most widely used sensing scheme for tactile measurements; however, the capacitive sensing scheme has gained momentum due to the

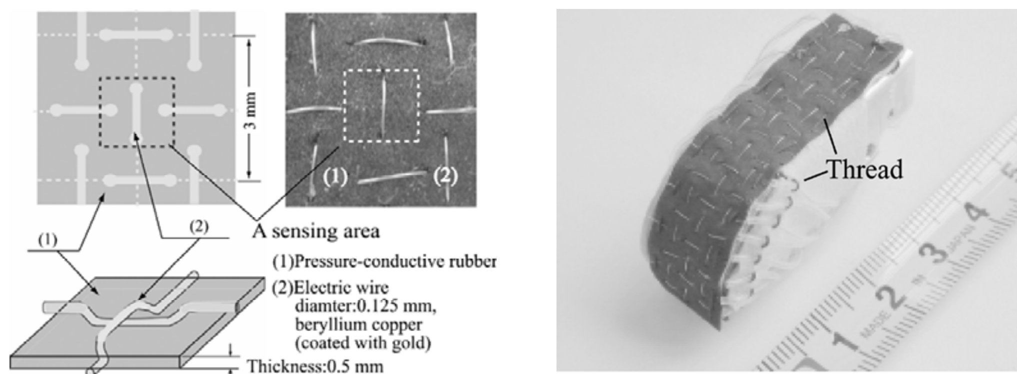

Figure 1.5. Schematic and image of sensing elements formed by stitched interlaced wires of beryllium copper [45].

advantage of ease of multiplexing individual sensors into arrays. Furthermore, the power consumption for the resistive sensing scheme is higher than that of capacitive sensing. The capacitive sensing scheme also exhibits zero standby power consumption and lower temperature dependence.

1.2.2 Capacitive sensing scheme

Capacitive tactile sensors have two or more electrodes separated by a compressible and elastomeric dielectric material [46-65]. Under an applied normal stress, the compression in the elastomeric dielectric causes a proportional change in capacitance. The capacitive tactile sensing scheme can be further divided into two groups: Single-axis tactile sensing (pressure or normal stress sensing), three-axis tactile sensing (pressure and two axial shear stress sensing).

1.2.2.1 Single axis tactile sensing

The first capacitive-based flexible tactile sensing array was developed in 1984 by Boie [46]. The array consisted of an 8×8 element array. Drive and sense electrodes (placed next to each other) were formed by conductive strips on a flexible printed circuit board (FPCB). An elastic dielectric material was bonded to the FPCB and the conductive strips were formed on top of the dielectric material by silk screening a conductive silicone rubber. These strips formed the floating electrodes of the sensor. When a load was applied on the sensor, the dielectric material deformed, changing the distance between the floating electrodes and the drive and sense electrodes. This in turn changed the capacitance value of the sensing element. An individual sensing element could be

probed by the analog multiplexers connected to the drive and sense electrodes. The schematic of a 6 × 6 element array is shown in Figure 1.6. This system provided greater robustness because the sensor output was insensitive to electrical breakage of the floating electrodes. Initial design of this sensor was used in [47-48] and sensor analysis was reported by Johnston *et al.* in [49].

Siegel *et al.* in 1987 [50] developed a parallel plate capacitor design using flexible material. Electrical traces were patterned by silk screening a conductive silicone rubber on either sides of an elastic dielectric material (insulating silicone rubber). The upper traces were placed perpendicular to the lower traces. Shielding layers were formed by enclosing the structure in layers of insulating silicone rubber. Detection of load was achieved by measuring the capacitance change due to compression of dielectric material in the sensor.

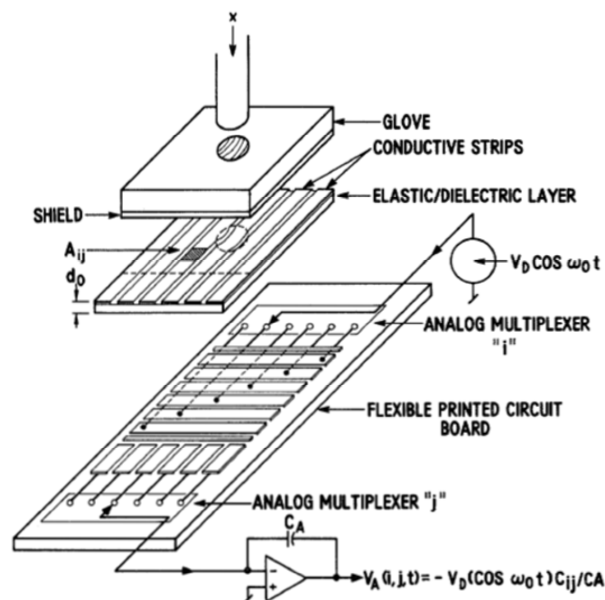

Figure 1.6. Schematic of 6 × 6 element array illustrating various layers [46].

Lee *et al.* [51-52] proposed and demonstrated a modular expandable 16 × 16 tactile sensor array using PDMS elastomer. The array was constructed with PDMS as the structural material and copper forming the metal traces of the parallel plate capacitor. A silicon wafer was spin-coated with sacrificial layer of lift-off resist (LOR 20B). Copper electrodes were then deposited by electroplating with patterned photoresist forming the electroplating mold. This was followed by deposition of titanium adhesion layer. PDMS was spin-coated and cured on top of the titanium layer and released by etching the sacrificial LOR layer. Insulation and spacer layers were formed by spin-coating n-hexane diluted PDMS on another Si wafer. The spacer layer was formed by etching PDMS using RIE process. The bump layer was formed by spin-coating PDMS on a KOH-etched silicon wafer. All the fabricated layers were aligned and bonded using oxygen plasma. The fabricated device and fabrication process are shown in Figure 1.7. The work demonstrated low crosstalk, reliable response and high spatial resolution.

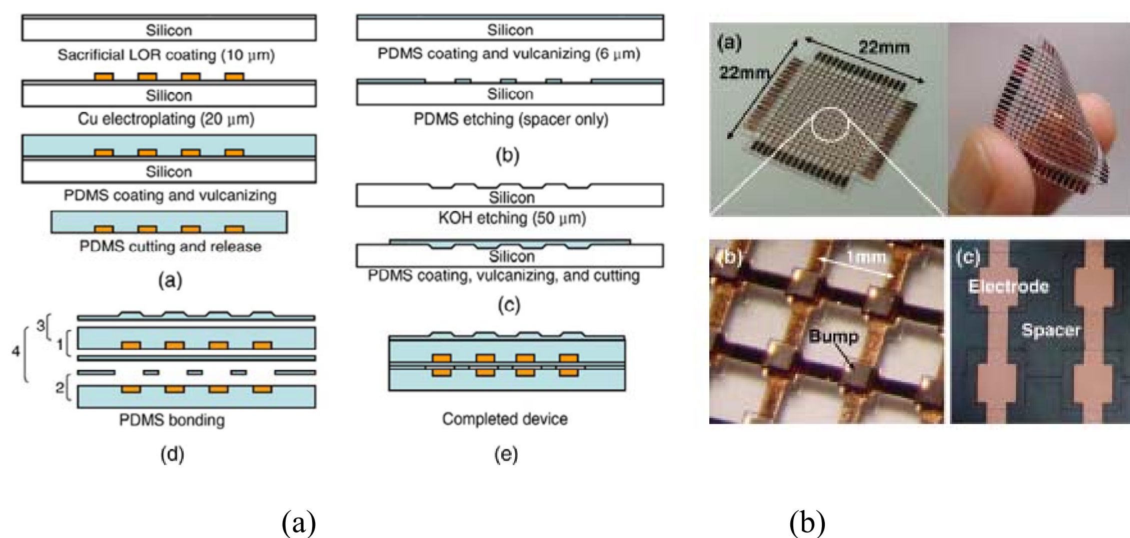

(a) (b)

Figure 1.7. A modular expandable tactile sensor array using PDMS elastomer. (a) Fabrication process flow for the sensing elements. (b) Fabricated array of sensor elements [52].

Lei *et al.* [53] proposed a simplified version of the Lee *et al.* [52] sensor element. The spacer layer is replaced by a thicker PDMS layer for two reasons: simplified fabrication (no need for RIE etching of PDMS) and higher dielectric constant of PDMS (since the dielectric constant of PDMS is higher than air, the nominal capacitance value of the sensor element is higher). Figure 1.8 shows the fabrication process flow of the modified sensor.

In 2006, Engel *et al.* [54] demonstrated a capacitive pressure sensor using conductive PDMS. Multiwalled carbon nanotubes (MWNT) were mixed in PDMS to form conductive PDMS (the nanotubes formed a matrix of conductive interconnects within PDMS). The fabrication of a conductive PDMS-based capacitive sensor was simple. A substrate was first spin-coated with photoresist and patterned. A mixture of PDMS with MWNT paste was applied and screen-printed (with the photoresist forming the mold). Photoresist was removed and a fresh layer of PDMS was spin-coated on top of the conductive PDMS layer. The structure was released from the substrate after curing of the

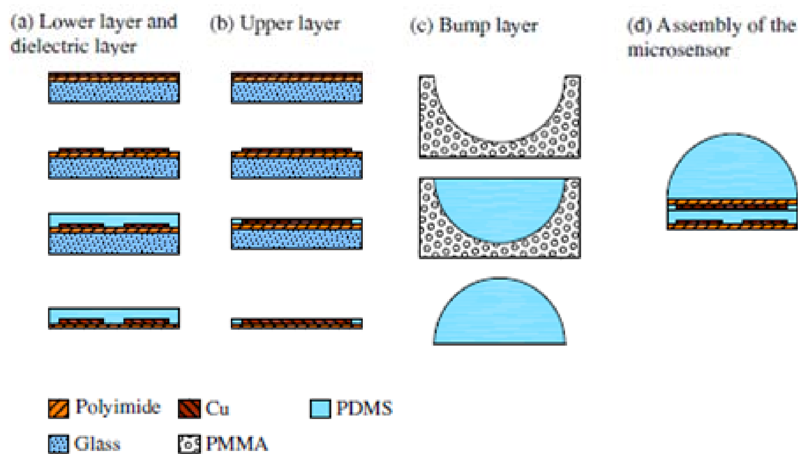

Figure 1.8. Fabrication process flow for the sensing element [53].

PDMS layer. Two such layers were bonded together orienting them orthogonal to each other to form a matrix of capacitive pressure sensors. The resistance of the conductive PDMS was in the order of hundreds of kOhms. High-speed electronics with this high resistance are difficult to build due to high RC time constant values.

Pritchard *et al.* in 2008 [55] developed a thin flexible capacitive pressure sensor array built on polyimide substrate. A flexible substrate formed by polyimide film with silicone adhesive was placed on a silicon wafer for structural support. A 150nm gold layer (with titanium seed layer) was deposited by evaporation and patterned by lift-off process (using a photoresist layer agitated in acetone). A dielectric layer (parylene-C) was deposited on top of the gold layer. Another layer of gold was deposited and patterned similar to the first layer. A protective polyimide layer was added over the sensing array, as shown in Figure 1.9. A parylene-C layer was etched at certain regions to expose bottom electrodes. Different sizes of sensing elements were fabricated and electrical characterization of the sensors was performed to detect applied pressure.

Fabrication of a wearable fabric tactile sensor with artificial hollow fibers was proposed by Hasegawa *et al.* in 2008 [56]. An artificial hollow fiber was formed by covering a single elastic hollow fiber with metal and insulation layers. The commercially available single elastic hollow fiber was first pretreated with argon and oxygen plasma to improve adhesion of the subsequent metal layer. A thin layer of gold was sputtered uniformly on the hollow fiber using modified equipment with rotating mechanism to spool the long fiber. A thin layer of parylene-C was deposited on top of the gold layer to form electrical insulation. The insulating layer was removed on either end of the long fiber to form electrical contacts. The artificial hollow fiber was woven into a fabric with

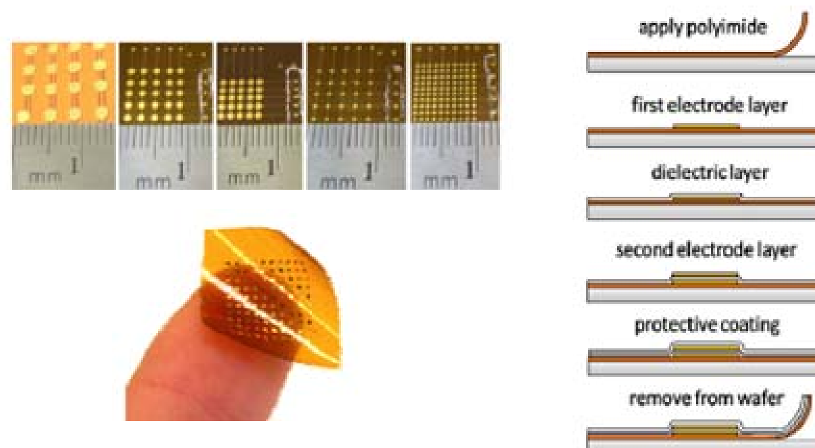

Figure 1.9. A thin flexible capacitive pressure sensor array built on polyimide substrate. (a) Images of fabricated devices of various dimensions. (b) Fabrication process flow [55].

intermittent cotton yarn fibers. As the fabric is normally loaded, the hollow fibers deform changing the capacitance between them. The authors demonstrated good sensor response to applied load.

A single sensing element based on PDMS embedded between two metal films was developed by Riedl *et al.* in 2010 [57]. A polyimide substrate with a copper metal layer formed the bottom electrode of the sensing element. Photoresist is spin-coated and patterned on the copper layer followed by spin-coating and curing of PDMS layer. The photoresist on the copper layer is dissolved using acetone. A thin layer of aluminum forming the top electrode is deposited on top of PDMS (after surface treating PDMS with oxygen plasma to avoid cracks in deposited metal). The cross-sectional view of the fabricated element is shown in Figure 1.10. The sensor demonstrated change in capacitance with applied static pressure.

In 2010, Mannsfeld *et al.* [58] developed a highly sensitive flexible pressure sensor with PDMS dielectric material. An 8 × 8 pixel pressure sensor pad consisted of a micro-

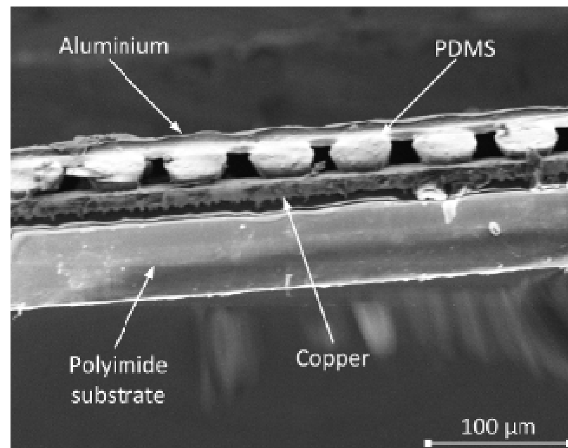

Figure 1.10. Cross-sectional SEM image of the fabricated device [57].

structured PDMS layer sandwiched between two poly ethyleneterephthalate (PET) sheets with eight vacuum-deposited aluminum metal lines. The microstructured PDMS is formed by curing PDMS on KOH-etched patterns in silicon wafer. The sensor showed excellent response to applied load.

1.2.2.2 Three-axis tactile sensing

The inability to sense multimodal tactile information by the single-axis sensing scheme has paved a path to the introduction of three-axis tactile sensing. Robotic gripping and manipulation of objects require multimodal tactile sensing for feedback of contact forces and dynamic slip sensing. Ground reaction sensors for gait analysis also require multimodal tactile sensing for detection of microvelocities as well as bearing changes. Recently, researchers have shifted focus on development of these multimodal tactile sensors.

A thin film five-electrode capacitive tactile normal/shear force sensor was first theoretically proposed by Chase *et al.* in 1995 [59]. Simultaneous measurement of pressure and shear using a single sensor element was demonstrated by this design. The sensing element consisted of a top electrode separated from the bottom electrodes by an elastic dielectric such as PDMS. The top electrode overlapped over the four bottom electrodes. When this structure was subject to normal pressure, the elastic dielectric compressed and capacitance on all four capacitors increased. When the same structure was subject to lateral shear stress, the top plate overlap may increase or decrease, as shown in the Figure 1.11. The vector shear strain and stress could be directly obtained by measuring the four capacitance values. This structure is simple and can measure both pressure and two-dimensional shear. Metal electrodes were patterned on flexible polyimide and a filler layer which forms the elastic dielectric material is sandwiched between the polyimide layers. The sensors were not actually fabricated; however, a

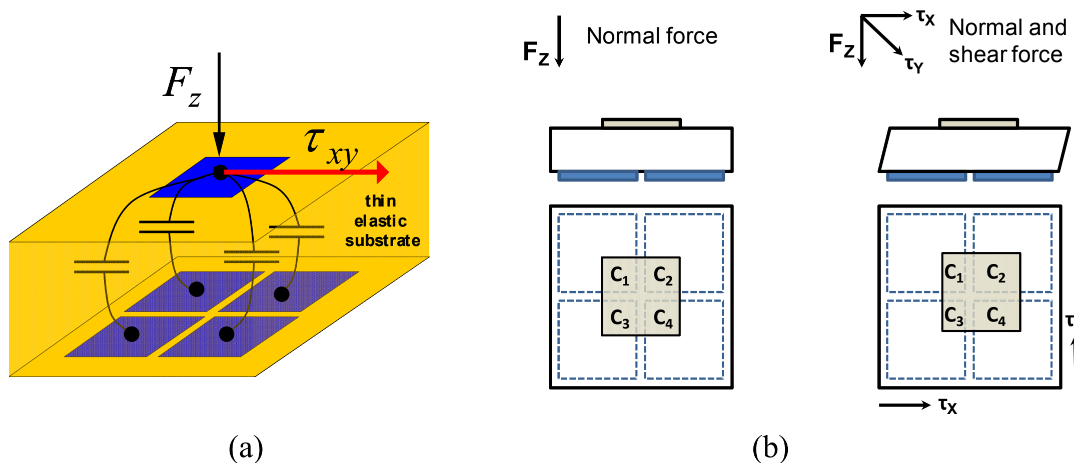

Figure 1.11. A five-electrode capacitive tactile sensor. (a) Schematic of the five-electrode configuration. (b) Operation principle of the sensing element [59].

fabrication process was proposed. Extensive analysis of this sensor was detailed in [60-61].

Lee *et al.* in 2008 [62] developed a three-axial tactile sensor array with multiple capacitors. Each sensing element consists of four parallel plate capacitors arranged as shown in Figure 1.12 (a). The operation principle of this sensing element is demonstrated in Figure 1.12 (b). The sensor construction is similar to the modular single axis tactile sensor developed by the same research group. First, a silicon wafer was spin-coated with a sacrificial layer of lift-off resist (LOR 20B). It is partially developed to form the pillar structure in the PDMS. Copper electrodes were then deposited by electroplating with patterned photoresist forming the electroplating mold. This was followed by deposition of a titanium adhesion layer. PDMS was spin-coated and cured on top of the titanium layer and released by etching the sacrificial LOR layer. The top metal layer is formed similarly without the pillar structure. Insulation and spacer layers were formed by spin-coating n-hexane diluted PDMS on another Si wafer. The spacer layer was formed by etching PDMS using the RIE process. The bump layer was formed by spin-coating PDMS on a KOH etched silicon wafer. All the fabricated layers were aligned and bonded using oxygen plasma. The sensor characterization was performed under different tactile forces in different axes. This sensor cannot measure if both normal and shear forces were simultaneously applied.

In 2010, Cheng *et al.* [63] developed a polymer-based capacitive sensing array for normal and shear force measurement using floating electrode implementation. The sensor element consisted of a pair of sensing electrodes with electrical interconnects patterned on a flexible polyimide substrate. The electrically isolated top floating electrodes

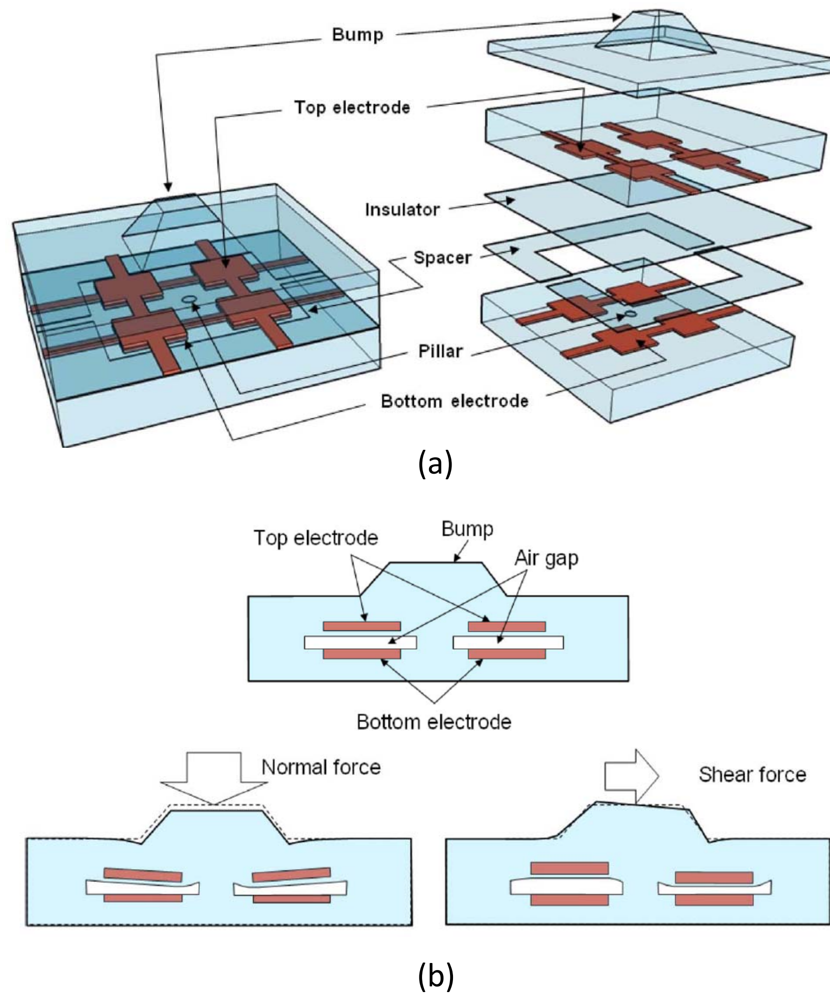

Figure 1.12. Multilayered three-axial tactile sensor. (a) An exploded view of the sensing element. (b) Demonstration of operating principle of the sensing element [62].

were patterned on PDMS. The top and bottom electrodes are separated by an insulating layer and a spacer layer (similar to the design in [52]). These electrodes form two parallel plate capacitors in series. A schematic (exploded view) of the sensor element is shown in Figure 1.13. The construction of the sensor element consisted of fabrication of three separate layers (PDMS bump layer, PDMS structure layer and FPCB layer) and assembling them together. First, PDMS is cured on top of a patterned SU-8 mold and then carefully peeled off. A thin chromium and gold layer are deposited on the PDMS

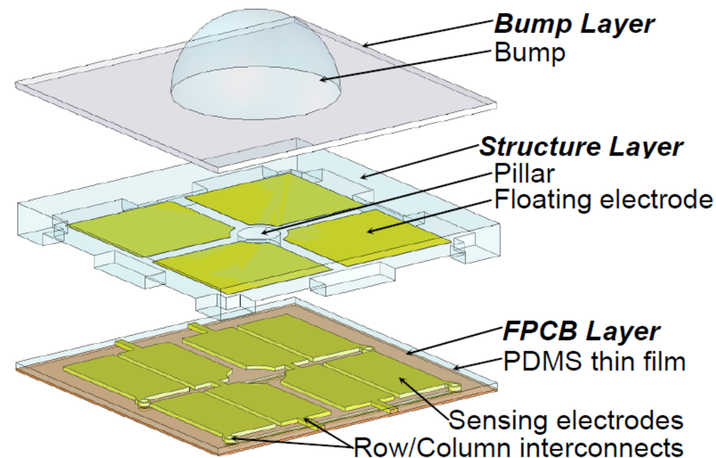

Figure 1.13. Exploded view of the sensing element [63].

structure using evaporation technique. The metal layers are patterned by using a steel mask to form the floating electrodes. The bump layer is formed by spin-coating PDMS in a PMMA mold (formed my CNC milling). The insulation layer was formed by spin-coating PDMS on another Si wafer. An FPCB layer was formed with patterned metal and implementation of via holes by standard FPCB manufacturing techniques. All three layers are bonded to each other using oxygen plasma treatment. The operating principle of this sensor is similar to the one demonstrated by Lee *et al.* [62]. This sensor also cannot measure pressure and shear when both are applied simultaneously.

Dobrzynska *et al.* in 2013 [64] developed a three-axial capacitive force sensor using a flexible polyimide substrate and PDMS as dielectric material. The sensor element consisted of a top and bottom multifingered structure that could detect pressure and two axial shear. The two metal layers formed four multifingered capacitors with a common top electrode. The top and bottom electrodes were aligned with slight off-set to implement the detection of shear. The sensor elements were fabricated on a silicon wafer for structural support and later released. A silicon wafer was first sputtered with a

tungsten-titanium alloy and then a layer of aluminum was deposited to form a sacrificial layer. A thin polyimide layer was then spin-coated and baked. The bottom electrodes were formed by depositing a Ti seed layer followed by platinum sputtering. The electrodes were patterned by dry etching. PDMS was then spin-coated and cured which formed the elastic dielectric. A thin parylene-C layer was deposited on the PDMS to avoid cracking of the subsequent metal layer during deposition. The top electrode was formed by deposition of a chromium and gold layer and patterning it using a lift-off process. Another layer of parylene-C is then deposited to form a protective layer. The fabricated sensor elements were assembled with a readout circuit. The sensor array consisting of 2 × 2 sensor elements was characterized with three-axial force measurements.

The selection of sensing scheme involves several tradeoffs. While both resistive and capacitive type sensors can be utilized to measure normal as well as shear stress, capacitive sensors have lower shear sensitivity than strain gauges [65]. On the other hand, strain gauges display a higher temperature coefficient than capacitors. In flexible tactile imagers (FTIs), dense arrays of these sensors are distributed over a contact region; therefore, the multiplexing of the readouts is critical. In high-density FTIs, capacitive sensors are preferred due to ease of multiplexing, zero standby power consumption and low temperature dependence readouts.

1.2.3 Commercially available sensors

A wide variety of pressure mapping systems are currently available in the market. Sensor systems from Tekscan [66] use pressure-sensitive ink for various applications

ranging from insole pads to mats for beds and automotive applications. Similarly, sensor systems that map pressure distribution during sitting and for gait analysis are developed by T&T Medilogic Medizintechnik GmbH [67]. On the other hand, sensors developed by companies like Xsensor [68] and Pressure Profile Systems, Inc., (PPS) [69] rely on a capacitive sensing scheme. Sensors systems from Pressure Profile Systems are used for tactile pressure measurements in robotic actuators for analysis of ergonomics and grasp pressure measurements. Sensors Products Inc. [70] offers similar tactile pressure mapping systems of various sizes and shapes for different applications.

Despite such a wide variety of products from these companies, there is no commercially available system that can measure three-axial pressure and shear stresses acting at a point of contact. Also, the tactile sensing systems developed by various research groups (discussed in the literature review) lack either one of the following features: sensor flexibility, sensor reliability or simultaneous detection of three-axial pressure and shear stresses.

1.3 Problem statement

The goal of this work is to design and fabricate a prototype tactile sensor system/FTI that is highly reliable, flexible and capable of simultaneously measuring three-axial normal and shear stresses. Various applications of these tactile sensors are discussed below.

1.3.1 Auxiliary sensor in pedestrian navigation

In the last decade, the Global Positioning Satellite (GPS)-based navigation system has become a ubiquitous technology for both military and commercial users, so much so that many critical applications have become highly dependent on it. However, GPS capabilities are not continuously available — they are highly susceptible to interference, jamming and line-of-sight constraints, especially in subterranean and urban environments such as tunnels and tall-enclosed building structures. Standalone inertial motion units (IMUs) consisting of an array of gyros and accelerometer have been traditionally used to navigate in these environments. The major limitation with IMUs is drift biases. As the position is derived by double integration of the acceleration vector, the presence of any drifts and offsets can result in very large integrated position errors. This problem has been particularly acute in miniature IMU systems that have very low mass. Typically, a miniaturized IMU produces errors in excess of 10% after a few minutes of use. For accurate navigation in these systems, corrections of the biases must be estimated using auxiliary velocity and bearing sensors. These auxiliary sensors determine the time when the ground velocity is zero and this technique is called the zero velocity updating technique (or zupting technique) [72-74]. Zero velocity can occur anywhere between the instance when the foot is flat and push off, as shown in Figure 1.14. The zero velocity points occurring between these instances of foot position need to be estimated with good accuracy to reduce the incurred biases in IMUs. Zero velocity points can be estimated by using commercially available step-corrected IMU and GPS navigation systems called dead reckoning modules (DRMs) which utilize accelerometers to detect the feet impact with the ground, but the measurements are not very precise [75-81]. This approximate

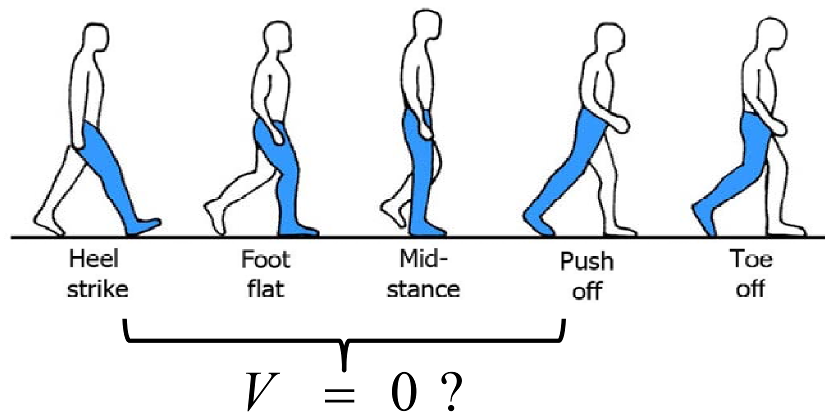

Figure 1.14. Different instances that occur during normal walk [82].

correction technique typically results in a 1-2% IMU positioning accuracy over a 30-min period, but it is limited by the ground velocity measurement resolution, which is poor because the step sensors are not in close proximity with the ground contact, and they also do not provide information on bearing changes.

In order to address these challenges for higher-resolution navigation, there is a need for high-resolution sensor array that we call ground reaction FTI (or GRFTI). The GRFTI can be considered a better approach than DRMs due to its ability to detect periods of zero velocity very accurately. The GRFTI should be located in close proximity to the ground contact and it independently needs to record dynamic ground forces, shear strains and sole deformation associated with ground locomotion *gait.* The GRFTI high-resolution biomechanical data can thus be readily used to detect periods of zero velocity very accurately, several times per second with speed resolution error as low as 50-100 μm/s. These zero velocity points provide a set of discrete velocity corrections (zupting) to the IMU that dramatically increase its effective positioning resolution [72-74]. For

navigation, pressure determination alone is insufficient as the GRFTI must be capable of sensing shear forces for determination of slippage and shoe rotation estimates. The pressure sensing elements of the GRFTI measure the distribution of ground reaction and the shear sensing elements measure lateral forces and torque (for estimation of bearing changes). From this information, the GRFTI can determine the ground contact line and its displacement to produce microvelocity estimates. Similarly, the shear information detects the slippage and intended direction of shoe rotation independent of angular velocity magnitude, as shown in Figure 1.15. This information can also be utilized to correct ineffective magnetic bearing estimates inside steel-supported building structures. The resolution required in the zero error bias is a direct function of GRFTI sensor pitch. The minimum detectable velocity (MDV) is given by

$$MDV = \frac{L}{N_s \cdot T_s} \tag{0.1}$$

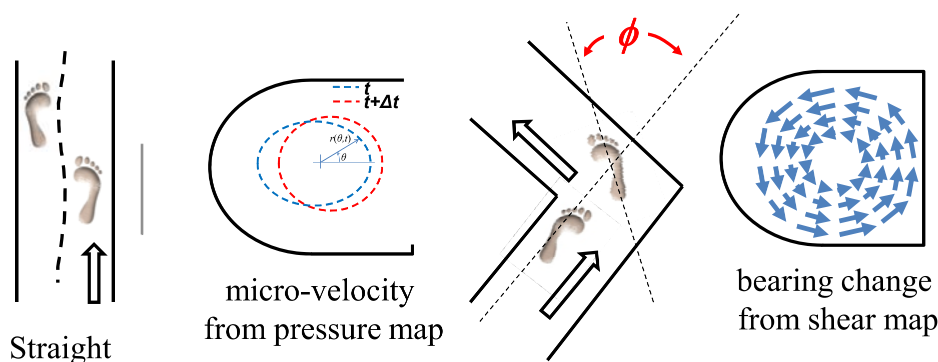

Figure 1.15. Dynamic pressure mapping results in microvelocities and dynamic shear mapping results in estimation of bearing changes during different walking instances [82].

where L is the sensor pitch, N_s and T_s are the sensor resolution or number of resolvable divisions and sampling time of the entire FTI readout. The sampling time is practically much less than the average time that the foot is on the ground during a regular walk (~100 ms). Hence, the MDV is reduced with a combination of either smaller pitch or a higher N_s or both. A more detailed analysis on the minimum detectable velocity is provided in Chapter 5. With these specifications in mind, the FTIs in the coming chapters have been designed and fabricated.

1.3.2 Gripping feedback in robotics

Long before the inception of humanoids, robots have been used in industrial purposes for the accomplishment of tasks such as handling and manipulating huge objects around the work floor. During such object handling tasks, robots required tactile feedback for better understanding of gripping and slippage. After the advent of humanoids, tasks such as gripping, holding or moving objects around and due to the need to handle delicate objects or human interaction, robotic tactile sensing has gained more importance. Recent research has found that dexterous robotic object manipulation can be possible with the introduction of flexible deformable grippers that mimic a human hand with deformable skin that can maintain more contact area and contact friction with objects [83]. In order to precisely manipulate a robotic arm, there is a need for a high-density, high-resolution tactile sensory system that can simultaneously measure both pressure and shear acting at the point of contact. This information will provide feedback on how hard or loose the object is held. This is very valuable when handling delicate objects such as wafers in a fabrication facility or handling glass objects at home by domestic humanoids [84]. In

addition to the pressure information, shear data will help the robots analyze the slippage of objects during gripping. Based on this information, the robotic arms can tighten or loosen grips. Hence, grip in a robotic arm involves simultaneous analysis of pressure and shear. Many research groups have been working on development of these tactile systems that can help robotic object manipulation. However, the tactile systems developed lack the ability to detect and measure pressure and shear simultaneously. Furthermore, the sensor systems are difficult to produce/fabricate because the periodic deformation during wear and tear can break their vital components such as metal interconnects after just a few hundred or thousand cycles.

1.3.3 Gripping feedback in prostheses

To overcome the limitations produced by amputation of limbs due to various injury-related or disease-related reasons, use of prosthetic devices have existed for centuries now (the earliest use, dating back to 300 BC). The aim of the prostheses was to bring back as much as functional capabilities as possible to the human in need. Similar to robotic gripping, prosthetic gripping need to fulfill tasks such as gripping, holding or moving objects around. In order to precisely manipulate a prosthetic limb, there is a need for a feedback system on gripping and slippage during holding objects or gait analysis during walking. For both these prosthetic needs, there is a requirement for a tactile sensor system that provides the brain with valuable pressure and shear information. For example, in the prosthetic arm as shown in Figure 1.16, one can use human thoughts to control the artificial limb. However, there is a need to understand the texture and hardness of the objects held. The sensor system can provide feedback on senses such as

Figure 1.16. Prosthetic arm with six motors to provide high degree of freedom developed by Todd Kuiken. Courtesy of the Rehabilitation Institute of Chicago (RIC).

touch, temperature and limb position [85]. The performance of these prosthetics can be improved many fold with the use of a advanced touch, gripping and slippage sensory system. The currently available technology cannot measure pressure and shear simultaneously similar to robotic manipulators. To cater to these needs, various FTI designs have been proposed and developed in Chapters 2, 3, 4 and 5.

1.4 Thesis overview

The goal of this work is to develop a flexible tactile imager that can simultaneously measure both pressure and two-axial shear acting at a point of contact using capacitive sensing scheme. To successfully achieve this imager system, we need to:

- **Develop highly reliable FTIs architectures** that can withstand a large number of deformation cycles during regular wear.
- **Develop low-cost fabrication methods for reliable FTIs** to achieve high volume production.
- **Develop a FTI testing station** that can characterize the developed FTI in terms of pressure and shear sensitivities.
- **Software development** for real-time data analysis with dynamic pressure and shear application on the FTI.

In this work, we present different design considerations, fabrication schemes and sensor characterization to achieve highly reliable FTIs. The developed FTI will be based on a capacitive sensing scheme and will make use of advanced microfabrication procedures. We also present the FTI integration with an in-house developed readout circuit to achieve in-depth FTI analysis. This thesis will go through the evolution of various design criteria to achieve both high pressure and high shear sensitivities, fabrication methods to make the FTI highly reliable and FTI characterization using testing stations and developed software tools.

This chapter has provided a in-depth overview of existing technologies and showcased the need for a system that can be incorporated in various applications discussed above in section 1.3.

Chapter 2 will provide an initial design scheme that will allow multiplexing sensor elements and accomplish measurements of both pressure and shear simultaneously. The chapter will also discuss various material evaluation for different fabrication schemes.

We will conclude the chapter with initial sensor element characterization using the developed testing stations.

Chapter 3 will evaluate the significant design modifications needed for the FTIs to achieve higher shear sensitivity. The chapter will also provide a comparison of improved sensitivities from the design modifications with the previous design.

Chapter 4 will focus on the fabrication of the proposed FTI that will make the sensor highly reliable using liquid metal scheme.

Chapter 5 will discuss both design and fabrication improvements made to achieve reliable FTIs using floating electrode scheme. This scheme will open avenues to low-cost fabrication of the FTIs. The chapter will also focus on FTIs integration with the readout circuits and characterization of individual sensor elements and well as entire FTIs.

Chapter 6 will conclude the work presented in this thesis by showing the possibilities and future modifications to shield the sensor from external parasitics and sensor damage. The chapter will also provide future trends in the application of the FTIs.

1.5 References

[1] Raibert M H and Tanner J E 1982 A VLSI tactile array sensor," *Proceedings of the 12th International Symposium on Industrial Robots*

[2] Raibert M H 1984 An all digital VLSI tactile array sensor *Proceedings of the 1984International Conference on Robotics* 314-19

[3] Fan L S, White R M, and Muller R S 1984 A mutual capacitive normal- and shear-sensitive tactile sensor *Technical Digest of the International Electron Devices Meeting* 220-22.

[4] Basu P R, Russell R A and Trott G 1988 Extracting 3-dimensional surface features from tactile data *Proceedings of the International Symposium and Exposition on Robots* 908-20

[5] Howe R D and Cutkosky M R 1989 Sensing skin acceleration for slip and texture perception *Proceedings of the 1989 IEEE International Conference on Robotics and Automation* 145-50

[6] Tremblay M and Cutkosky M R 1993 Estimating friction using incipient slip sensing during a manipulation task *Proceedings of the 1993 IEEE International Conference on Robotics and Automation* 429-34

[7] Fearing R S and Binford T O 1991 Using a cylindrical tactile sensor for determining curvature *IEEE Transaction on Robotics and Automation* **7** 806-17

[8] Nicolson E J and Fearing R S 1995 The reliability of curvature estimates from linear elastic tactile sensors *Proceedings of the 1995 IEEE International Conference on Robotics and Automation* 1126-33

[9] Chen N, Zhang H and Rink R 1995 Edge tracking using tactile servo *Proceedings of the 1995 IEEE/RSJ International Conference on Intelligent Robots and Systems*, 84-89

[10] Chen N, Rink R and Zhang H 1995 Efficient edge detection from tactile data *Proceedings of the 1995 IEEE/RSJ International Conference on Intelligent Robotics and Systems* 386-91

[11] Chun K J and Wise K D 1985 A capacitive silicon tactile imaging array *Digest of Technical Papers for the 1985 International Conference on Solid-State Sensors and Actuators, TRANSDUCERS '85* 22-25

[12] Suzuki K, Najafi K and Wise K D 1990 A 1024-element high-performance silicon tactile imager *IEEE Transactions on Electron Devices* **37** 1852-60

[13] DeSouza R J and Wise K D 1997 A very high density bulk micromachined capacitive tactile imager *Digest of Technical Papers for the 1997 International Conference on Solid-State Sensors and Actuators, TRANSDUCERS '97* 1473-76

[14] Wolffenbuttel R F and Regtien P P L 1989 Integrated tactile imager with an intrinsic contour detection option *Sensors and Actuators* **16** 141-53

[15] Wolffenbuttel M R and Regtien P P L 1990 Design considerations for a silicon capacitive tactile cell," *Sensors Actuators A* **A24** 187-90

[16] Rey P, Charvet P, Delaye M T and Abou Hassan S 1997 A high density capacitive senor array for fingerprint sensor application *Digest of Technical Papers for the 1997 International Conference on Solid-State Sensors and Actuators, TRANSDUCERS '97* 1453-56

[17] Chu Z, Sarro P M and Middelhoek S 1995 Silicon three-axial tactile sensor *Digest of Technical Papers of the 1995 International Conference of Solid State Sensors and Actuators, TRANSDUCERS '95* **1** 656-59

[18] Oki A K and Muller R S 1986 Integrated polysilicon tactile sensor *Technical Digest of the IEEE Solid State Sensors Workshop*

[19] Yao C T, Peckerar M C, Wasilik J H, Amazeen C and Bishop S 1987 A novel three-dimensional microstructure fabrication technique for a triaxial tactile sensor *Proceedings of the IEEE Micro Robotics and Teleoperators Workshop* 1-6

[20] Middelhoek S and Audet S A 1989 *Silicon Sensors,* New York, NY, Academic Press of Harcourt Brace Jovanovich

[21] Sugiyama S, Kawahata K, Yoneda M and Igarashi I 1990 Tactile image detection using a 1k-element silicon pressure sensor array *Sensors Actuators* A **22** 397-400

[22] Litian L, Xinyu Z and Zhijian L 1993 An array tactile sensor with piezoresistive single-crystal silicon diaphragm *Sensors Actuators* A **35** 193-96

[23] Wang L and Beebe D J 1998 Silicon-based tactile sensor for finger-mounted applications *IEEE Trans. Biomed. Eng.* **45** 151–59

[24] Wang L and Beebe D J 2000 A silicon-based shear force sensor: Development and characterization *Sensors Actuators* A **84** 33–44

[25] Kane B J, Cutkosky M R and Kovacs G T A 1995 CMOS compatible traction stress sensor for use in high resolution tactile imaging *Digest of Technical Papers of the 1995 International Conference of Solid State Sensors and Actuators, TRANSDUCERS '95* **1** 163-66

[26] Kane B J, Cutkosky M R and Kovacs G T A 2000 A traction stress sensor array for use in high- resolution robotic tactile imaging *J. Microelectromech. Syst.* **9** 425–34

[27] Yamada Y and Cutkosky M R 1994 Tactile sensor with 3-axis force and vibration sensing functions and its applications to detect rotational slip *Proceedings of the 1994 IEEE International Conference on Robotics and Automation* **4** 3550-57

[28] Domenici C, de Rossi D, Bacci A and Bennati S 1989 Shear stress detection in an elastic layer by a piezoelectric polymer tactile sensor *IEEE Transactions on Electrical Insulation* **24** 1077-81

[29] Lumelsky V J, Shur M S and Wagner S 2001 Sensitive skin *IEEE Sensors J.* **1** 41–51

[30] Lee M H 2000 Tactile sensing: New directions, New challenges *Int. J. Rob. Res.* **19** 636–43

[31] Yamada D, Maeno T and Yamada Y 2002 Artificial finger skin having ridges and distributed tactile sensors used for grasp force control *J. Robot. Mechatron.* **14** 140–46

[32] Lee M H and Nicholls H R 1999 Tactile sensing for mechatronics—A state of the art survey *Mechatronics* **9** 1–31

[33] Rebello K J 2004 Applications of MEMS in surgery *Proc. IEEE* **92** 43–55

[34] Preising B, Hsia T C and Mittelstadt B 1991 A literature review: Robots in medicine *IEEE Eng. Med. Biol. Mag.***10** 13–22

[35] Brett P N and Stone R S 1994 A tactile sensing technique for automatic gripping of compact shaped non-rigid materials *IEEE Colloq. Intell. Autom. for Process. Non-Rigid Products* 1–5

[36] Kim K, Lee K R, Kim Y K, Lee D S, Cho N K, Kim W H, Park K B, Park H D, Park Y K, Kim J H and Pak J J 2006 3-Axes flexible tactile sensor fabricated by Si micromachining and packaging technology *Micro Electro Mechanical Systems, 2006. MEMS 2006 Istanbul. 19th IEEE International Conference on* 678-81

[37] Beccai L, Roccella S, Arena A, Valvo F, Valdastri P, Menciassi A, Chiara M Carrozza and Dario P 2005 Design and fabrication of a hybrid silicon three-axial force sensor for biomechanical applications *Sensors Actuators* A **120** 370-82

[38] Nadvi G 2010 MEMS piezoresistive pressure sensor on flexible susbtrate using nichrome and CNT/polyimide nanocomposities *Thesis The University of Texas at Arlington*

[39] Engel J, Chen J and Liu C 2003 Development of polyimide flexible tactile sensor skin *J. Micromech. Microeng.* **13** 359-66

[40] Kim S H, Engel J, Liu C and Jones D L 2005 Texture classification using a polymer-based MEMS tactile sensor *J. Micromech. Microeng.* **15** 912-20

[41] Engel J, Chen J, Fan Z and Liu C 2005 Polymer micromachined multimodal tactile sensors *Sensors Actuators* A **117** 50-61

[42] Hwang E-S, Seo J-H and Kim Y-J 2007 A polymer-based flexible tactile sensor for both normal and shear load detections and its application for robotics *J. Microelectromech. Syst.* **16** 556–63

[43] Kim K, Lee K R, Kim W H, Park K-B, Kim T-H, Kim J-S and Pak J J 2009 Polymer-based flexible tactile sensor up to 32 × 32 arrays integrated with interconnection terminals *Sensors Actuators* A **156** 284-91

[44] Jin H 2009 Carbon nanotube strain sensors with wide dynamic range fabrication on flexible substrates by novel processing techniques *Thesis University of Illinois at Urbana-Champaign*

[45] Shimojo M, Namiki A, Ishikawa M, Makino R and Mabuchi K 2004 A tactile sensor sheet using pressure conductive rubber with electrical-wires stitched method *IEEE Sensors Journal* **4** 589-96

[46] Boie R A 1984 Capacitive impedance readout tactile image sensor *Proc. IEEE Int. Conf. Robotics and Animation.* **1** 370-78

[47] Jacobsen S C, Iversen E K, Knutti D F, Johnson R T and Biggers K B 1986 design of the Utah/MIT dexterous hand *Proc. IEEE Int. Conf. Robotics and Animation.*1520-32

[48] Jacobsen S C, McCammon I D, Biggers K B and Phillips R P 1988 Design of tactile sensing systems for dexterous manipulators *IEEE Control Systems Magazine* **8** 3-13

[49] Johnston D, Zhang P, Hollerbach J and Jacobsen S 1996 A full tactile sensing suite for dexterous robot hands and use in contact force control *Proc. IEEE Int. Conf. Robotics and Automation* **4** 3222–27

[50] Siegel D M, Drucker S M and Garabieta I 1987 Performance analysis of a tactile sensor *Proc. IEEE Int. Conf. Robotics and Automation* **4** 1493-99

[51] Lee H K, Chang S I, Kim K H, Kim S J and Yoon E 2005 A modular expandable tactile sensor using flexible polymer *MEMS'05: 18th IEEE Int. Conf. on Micro Electro Mechanical Systems* 642–45

[52] Lee H K, Chang S I and Yoon E 2006 A flexible polymer tactile sensor: fabrication and modular expandability for large area deployment *J. Microelectromech. Syst.* **15** 1681–86

[53] Lei K F, Lee K-F and Lee M-Y 2012 Development of a flexible PDMS capacitive pressure sensor for plantar pressure measurement *Microelectronic Eng.* **99** 1-5

[54] Engel J M, Chen N, Ryu K, Pandya S, Tucker C, Yang Y and Liu C 2005 Multi-layer embedment of conductive and non-conductive PDMS for all-elastomer MEMS *Solid State Sensors, Actuators and Microsystems workshop* 316-19

[55] Pritchard E, Mahfouz M, Evans B, Eliza S and Haider M 2008 Flexible capacitive sensors for high resolution pressure measurement *IEEE Sensors 2008* 1484-87

[56] Hasegawa Y, Shikida M, Ogura D, Suzuki Y and Sato K 2008 Fabrication of a wearable fabric tactile sensor produced by artificial hollow fiber *J. Micromech. Microeng.* **18** 085014

[57] Riedl X, Bolzmacher C, Wagner R, Bauer R and Schwesinger N 2010 A novel PDMS based capacitive pressure sensor *IEEE Sensors 2010* 2255-58

[58] Mannsfeld S C B, Tee B C K, Stoltenberg R M, Chen C V H H, Barman S, Muir B V O, Sokolov A N, Reese C and Bao Z 2010 Highly sensitive flexible pressure sensors with microstuctured rubber dielectric layers *Nature Mater.* **9** 859–64

[59] Chase T A and Luo R C 1995 A thin-film flexible capacitive tactile normal/shear force array sensor *IECON'95: Proc. IEEE 21st Int. Conf. on Industrial Electronics, Control, and Instrumentation* **2** 1196–01

[60] Santos R F, Rocha P F, Lanceros-Mendez S, Santos C and Rocha J G 2005 3 Axis capacitive tactile sensor *ISIE: Proc. IEEE Int. Symp. Industrial Electronics* **4** 1539–44

[61] Rocha J G, Santos C, Cabral J M and Lanceros-Mendez S 2006 3 Axis capacitive tactile sensor and readout electronics *IEEE Int. Symp. on Industrial Electronics* **4** 2767–72

[62] Lee H K, Chung J, Chang S I and Yoon E 2008 Normal and shear force measurement using a flexible polymer tactile sensor with embedded multiple capacitors *J. Microelectromech. Syst.* **17** 934–42

[63] Cheng M Y, Lin C L and Yang Y J 2010 Tactile and shear stress sensing array using capacitive mechanisms with floating electrodes *MEMS'10: IEEE 23rd Int. Conf. on Micro Electro Mechanical Systems* 228–31

[64]] Dobrzynska J A and Gijs M A M 2013 Polymer-based flexible capacitive sensor for three-axial force measurements *J. Micromech. Microeng.* **23** 015009

[65] Shan J H, Mei M, Sun L, Kong D Y, Zhang Z Y, Ni L, Meng M and Chu J R 2005 The design and fabrication of a flexible three-dimensional force sensor skin *IEEE/RSJ Int. Conf. on Intelligent Robots and Systems* 1818–23

[66] http://www.tekscan.com/sensor-technology/

[67] http://www.medilogic.com/en/home/

[68] http://www.xsensor.com/pressure-imaging/pressure-imaging/

[69] http://www.pressureprofile.com/

[70] http://www.sensorprod.com/index.php/

[71] Lin K L and Jain K 2010 Design and fabrication of large-area, redundant, stretchable interconnect meshes using excimer laser photoablation and in situ masking *Adv. Packag. IEEE Trans.* **33** 592–01

[72] Foxlin E 2005 Pedestrian tracking with shoe-mounted inertial sensors *Computer Graphics and Applications, IEEE* **25** 38-46

[73] Stirling R *et al.* 2003 An Innovative Shoe-Mounted Pedestrian Navigation System *Proc. European Navigation Conf.* (GNSS), CDROM, Austrian Inst. of Navigation, 2003.

[74] Brand T and Phillips R 2003 Foot-to-Foot Range Measurement as an Aid to Personal Navigation *59th Institute of Navigation Annual Meeting.* Albuquerque, NM.

[75] Kim J, Lee J-G and Sung T K 1996 Compensation of gyroscope errors and GPS/DR integration *Proc. IEEE Position Location and Navigation Symposium,, IEEE 1996* 464-470

[76] Zhou Z, Chen X and Zhang T 2005 The principle of non-sensor dead reckoning *Proc. IEEE Geosience and Remote Sensing Symposyim* 4693-96

[77] Kao W-W 1991 Integration of GPS and dead reckoning navigation systems *Proc. IEEE Vehicule Navigation and Information Systems Conference* 635-43

[78] ZSazonov E S, Bumpus T, Zeigler S and Marocco S 2005 Classification of plantar pressure and heel acceleration patterns using neural networks *Proc. IEEE Neural Networks Conference* 3007-10

[79] Randell C, Djialis C and Muller H 2005 Personal position measurement using dead reckoning *Proc. Intl. Wearable Computing Symp.* 166-73

[80] Ojeda L and Borenstein J 2006 Non-GPS navigation for emergency responders *International Joint Topical Meeting: "Sharing Solutions for Emergencies and Hazardous Environments* February 12-15, 2006, Salt Lake City, Utah, USA

[81] Ojeda L and Borenstein J 2007 Non-GPS navigation with the personal dead reckoning system *SPIE Defense and Security Conference, Unmanned Systems Technology IX*, Orlando, Florida, April 9-13, 2007, pp. 1-11

[82] Surapaneni R, Park K, Suster M A, Young D J and Mastrangelo C H 2011 A highly sensitive flexible pressure and shear sensor array for measurement of ground reactions in pedestrian navigation *Transducers'11: 16th Int. Solid-State Sensors, Actuators and Microsystems Conf.* pp 906–09

[83] Matei Ciocarlie A M 2005 Grasp Analysis Using Deformable Fingers *Thesis New York, NY: Department of Computer Science, Columbia University*

[84] Adee S 2008 Dean Kamen's" Luke Arm" Prosthesis Readies for Clinical Trials *IEEE Spectrum 2 (2008)*

[85] Yu S 2007 To Arms. *Retrieved 2010, from Northwestern Magazine: http://www.northwestern.edu/magazine/winter2007/feature/kuiken.html*

CHAPTER 2

A THREE-AXIS HIGH-RESOLUTION CAPACITIVE FLEXIBLE TACTILE IMAGER

2.1 Introduction

Three-axial tactile sensing can be achieved by either resistive or capacitive sensing schemes. Capacitive sensing schemes for tactile force measurements at the point of contact have gained more prominence over resistive type sensing, due to their ability to multiplex an array of sensors without complex circuitry.

An FTI uses arrays of flexible capacitor cells, similar to the five-electrode capacitor cell configuration, discussed by Someya *et al.*, 2004 and Rocha *et al.*, 2006 [1-2] that are sensitive to normal and shear stress. The top central electrode in this five-electrode capacitor cell configuration is placed over an elastic dielectric material with four bottom electrodes. When normal force alone is exerted over the top electrode, the elastic dielectric material is compressed, leading to an increase in the capacitance between the top and the four bottom electrodes equally. However, the change in capacitance varies among the bottom electrodes when there is a combination of normal and shear forces. The five electrode capacitor cell configuration does not permit the implementation of a multiplexed high-density sensor array because it requires four parallel wires per row and one per column. Furthermore, there is a need for an additional metal layer using ‘via’

holes connecting all four bottom electrodes of individual cells in a column. From a given sensor layout with NxM (col)x(rows) capacitor cells, the number of electrical connections required is N+4M connections. The factor of 4 in the number of rows is excessive and precludes the fabrication of a practical high-density array. In order to minimize these connection requirements, we propose the use a six electrode configuration (discussed in this chapter) which can be multiplexed easily. This new type of cell can be read using 2N+2M connections. To illustrate the difference that this makes, we consider the following example. Let us consider an array of 1600 sensors (40 × 40). Multiplexing the five-electrode cell requires 200 wires.

2.2 FTI design

The FTI design proposed in this section comprises a simple design and an alternate cell arrangement (modified version of the simple design). In the simple design, the bottom electrodes of each cell in a column are connected to two sense lines in a similar fashion. In the alternate cell arrangement, the bottom electrodes of alternate cells are flipped when connecting to the sense lines. This is explained in detail below.

2.2.1 Simple design

The FTI consists of an array of 169 unit cells arranged in 13 × 13 matrix configuration materialized using Ledit (V.15) software. Each unit cell of the FTI measures 4.3 × 4.1 mm^2 and consists of six electrodes configured into two top electrodes and four bottom electrodes, as shown in Figure 2.1. The top electrodes form the drive lines and the bottom electrodes form the sense lines of the capacitors.

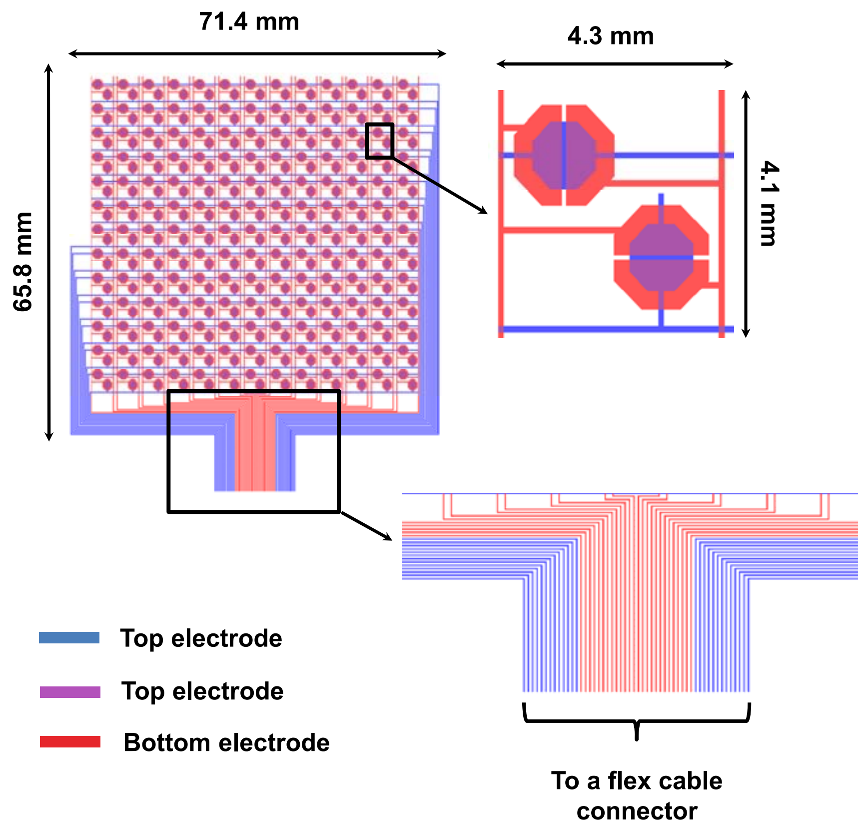

Figure 2.1. L-edit layout of the entire FTI array and individual sensing cell. The electrical connections to the top electrodes in each row and the bottom electrodes in a column are placed such that it can be connected to a flex cable connector.

A pair of bottom electrodes (represented in 'red', Figure 2.1) and a top electrode (represented in 'blue', Figure 2.1), separated by an elastomeric dielectric, forms a half-cell namely X-cell and Y-cell (consisting of two capacitors per half-cell). Each half-cell can measure shear stress in only one direction in addition to the normal stress. X-cells and Y-cells are placed orthogonal to each other such that shear vector can be obtained during load application. When a half-cell is subjected to a uniaxial shear stress, the capacitance of one of the capacitors increases while the other decreases. Hovever, under a uniform normal stress, both the capacitance values in the half-cell increases.

The readout electronics developed by Suster in 2010 [3] can measure a capacitance of 0.1-2.5pF and hence the size and shape of each half-cell is chosen such that the capacitance output is around 1pF. The nominal capacitance C_N of a capacitor is given by the equation (2.1):

$$C_N = \varepsilon_o \varepsilon_r \frac{A}{t} \tag{2.1}$$

where, ε_o is the permittivity of air , ε_r is the dielectric constant of the elastic dielectric material, t is the thickness of the dielectric material and A is the equivalent of half the area of the top electrode. PDMS (Sylgard-184, Dow Corning, USA) was chosen as the elastic dielectric material due to its low Young's modulus [4-10]. Lower Young's modulus helps achieve higher change in capacitance for a given normal load compared to parylene-based dielectric material [11-12]. Furthermore, PDMS demonstrated no permanent deformation during load application [7-8,10]. The dielectric constant of PDMS (ε_r) is 2.65, t is the thickness of the PDMS (considering 15 µm) and A is the equivalent of half the area of the top electrode with diameter 1.2 mm. Substituting these values in equation (2.1), the calculated nominal capacitance is 884 fF.

The two orthogonal half-cells are interrogated using a dual row select, dual column readout multiplexing scheme as reported in [3], as there is no overlap of connectivity of any same-axis capacitors along the vertical direction. This reduces the number of required connections to the array, which in turn increases the density of cells in the FTI. The capacitance value of the each of the capacitors in a half-cell can be measured by individually driving the 'blue' lines (A, B), while sensing on the vertical red lines (C, D),

as shown in Figure 2.2. The 'blue' drive lines connect all the top electrodes in a row, while the 'red' sense lines connect all the bottom electrodes in a column. All the 'red' and 'blue' lines are designed to form a flex cable, as shown in Figure 2.1. The flex cable thus can be connected to a flex cable connector on the readout circuit. Figure 2.3 shows a uniaxial three-terminal half-cell representation and its equivalent circuit (where C_{AC}, C_{AD} are capacitances of each of the capacitors in the half-cell). The capacitor sum in a half-cell (C_{AC}+C_{AD}) yields to the detection of normal stress, while the capacitor difference (C_{AC}-C_{AD}) yields the shear stress.

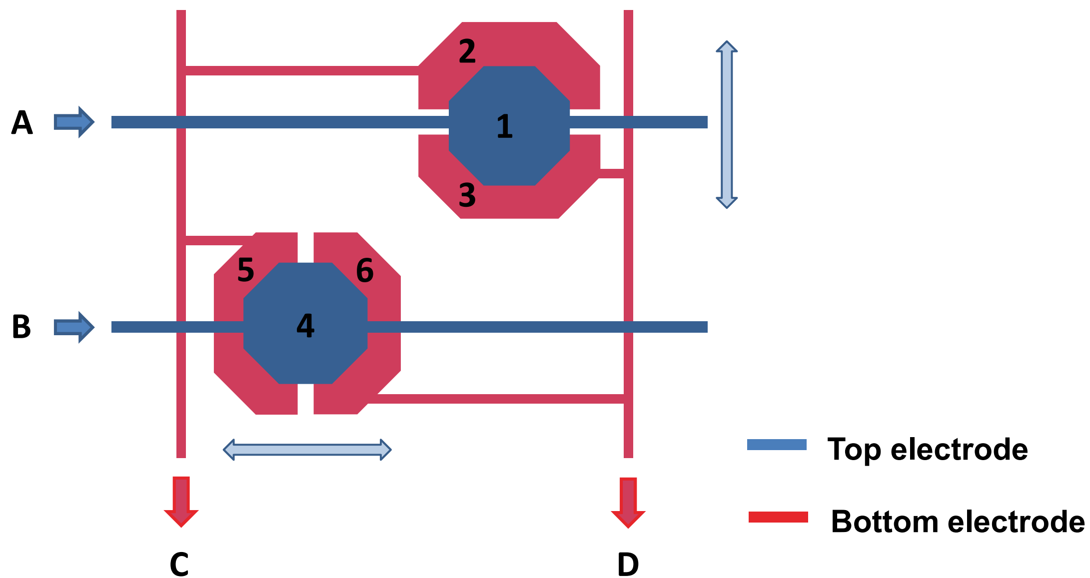

Figure 2.2. Design of a sensing scheme in a cell. The capacitance between electrodes '1' and '2' can be measured by driving line 'A' and sensing it through line 'C'. Similarly, the capacitance between electrodes '1' and '3' can be measured by driving line 'A' and sensing it through line 'C'. Capacitors '1', '2' and '1', '3' can measure shear only in the vertical direction (represented by the arrow beside the capacitors) whereas capacitors '4', '5' and '4', '6' can measure shear only in the horizontal direction (represented by the arrow below the capacitors).

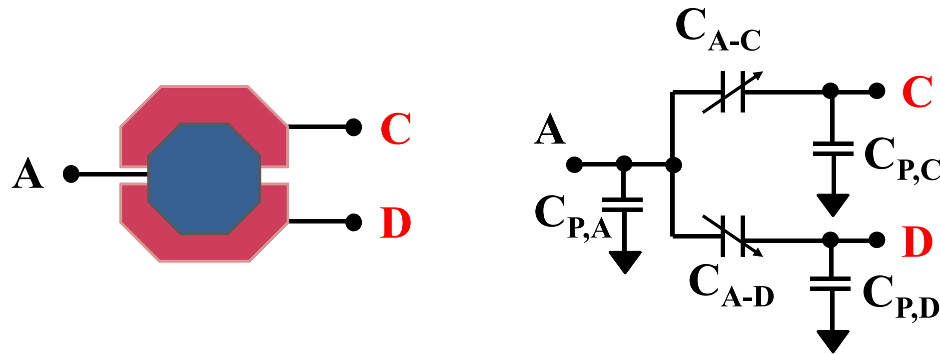

Figure 2.3. Uniaxial three-terminal two capacitor representation and its equivalent circuit. $C_{P,A}$, $C_{P,B}$ and $C_{P,C}$ are the parasitic capacitances associated with the terminals A, C and D, respectively, and $C_{A\text{-}C}$ and $C_{A\text{-}D}$ are the capacitances between terminals A, C and A, D, respectively.

2.2.2 Alternate cell arrangement design

The design of the FTI is slightly modified to reduce the parasitic mismatch. Since the readout circuit developed by Suster *et al*. [3] uses a differential circuit to read the half-cells, parasitic capacitance mismatch between the differential sensor electrodes causes ground noise interference to couple to the signal output, thus reducing FTI resolution. Noise interference ($V_{n1\text{-}2}$) between the parasitic capacitance ground and reference capacitor ground, as shown in Figure 2.4, limits the output dynamic range and thus the FTI resolution. The updated FTI design with alternating connections (shown in Figure 2.5) results in well-matched parasitic capacitance, minimizing the ground noise interference. Maximum output signal $V_{out,max}$ and output noise due to ground interference V_{on} are given by (2.2) and (2.3):

$$V_{out,\max} = \frac{\Delta C_{s,\max}}{C_I} V_s \tag{2.2}$$

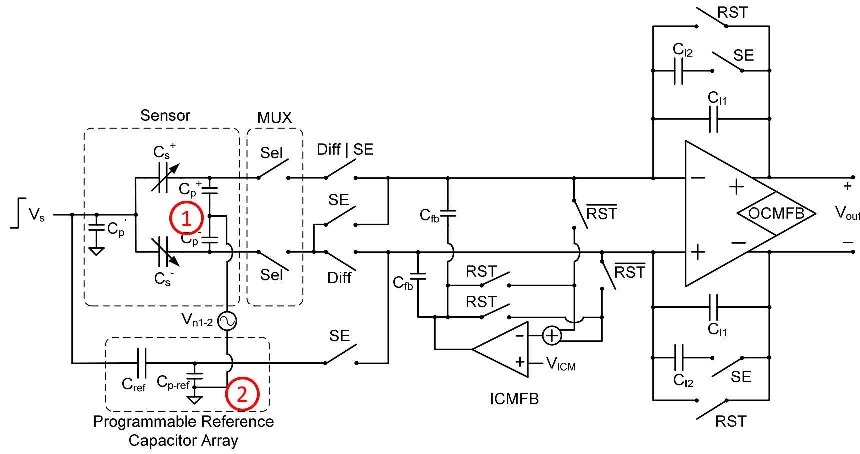

Figure 2.4. Charge amplifier design for the FTI interface [3].

$$V_{on} = \frac{C_p^{\ +} - C_p^{\ -}}{C_I} V_{n1-2} = \frac{\Delta C_p}{C_I} V_{n1-2} \tag{2.3}$$

where $\Delta C_{s,max}$ is the maximum capacitance change, C_I is the integrating capacitance, V_s is the stimulation voltage, C_p^{+} and C_p^{-} are the parasitic capacitances associated with the selected half-cell and ΔC_p is the change in the parasitic capacitances. From equation (2.3), it is evident that the effect of ground interference is directly related to parasitic capacitance mismatch. All the C_p^{+} for each individual X-cell and Y-cell of a column are connected to electrode e_2 and similarly C_p^{-} for each individual X-cell and Y-cell of a column are connected to electrode e_1 as shown in Figure 2.6. When the FTI is subjected to a large shear force, there will be a large difference of parasitic capacitance between electrodes e_1 and e_2. This will result in a large parasitic capacitance mismatch and thus an imbalance in the readout circuit. To overcome this mismatch, alternate cells in the columns are connected to electrodes e_1 and e_2 as shown in Figure 2.5. This will help

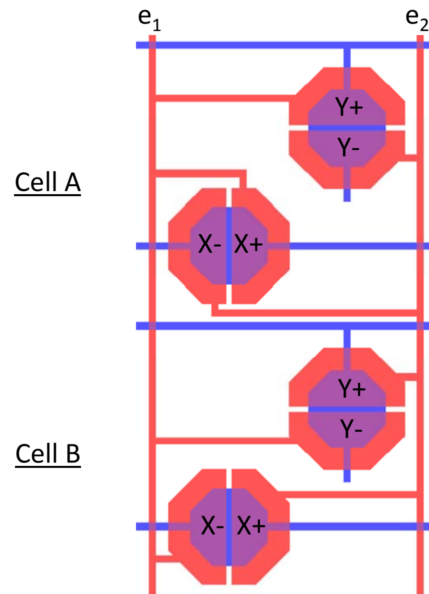

Figure 2.5. Adjacent cells of a column are alternately connected to electrodes e_1 and e_2. Parasitic capacitance on each electrode due to this arrangement is 6X+, 6X-, 6Y+, 6Y-.

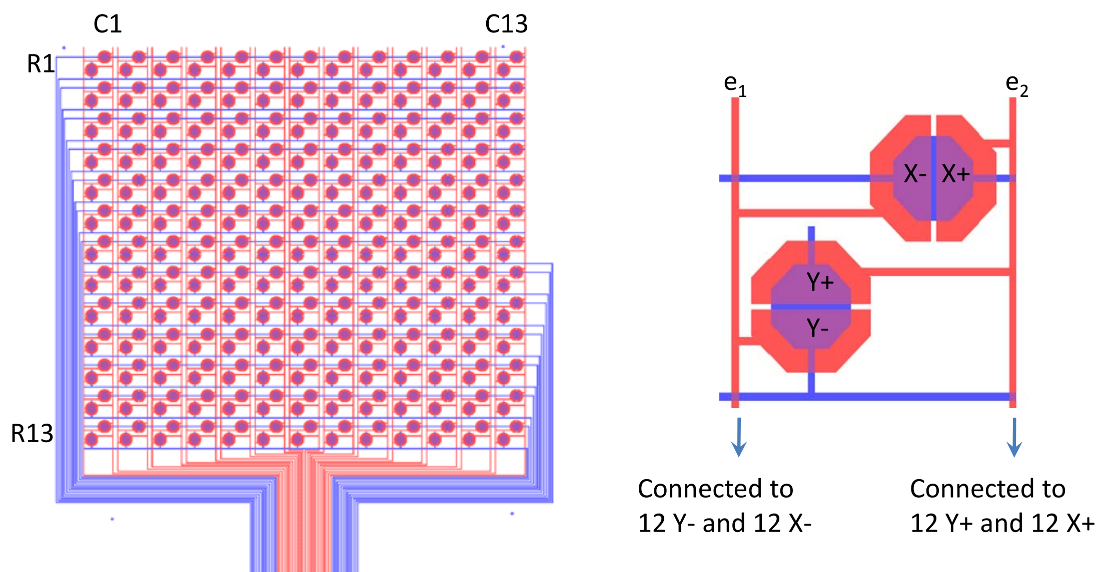

Figure 2.6. FTI layout representing columns C to C13 and rows R1 to R13. Parasitic capacitance on electrode e_1 will be 12 X- and 12 Y-, since all 12 consecutive 'minus' of the column are connected to e_1. Similarly, parasitic capacitance on electrode e_2 will be 12 X- and 12 Y+, since all the 12 consecutive 'plus' of the column are connected to e_2.

reduce the parasitic capacitance mismatch in each sensing column. The symmetry of connections attenuates parasitic capacitance mismatch by reducing the effect of ground interference during large shear force application on the FTI.

2.3 FTI fabrication

Various fabrication methods have been interrogated to achieve an array of flexible sensors. These fabrication methods are discussed below.

2.3.1 Conductive-polydimethylsiloxane (PDMS) electrodes on parylene substrate based on simple design

The first step for flexible sensor fabrication is choosing a flexible substrate. This flexible substrate, however, needs a rigid support for fabrication steps such as spin-coating layers of polymers. A parylene-C layer as a flexible substrate can be deposited on a rigid Si wafer for structural support. Due to the absence of parylene adhesion promoter (AZ-174), parylene does not adhere to the Si-wafer. This helps in easy separation of the parylene substrate from the Si wafer after device fabrication (from Figure 2.7, it is evident that parylene-C layer can be easily peeled off the Si surface).

Figure 2.8 shows a simplified FTI fabrication process flow. Firstly, a 5 µm thick parylene-C layer is coated on a 5” Si wafer using PDS 2010 parylene coater (Specialty Coating Systems, USA). A 2 µm thick layer of positive photoresist PR 1813 (Shipley, USA) is spin-coated (2000 rpm for 45 s) and patterned. A mixture of 5% weight/weight multiwalled carbon nano-tubes (MWCNT) and PDMS Sylgard-184 (Dow Corning, USA) [13] is applied on the patterned photoresist using screen-printing technique. This forms

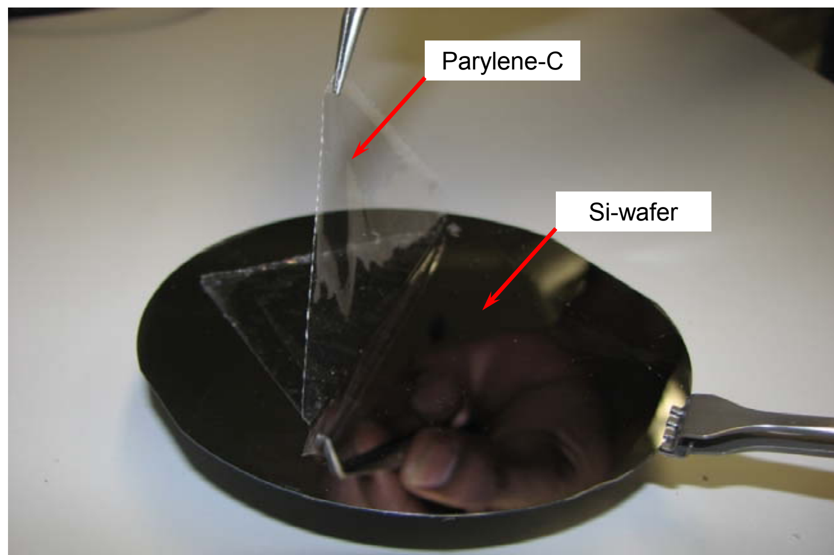

Figure 2.7. Parylene-C layer separation from wafer showing no issues of adhesion or tear during peel-off.

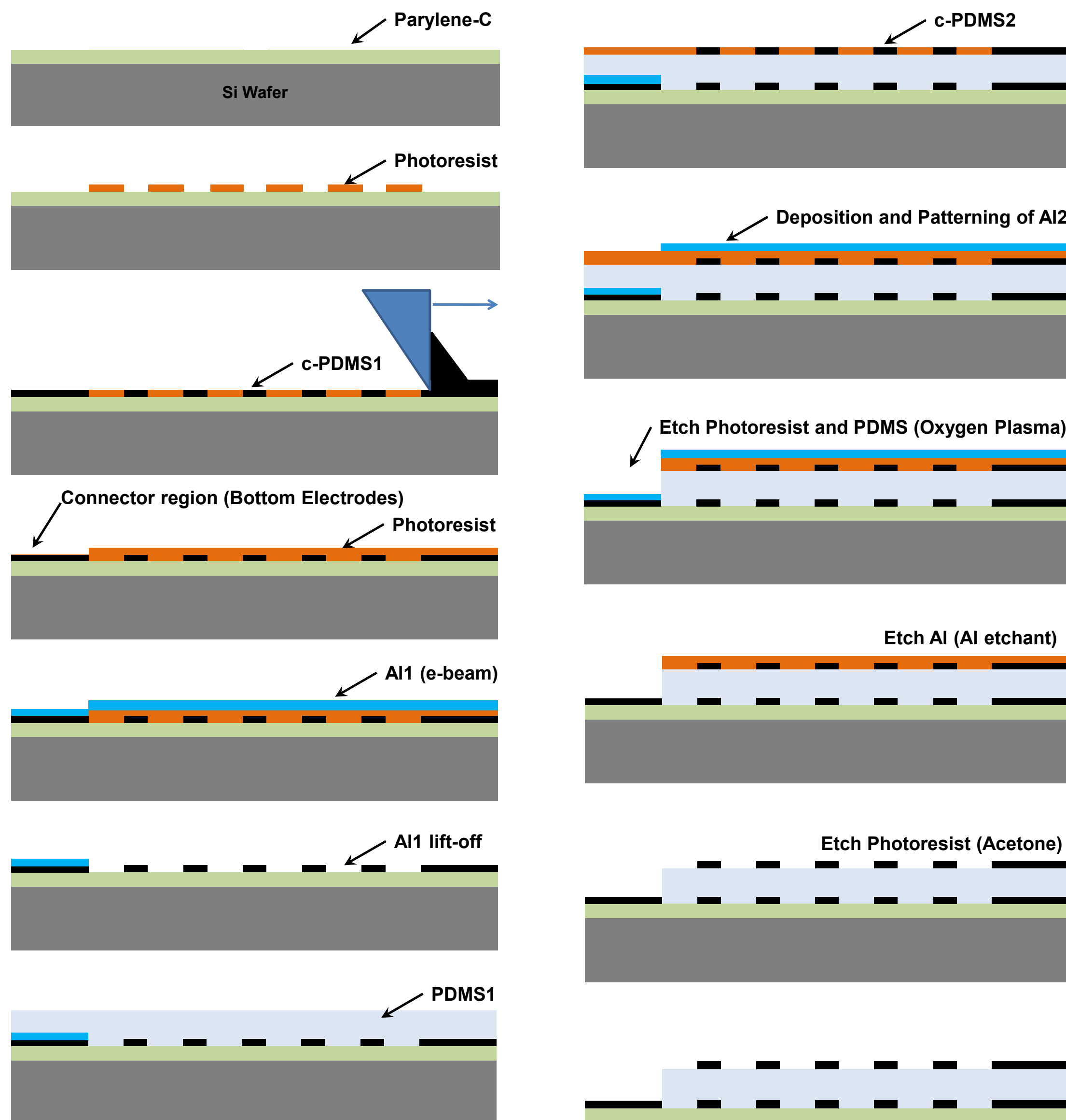

Figure 2.8. Simplified process flow of flexible FTI using conductive-PDMS. Top and bottom electrodes are represented by c-PDMS1 and c-PDMS2, respectively. PDMS1 forms the elastic dielectric material.

the bottom electrodes of the capacitor (c-PDMS1). After the bottom electrodes are completely cured at 65°C overnight, another layer of 2 μm photoresist is spin-coated and patterned to expose the connector region of the bottom electrodes. A 100 nm aluminum layer (Al1) is deposited over the entire FTI using e-beam evaporation. A lift-off process is performed such that Al1 remains on the connector region of the bottom electrodes. A layer of 20 μm PDMS (Sylgard-184, 10:1 ratio elastomer to curing agent) is spin-coated at 3000 prm for 30 s and cured at 65 ^{o}C for five hours which forms the elastic dielectric material (PDMS1). A 2 μm thick layer of positive photoresist is spin-coated and patterned on PDMS1 after alignment with c-PDMS1. The top electrode (c-PDMS2) is patterned by screen-printing MWCNT-loaded PDMS. Photoresist is spin-coated again to form another layer of 2 μm. 100nm thick aluminum (Al2) is then deposited on the entire FTI and patterned such that there is no Al over the connector region of the bottom electrodes. Al2 acts as a masking agent while oxygen plasma is performed (Oxford Plasmalab 80) to remove the photoresist from the connector region (bottom electrodes). SF_6 and O_2 at 30 sccm and 50 sccm, respectively, are used to etch the PDMS layer in the Oxford Plasmalab 80. Al1 acts as a masking agent/etch stop to protect the bottom electrodes at the connector region. Both Al1 and Al2 are removed by Al etchant. This is followed by removal of photoresist using acetone. Parylene is separated from the wafer to form the FTI. Figure 2.9 shows a comparison of etched and masked PDMS. Figure 2.9.(b) shows a scanning electron microscopy (SEM) image of the etched and masked PDMS. Fabricated bottom electrodes with an elastic dielectric PDMS layer are shown in Figure 2.10.

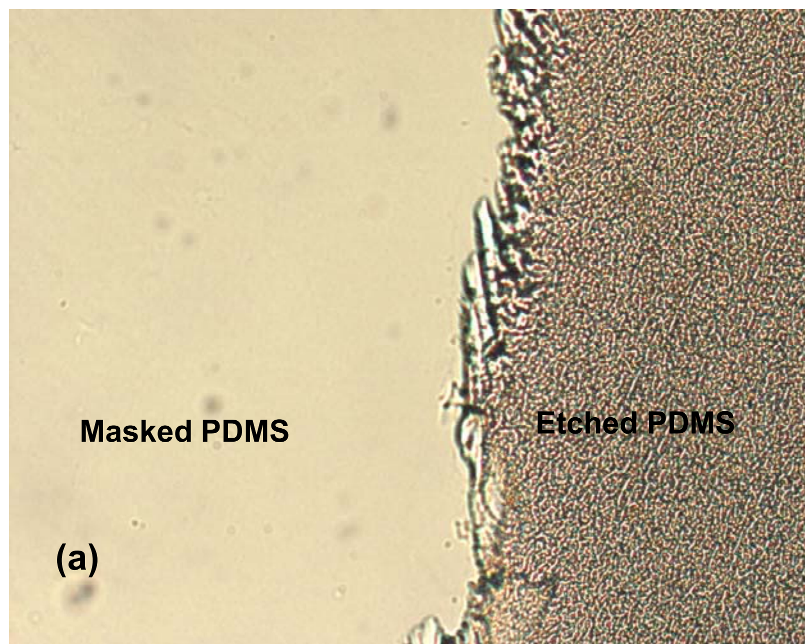

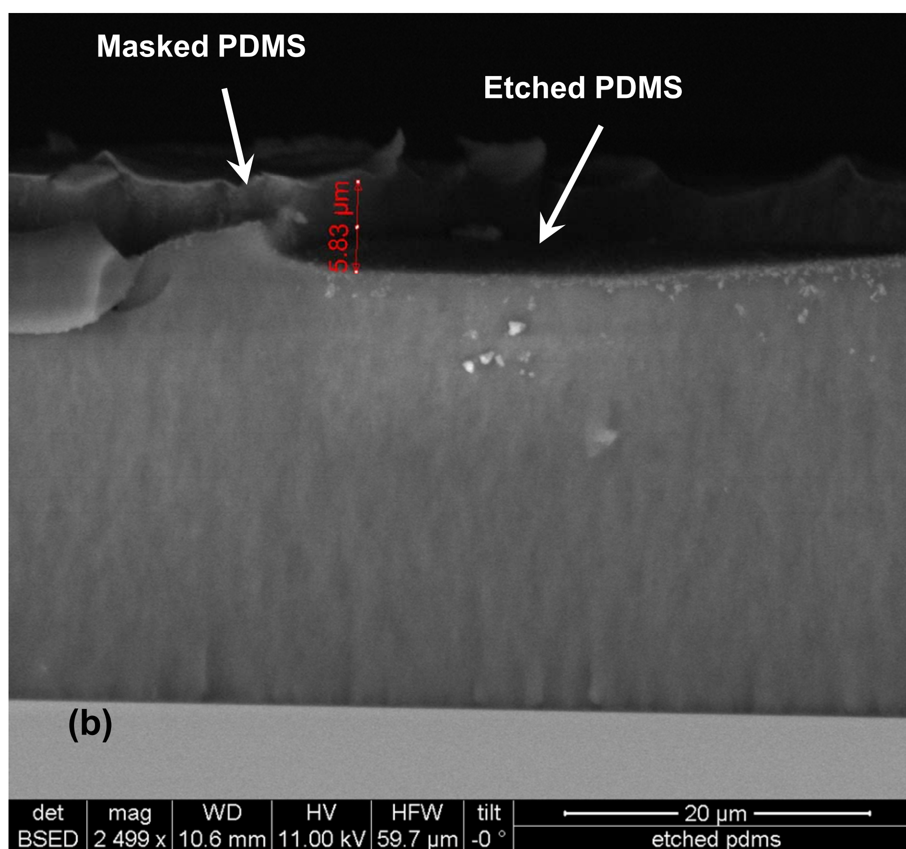

Figure 2.9. PDMS etch profile. (a) Optical image comparing etched PDMS to masked PDMS. (b) SEM image clearly identifying etched and masked PDMS.

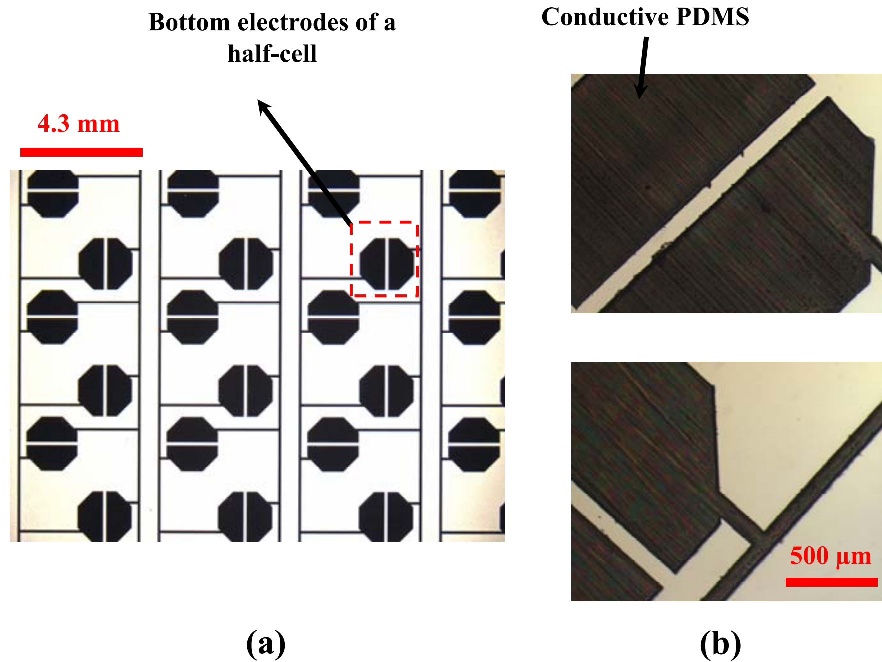

Figure 2.10. Images of the fabricated bottom layer. (a) Fabricated bottom electrodes with elastic dielectric PDMS layer. (b) Detailed views of bottom electrodes in a half-cell.

The sheet resistance of the 5% weight/weight MWCNT-loaded PDMS is about 3kΩ/□ [13]. Electrical resistance of a MWCNT-loaded PDMS 14cm long and 100 µm wide is measured by a Keithley 4200 SCS test station. The resistance is found to be as high as 45 MΩ. The thermal noise for the readout circuit depends on this resistance and is given by the equation:

$$\frac{V_n^2}{\Delta f} = k \cdot T \cdot R \tag{2.4}$$

where $V_n^2/\Delta f$ is the spectral density of the thermal noise for a resistor, k is the Boltzmann's constant, T is the temperature and R is the resistance measured in Ohms (Ω).

The high resistance of the electrodes thus results in a total output noise voltage of 0.49 mV. This is one of the contributing factors to the total noise on the readout circuit. Considering thermal noise due to high resistance alone, the readout circuit can only offer 11 bit resolution, whereas the required readout circuit design should offer 13 bits resolution. For this reason, low resistance electrodes are required. Furthermore, during the final Al1 and Al2 etching process (using aluminum etchant) in the fabrication flow, Al2 etching had difficulty since etched PDMS redeposited over Al2. For these reasons, a different fabrication method is adopted.

2.3.2 Thin-film metallization on parylene substrate based on simple design

Thin films of ductile metals such as gold (Au) or aluminum (Al) have been used in flexible electronics manufacturing techniques for almost half a decade now [5]. Au is chosen over Al due to its ease of evaporation in the e-beam evaporator. A substantial rise in substrate temperature can occur during Al metallization since the aluminum deposition rate is slower. The temperature rise causes an unwarranted PDMS thermal-expansion. Fabrication process flow of FTI devices using thin film metallization on parylene and PDMS is shown in Figure 2.11. A 5 µm thick parylene-C layer is first coated on a 5” Si-wafer. Photoresist (PR1813) is spin-coated and patterned using photolithography techniques. A seed layer of 20 nm chromium (Cr) followed by a 200 nm ductile metal (Au) layer is deposited using an e-beam evaporator and patterned by the lift-off process. The remaining metal on the Kapton film after the lift-off process forms the bottom electrodes (Metal1). PDMS which forms the elastic dielectric material is spin-coated and

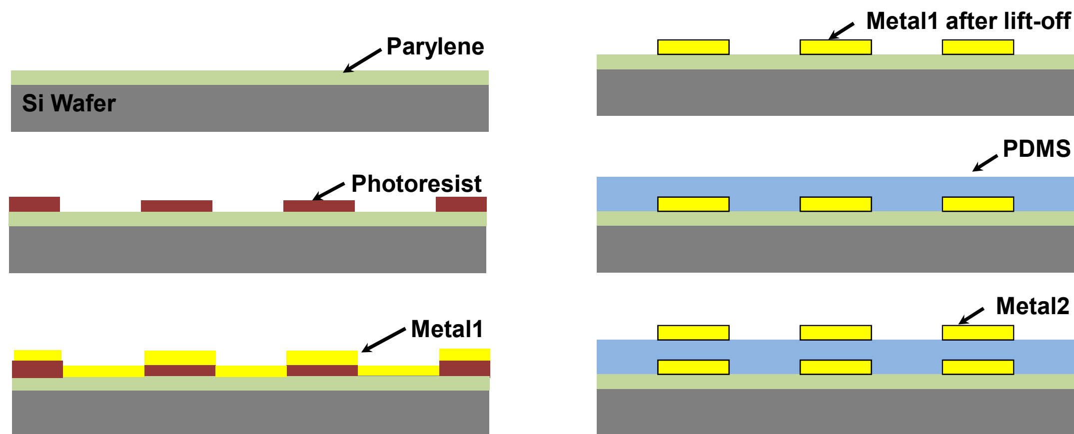

Figure 2.11. Simplified process flow of flexible FTI with thin film metallization on parylene substrate. Top and bottom electrodes are represented by Metal1 and Metal2, respectively. PDMS forms the elastic dielectric material.

cured (20 µm) on the film. Another layer of photoresist (PR1813) is spin-coated and patterned (after alignment with bottom electrodes) using photolithography techniques. Top electrodes are formed by deposition and lift-off of a 20/200 nm Cr/Au layer (Metal2) on top of the PDMS. A Cr layer (100nm) is deposited on the entire FTI and patterned such that PDMS over the connector region of the bottom electrodes is exposed. The remaining Cr layer acts as a mask to etch the exposed PDMS using Tetra-n-butylammonium fluoride (1M in Tetrahydrofuran (THF), Alfa-Aesar, USA). Figure 2.12 (a) shows a detailed view of the fabricated sensing cells. Figure 2.12 (b) shows the entire array on the Si-wafer.

However, the devices were damaged during the final fabrication step; parylene layer separation from the Si-substrate. One possible reason for the damage could be parylene having pin-holes during deposition on Si wafer in some spots. These pin-holes during the fabrication process expand to form blisters (which are not seen prior to fabrication of FTI). Figure 2.13 identifies blisters formed on the fabricated FTIs. Parylene eventually

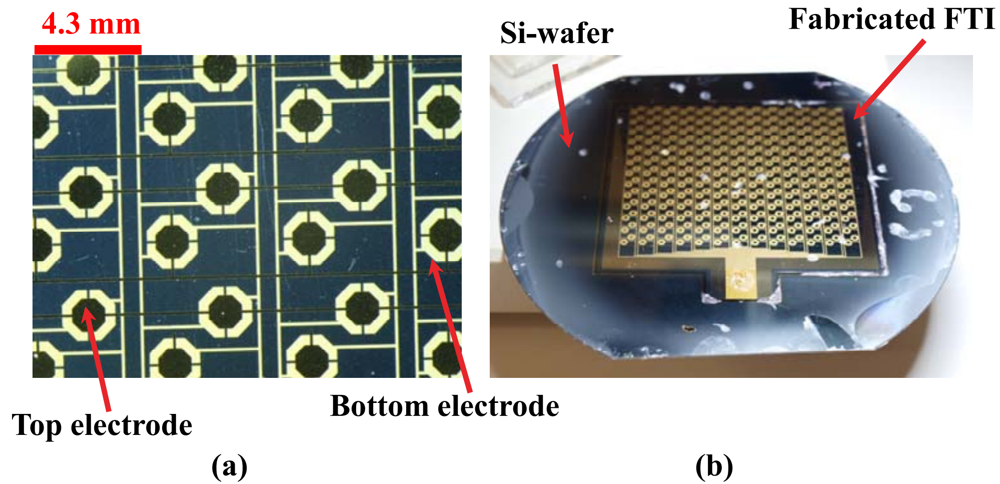

Figure 2.12. Fabricated FTI. (a) Detailed view of the fabricated FTI. (b) Entire fabricated FTI on a Si-wafer.

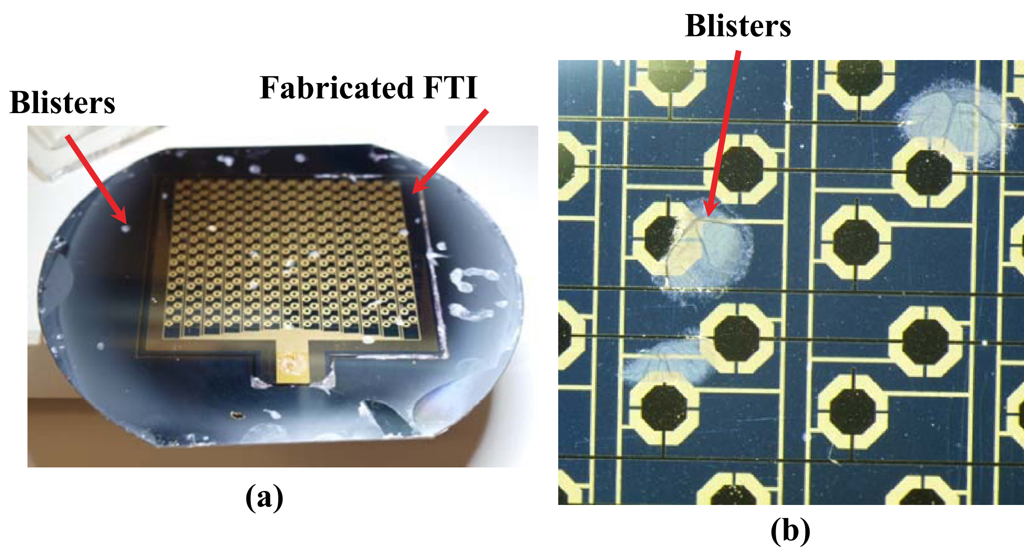

Figure 2.13. Blisters on the fabricated devices. (a) Entire fabricated FTI on the Si-wafer. (b) Image identifying blister formed in the parylene layer.

needs to be replaced by another flexible substrate material that can withstand the separation step. Choosing a material that can be readily available in the form of thin films is one viable solution.

2.3.3 Thin-film metallization on polyimide substrate based on alternative cell arrangement

Implementing the design criteria shown in Figure 2.6, FTI are fabricated on a polyimide substrate using thin-film metallization. Polyimide substrates are widely used as base materials for flexible cables in flexible printed circuit board (FPCB) technology. Kapton HN-500 (Dupont, USA) is a 125 μm thick off-the-shelf polyimide substrate that is compatible with MEMS fabrication techniques. This material has high tensile strength of 231MPa (that can withstand normal wear and tear) and can be taped to a 5” mask for structural support during fabrication.

Figure 2.14 shows a simplified process flow for the fabrication of FTIs. A 125 μm thick Kapton film (5” x 5”) is cleaned in DI water and thoroughly dried. A 20/200 nm Cr/Au layer (Metal1) is deposited by an e-beam evaporator and patterned by the lift-off process (as discussed in section 2.2.2). A 20 μm PDMS layer is next spin-coated after application of adhesion promoter (VM-652). The adhesion promoter improves the PDMS layer adhesion to the Kapton film. PDMS is cured overnight in an oven at 65°C. Next, parylene-C (1 μm), that acts as a buffer layer, is deposited over the PDMS after exposing the PDMS to A-174 (silane coating) adhesion promoter for parylene adhesion. Top electrodes (20/200 nm of Cr/Au) are aligned to Metal1 and patterned over parylene using the lift-off process (Metal2). A portion of the parylene layer is patterned and etched by

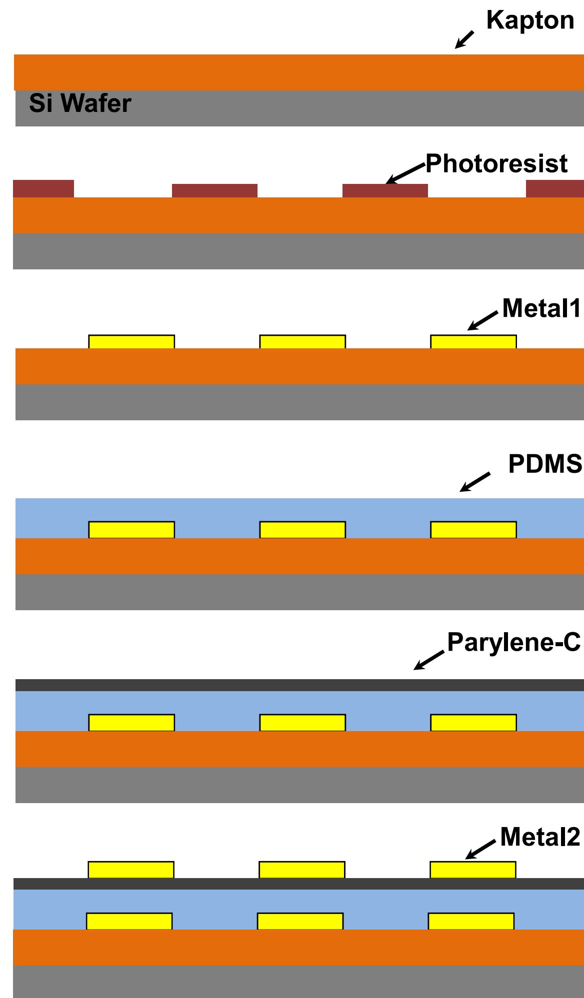

Figure 2.14. Process flow of flexible FTI with thin film metallization on parylene substrate (Metal1 and Metal2 being the top and bottom electrodes of the capacitor).

oxygen plasma to expose the underlying PDMS over the connector region of the bottom electrodes. The remaining parylene layer acts as a mask to etch the exposed PDMS using Tetra-n-butylammonium fluoride (1M in Tetrahydrofuran (THF), Alfa-Aesar, USA).

The 1 μm parylene buffer layer is deposited on top of the PDMS to shield the top surface of PDMS from thermal expansion. Figure 2.15 shows fabricated devices on a flexible Kapton substrate. Figure 2.15 (b) identifies wrinkles and crack propagation

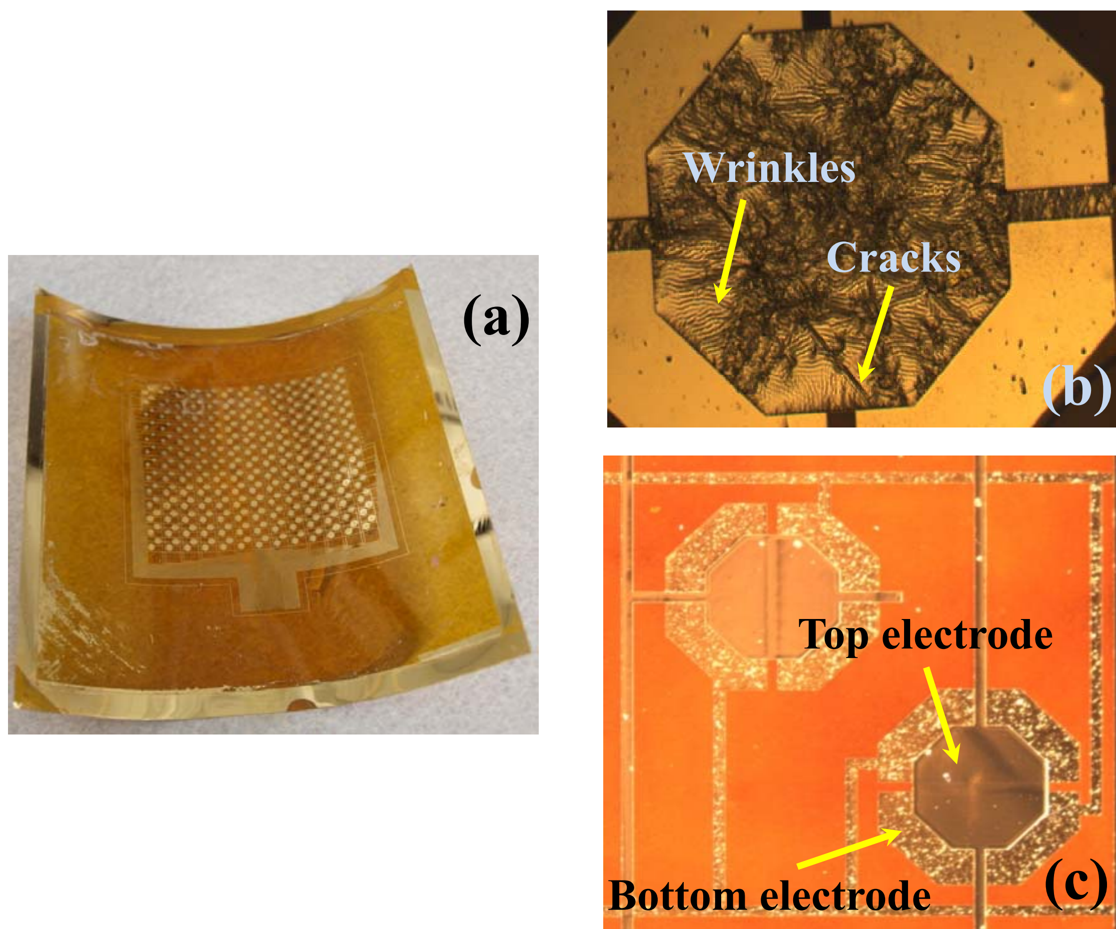

Figure 2.15. Fabricated devices. (a) Entire FTI fabricated on a Kapton film. (b) Detailed view of half-cell without buffer parylene layer. (c) Detailed view of half-cell after the introduction of buffer parylene layer.

developed in the top electrode metal (due to expansion of PDMS during metal deposition). Figure 2.15 (c) shows no such wrinkles or metal cracks due to the presence of the parylene buffer layer.

2.4 Experimental setup

Custom-made normal stress and shear stress application/measurement systems consist of a two-axis translation stage built from two microtranslation stages (Edmund Optics, USA), namely the Vertically-mounted stage (VMS) and Horizontally-mounted stage (HMS), as shown in the schematic of Figure 2.16. The stages can be controlled (VMS, HMS) by the movement of individual screw-gauges. In the normal stress application/measurement system, an 'L' shaped metal (Al) bar is connected to the VMS and the load cell ZPS-LM-11(Imada, USA) is placed on the bottom surface of the 'L' bar, as shown in Figure 2.16 (a). A normal load could be applied on the FTI using a load cell by lowering the VMS. However, in the shear application/measurement system, the load cell is directly mounted on to the VMS while a modified 'L' bar (with a rubber end cap) is attached to the load cell (iLoad-U TUF-002, Loadstar Sensors, USA), as shown in Figure 2.16 (b). First, a normal stress is applied on the FTI by lowering the VMS using the screw-gauge and then the output of the load cell is reset to zero. A shear force is then applied by rotating the screw gauge on the horizontally mounted stage (HMS).

2.5 Results and discussion

After the FTI is fabricated successfully, several unit cells at seven different locations are sliced using a sharp edged knife and the nominal capacitance is measured. The

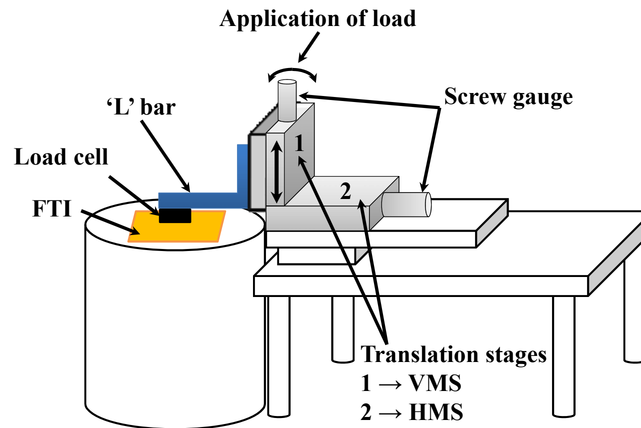

(a)

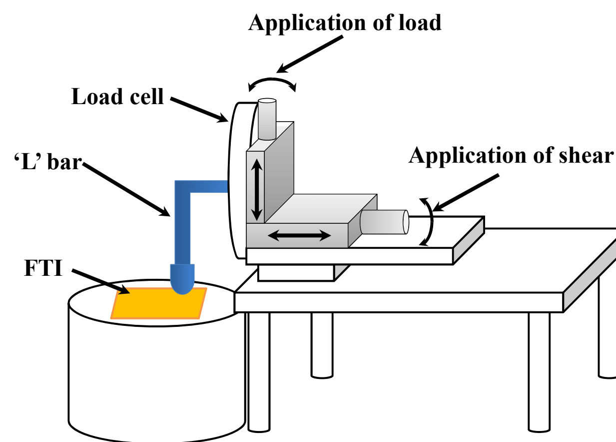

(b)

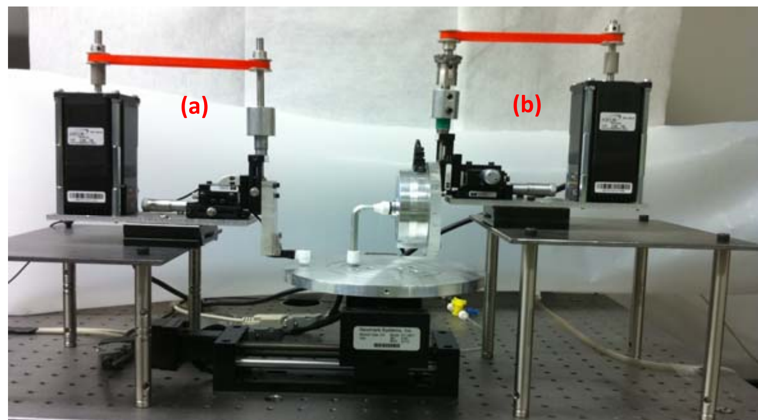

(c)

Figure 2.16. Custom-made normal stress and shear stress application/measurement systems. (a) Schematic representation of a normal stress application/measurement system, and (b) of shear application/measurement system. (c) Images of the systems.

capacitance of the individual capacitors in a cell are probed with a probe station using a precision LCR meter (Agilent 4284A). The nominal capacitance ranged from 804-927fF. Table 2.1 represents the nominal capacitance before and after isolating from the FTI (C1-C13 indicate the 13 columns and R1-R13 indicate the 13 rows of the FTI). The nominal capacitance before isolation is different due to the parasitic capacitance that adds to the nominal capacitance. The cell locations mentioned in the table are shown in Figure 2.17.

Under an applied stress, the capacitance of the individual capacitors in a cell are probed using the precision LCR meter. The LCR meter showed a higher capacitance reading due to the presence of overall parasitic capacitance of the array. Figure 2.18 shows the capacitive measurements of a single capacitor during normal/shear loading of the FTI. The normal and shear stress sensitivities of a capacitor are 0.58 MPa^{-1} and 0.052 MPa^{-1}, respectively.

Table 2.1. Nominal capacitances of seven cells before and after isolating from the FTI.

Cell Location	C_{1-2} connected to array (before cut)	C_{1-2} isolated (after cut)
C11, R1	12.0 pF	916 fF
C11, R3	12.0 pF	927 fF
C12, R3	3.5 pF	804 fF
C7, R2	18.5 pF	847 fF
C7, R3	17.9 pF	858 fF
C8, R3	15.5 pF	873 fF
C8, R4	17.2 pF	875 fF

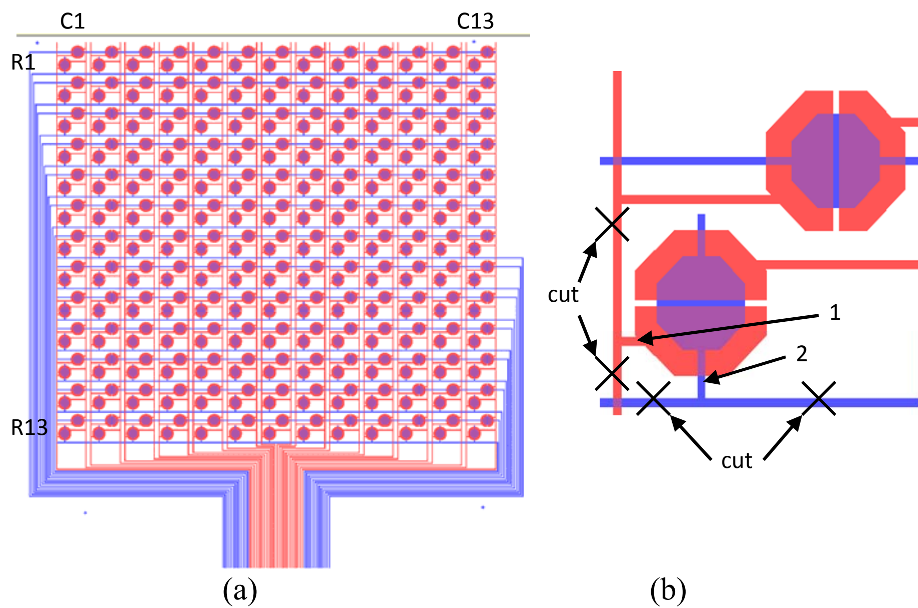

Figure 2.17. FTI layout identifying isolated cells. (a) Represents the cell locations mentioned in Table 2.1 and (b) the locations where the cuts are made.

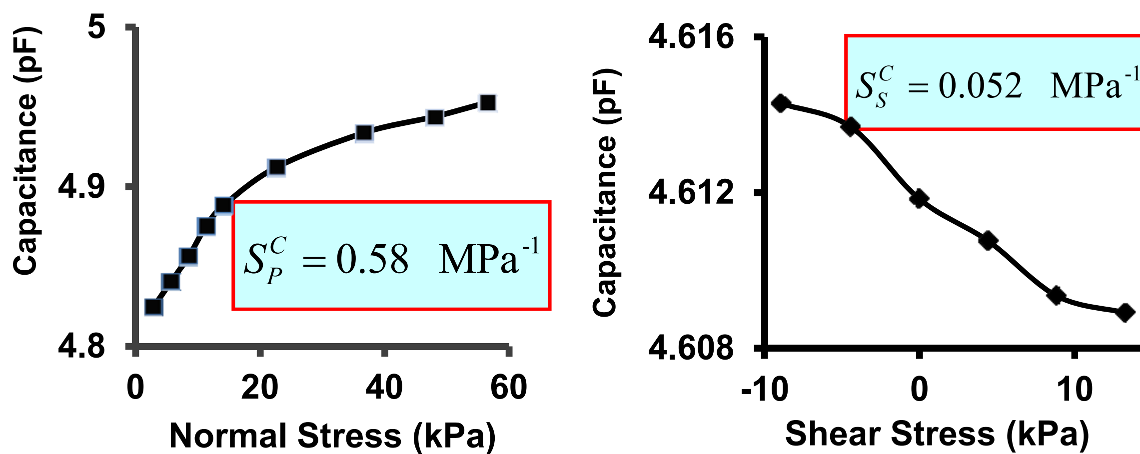

Figure 2.18. Measured capacitance for different normal stress and shear stress.

2.6 FTI to readout circuitry packaging

After initial experiments with individual cells, the entire FTI needs to be characterized. In order to achieve this, the FTI design was incorporated such that the electrical connections to the top electrodes in each row and the bottom electrodes in a column are realized to form a flex cable connector, as shown in Figure 2.1. The flex cable thus formed can be connected to a low profile flip-lock flex cable connector (FH29B-120S-0.2 SHW(05), from Hirose Electric Co., LTD.) on the readout circuit, as shown in Figure 2.19. After connecting to the flex cable connector, the teeth of the connector deformed the gold electrodes on PDMS by indentation. The indentation was extreme, destroying the gold electrodes on PDMS near the cable end. Once the electrodes were destroyed, the entire FTI could not be characterized. To overcome this problem, the flex cable design is modified and its specifics are discussed in Chapter 3.

2.7 Summary

Various methods to fabricate the FTI have been developed and carefully studied to understand the shortcomings of each method. Improvements have been proposed and implemented for the fabrication of a functional FTI. Individual capacitors of the FTI are interrogated using a custom measurement system and LCR meter. The developed design showed promising results for simultaneous normal stress and shear stress loading of the FTI. However, the shear stress sensitivity is lower compared to the sensitivity of normal stress. Multifingered electrode arrays with enhanced shear sensitivity are discussed in the next chapter as a viable solution.

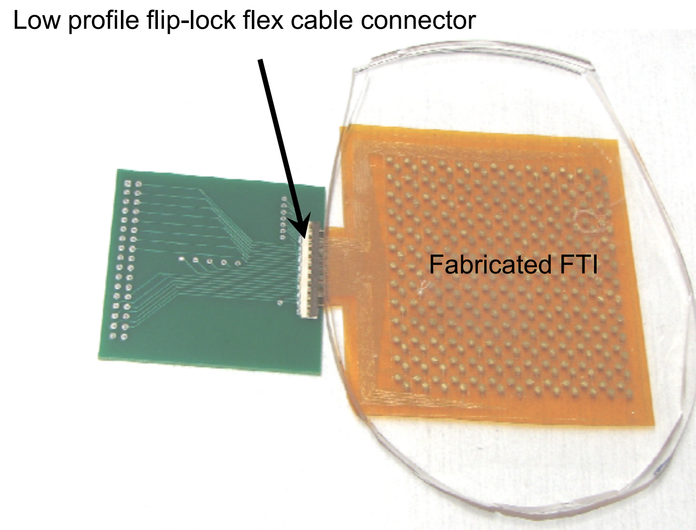

Figure 2.19. Fabricated FTI connected to a intermediate readout circuit through a low profile flip-lock flex cable connector.

2.8 References

[1] Someya T *et al*. 2004 A large-area, flexible pressure sensor matrix with organic field-effect transistors for artificial skin applications *PNAS 2004* **101** 9966-70

[2] Roch J *et al*. 2006 3 Axis capacitive tactile sensor and readout electronics," *IEEE ISIE 2006* pp. 2767-2772

[3] Suster M *et al*. 2010 Low-Interference Sensing Electronics For High-Resolution Error-Correcting Biomechanical Ground Reaction Sensor Cluster *Proc. IEEE Sensors, 2010*, pp. 1020-23

[4] Schneider F, Fellner T, Wilde J and Wallrabe U 2008 Mechanical properties of silicones for MEMS *J.Micromech. Microeng.* **18** 065008

[5] Kim T K, Kim J K and Jeong O C 2011 Nonlinear mechanical properties of PDMS elastomer *Microelectronic Eng.* **88** 1982-85

[6] Lui M, Sun J, Sun Y, Bock C and Chen Q 2009 Thickness-dependent mechanical properties of polydimethylsiloxane membranes *J.Micromech. Microeng.***19** 035028

[7] Wang Z 2011 Polydimethylsiloxane mechanical properties measured by macroscopic compression and nanoindentation techniques *Thesis University of South Florida*

[8] Carrillo F, Gupta S, Balooch M, Marshall S J, Marshall G W, Pruitt L and Puttlitz C 2005 Nanoindentation of polydimethylsiloxane elastomers: Effects of crosslinking, work of adhesion, and fluid environment of elastic modulus *J. Mater. Res.* **20** 2820-30

[9] Lotters J C, Olthuis W, Veltink P H and Bergveld P 1997 The mechanical properties of the rubber elastic polymer polydimethylsiloxane for sensor applications *J.Micromech. Microeng.* **7** 145-47

[10] Mannsfeld S C B, Tee B C K, Stoltenberg R M, Chen C V H H, Barman S, Muir B V O, Sokolov A N, Reese C and Bao Z 2010 Highly sensitive flexible pressure sensors with microstuctured rubber dielectric layers *Nature Mater.* **9** 859–64

[11] Pritchard E *et al*. 2008 Flexible capacitive sensors for high resolution pressure measurement *Proc. IEEE Sensors 2008* pp. 1484-1487

[12] Lotters J C, Olthuis W, Veltink P H and Bergveld P 1996 Polydimethylsiloxane as an elastic material applied in a capacitive accelerometer *J.Micromech. Microeng.* **6** 52-54

[13] Engel J *et al*. 2006 Multi-layer embedment of conductive and non-conductive PDMS for all-elastomer MEMS *Solid State Sensors, Actuators, and Microsystems Workshop*, Hilton Head, SC, pp. 316-319

CHAPTER 3

HIGHLY SENSITIVE MULTIFINGERED CAPACITIVE FLEXIBLE TACTILE IMAGER

3.1 Introduction

The developed FTI showed promising sensing capabilities to detect both the normal and shear stress simultaneously. The FTI, however, showed lower sensitivity to shear compared to normal stress (by a factor of ~10). This chapter discusses the design modifications that improved the shear sensitivity while maintaining good normal stress sensitivity.

3.2 Sensor design and fabrication

Consider a rectangular shaped parallel plate capacitor that is similar to our previous half-cell design as in Figure 3.1(a). The nominal capacitance (C_E) of the parallel plate capacitor with the top and bottom electrodes of length l, width w and separated by a distance t is given by the equation:

$$C_E = \varepsilon \frac{w \cdot l}{t} \tag{3.1}$$

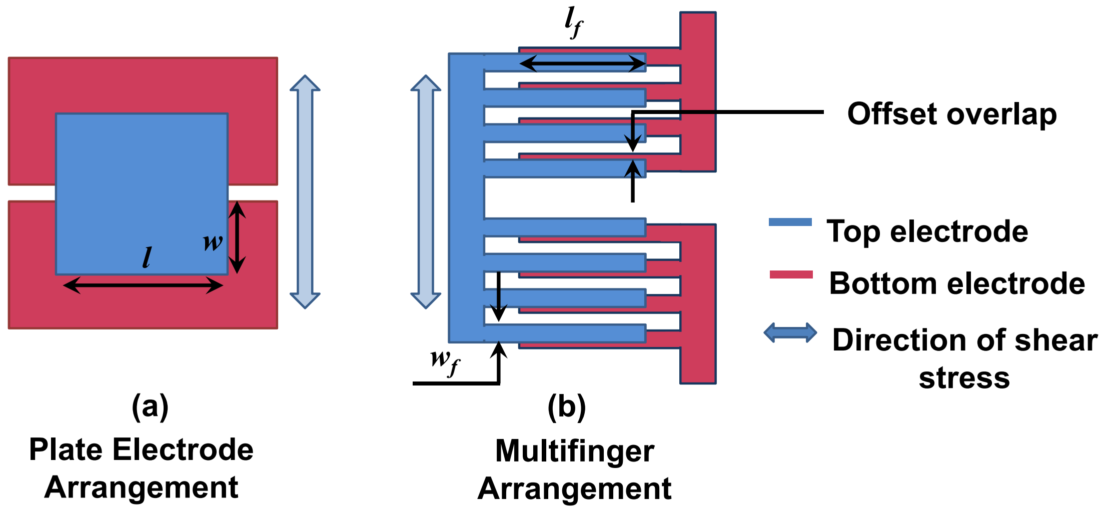

Figure 3.1. Comparison of plate electrode and multifingered electrode configuration.

where is ε the product of relative static permittivity (ε_r) and dielectric constant (ε_o). When this capacitor is subjected to a normal stress (S_N), the dielectric thickness changes by Δt and the capacitance change due to this stress (ΔC_{EN}) *is* given by the following equation:

$$\Delta C_{EN} = \varepsilon \frac{\Delta t \cdot w \cdot l}{t(t - \Delta t)} \tag{3.2}$$

When the dielectric material is subjected to normal stress, it undergoes strain ($\Delta t/t$) defined as the ratio of change in thickness (Δt) to the original thickness (t). Young's modulus of a material (E) is defined as the ratio of applied normal stress to strain experienced by the object and is given by the equation:

$$E(\frac{\Delta t}{t}) = S_N \Rightarrow \Delta t = \frac{S_N \cdot t}{E} \tag{3.3}$$

The normal stress sensitivity of this capacitor (S_N^C) is defined as the ratio of change in capacitance to the nominal capacitance per unit normal stress and is given by the equation:

$$S_N^C = \frac{\Delta C_{EN}}{C_E} \cdot \frac{1}{S_N} \tag{3.4}$$

From equations (3.1) and (3.2), the ratio of change in capacitance to the nominal capacitance is given by the equation:

$$\frac{\Delta C_{EN}}{C_E} \cong \frac{\Delta t}{t} \tag{3.5}$$

From equations (3.1), (3.3) and (3.5), equation (3.6) is derived:

$$\frac{\Delta C_{EN}}{C_E} = \frac{S_N}{E} \tag{3.6}$$

Now, substituting (3.6) in (3.4), normal stress sensitivity is given by the equation:

$$S_N^C = \frac{1}{E} \tag{3.7}$$

Similarly, when the capacitor is subjected to only shear stress (S_S), the overlap area ($w \cdot l$) of the capacitor increases or decreases depending on the direction of the shear. The change in overlap area ($\Delta x \cdot l$) causes a capacitance change (ΔC_{ES}) given by the equation:

$$\Delta C_{ES} = \varepsilon \frac{\Delta x \cdot l}{t} \tag{3.8}$$

When the same dielectric material is subjected to shear stress (S_S), it undergoes shear strain ($\Delta x/t$) defined as the ratio of plate displacement (Δx) in the direction of shear to the thickness of dielectric material. Shear modulus of a material (G) is defined as the ratio of applied shear stress to shear strain experienced by the object and is given by the equation:

$$G(\frac{\Delta x}{t}) = S_S \Rightarrow \Delta x = \frac{S_S \cdot t}{G} \tag{3.9}$$

The shear sensitivity (S_S^C), on the other hand, is defined as the ratio of change in capacitance to the nominal capacitance per unit shear stress applied and is given by the equation:

$$S_S^C = \frac{\Delta C_{ES}}{C_E} \cdot \frac{1}{S_S} \tag{3.10}$$

From equations (3.1) and (3.8),

$$\frac{\Delta C_{ES}}{C_E} = \frac{\Delta x}{t} \tag{3.11}$$

Substituting t from equation (3.1) in (3.9) and (3.9) in (3.11),

$$\frac{\Delta C_{ES}}{C_E} = \frac{S_S \cdot l}{G \cdot C_E} = \frac{S_S \cdot t}{G \cdot w} \tag{3.12}$$

Substituting (3.12) in (3.10), shear sensitivity is given by the equation:

$$S_S^C = \frac{t}{G \cdot w} \tag{3.13}$$

Equation 3.13 relates the shear sensitivity as a function of the thickness, shear modulus and width of the capacitor. In order to improve the shear sensitivity of a capacitor, the effective change in area due to the shear should be enhanced. One way to do this is to increase the length (l) of the top electrode (Figure 3.1). However, this also leads to an increase in the normal stress sensitivity and a consequent reduction in the sensor density for a unit area.

The need to improve the shear sensitivity while retaining the same nominal capacitance and normal stress sensitivity was conceptualized into a multifingered capacitive structure. Each capacitor consists of a series of finger electrodes as opposed to plate electrodes (such that the nominal capacitance remains the same), as shown in Figure 3.1. The fingers are staggered such that under a uniaxial shear stress, one of the

capacitances in a half-cell increases while the other decreases. However, under a uniform normal stress, both the capacitances in the half-cell would increase. The offset overlap between the top and bottom finger electrodes (seen in Figure 3.1(b)) of a capacitor offers the ability to measure shear stress. The design layout is materialized using a software L-edit (V.15).

The nominal capacitance (C_F) of the multifingered capacitor constructed from the fingered top and bottom electrodes of length l_f, width w_f and separated by a distance t is given by the equation:

$$C_F = \varepsilon \frac{N_f \cdot w_f \cdot l_f}{t} \tag{3.14}$$

where N_f is the number of fingers. When this capacitor is subjected to a normal stress (S_N), the dielectric material thickness changes by Δt and the capacitance change due to this stress (ΔC_{FN}) is given by the following equation:

$$\Delta C_{FN} = \varepsilon \frac{N_f \cdot w_f \cdot l_f \cdot \Delta t}{t(t-\Delta t)} \tag{3.15}$$

Young's modulus of a material (E) is given by the equation:

$$E(\frac{\Delta t}{t}) = S_N \Rightarrow \Delta t = \frac{S_N \cdot t}{E} \tag{3.16}$$

and the normal stress sensitivity S_N^{Cf} is given by the equation:

$$S_N^{Cf} = \frac{\Delta C_{FN}}{C_F} \cdot \frac{1}{S_N} \tag{3.17}$$

From equations (3.14) and (3.15), the ratio of change in capacitance to the nominal capacitance is given by the equation:

$$\frac{\Delta C_{FN}}{C_F} \cong \frac{\Delta t}{t} \tag{3.18}$$

Substituting t from equation (3.14) in (3.17) and (3.17) in (3.18),

$$\frac{\Delta C_{fFN}}{C_F} = \frac{S_N}{E} \tag{3.19}$$

Substituting (3.6) in (3.4), normal stress sensitivity is given by the equation:

$$S_N^{Cf} = \frac{1}{E} \tag{3.20}$$

Similarly, when the capacitor is subjected to only shear stress (S_S), the overlap area ($w_f \cdot l_f$) of the capacitor increases or decreases depending on the direction of the shear. The

change in overlap area per finger ($\Delta x \cdot l_f$) causes a capacitance change (ΔC_{FS}) given by the equation:

$$\Delta C_{FS} = \varepsilon \frac{N_f \cdot \Delta x \cdot l}{t} \tag{3.21}$$

When the dielectric material is subjected to shear stress (S_S), it undergoes shear strain ($\Delta x/t$) defined as the ratio of plate displacement (Δx) in the direction of shear to the thickness of dielectric material (t). The shear modulus of a material (G) is given by the equation:

$$G(\frac{\Delta x}{t}) = S_S \Rightarrow \Delta x = \frac{S_S \cdot t}{G} \tag{3.22}$$

The shear sensitivity of this capacitor (S_S^{Cf}) is given by the equation:

$$S_S^{Cf} = \frac{\Delta C_{FS}}{C_F} \cdot \frac{1}{S_S} \tag{3.23}$$

From equations (3.14) and (3.21),

$$\frac{\Delta C_{FS}}{C_F} = \frac{\Delta x}{t} \tag{3.24}$$

Substituting *t* from equation (3.14) in (3.22) and (3.22) in (3.24),

$$\frac{\Delta C_{fFS}}{C_{fF}} = \frac{N_f \cdot S_S \cdot l_f}{G \cdot C_{fF}} = \frac{N_f \cdot S_S \cdot t}{G \cdot w_f} \tag{3.25}$$

Substituting (3.12) in (3.10), shear sensitivity is given by the equation:

$$S_S^{Cf} = N_f \frac{t}{G \cdot w_f} \tag{3.26}$$

$$S_S^{Cf} = N_f \cdot S_S^C \tag{3.27}$$

From equation (3.7) and (3.20), it is evident that the normal stress sensitivity is unaffected (for the same nominal capacitance and dielectric thickness) and the shear sensitivity increased by N_f (from equation (3.27)). The circuit equivalent of a three-terminal two-capacitor (C_{AC}, C_{AD}) structure for a single shear axis that is similar to the previous design is shown in Figure 3.2. ($C_{AC}+C_{AD}$) attributes to normal stress, while the capacitor difference (C_{AC}-C_{AD}) is for the shear stress.

The multifingered half-cell can be rotated 90 degrees to obtain the shear vector, as shown in the sensing cell scheme of Figure 3.3. The capacitance value of the each of the capacitors in a half-cell can be measured by individually driving the 'blue' lines (A, B), while sensing on the vertical red lines (C, D), as shown in Figure 3.4. The FTI is designed to detect minimum contact line velocities as low as 250 µm/s. Each finger

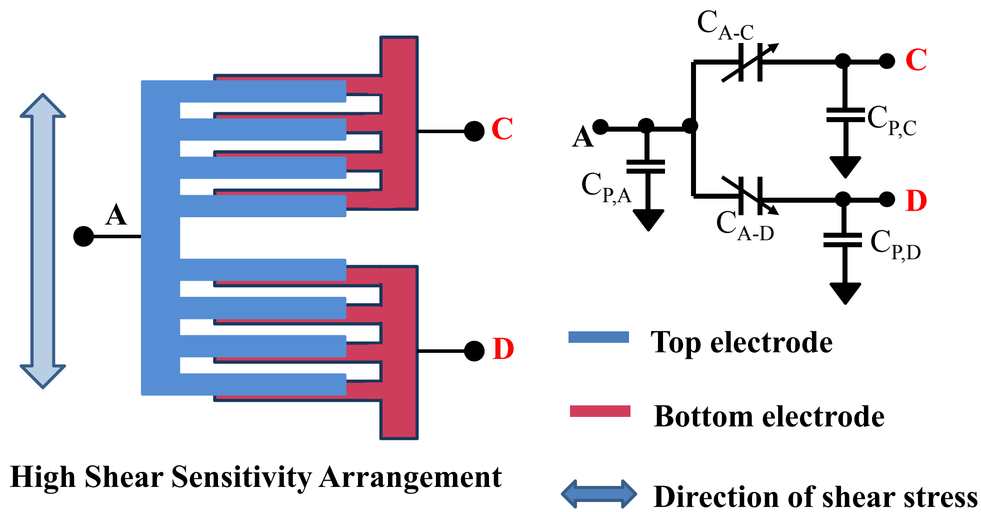

Figure 3.2. Uniaxial three-terminal two-capacitor representation for the multifingered FTI and its equivalent circuit. $C_{P,A}$, $C_{P,B}$ and $C_{P,C}$ are the parasitic capacitances associated with the terminals A, C and D, respectively, and $C_{A\text{-}C}$ and $C_{A\text{-}D}$ are the capacitances between terminals A, C and A, D, respectively.

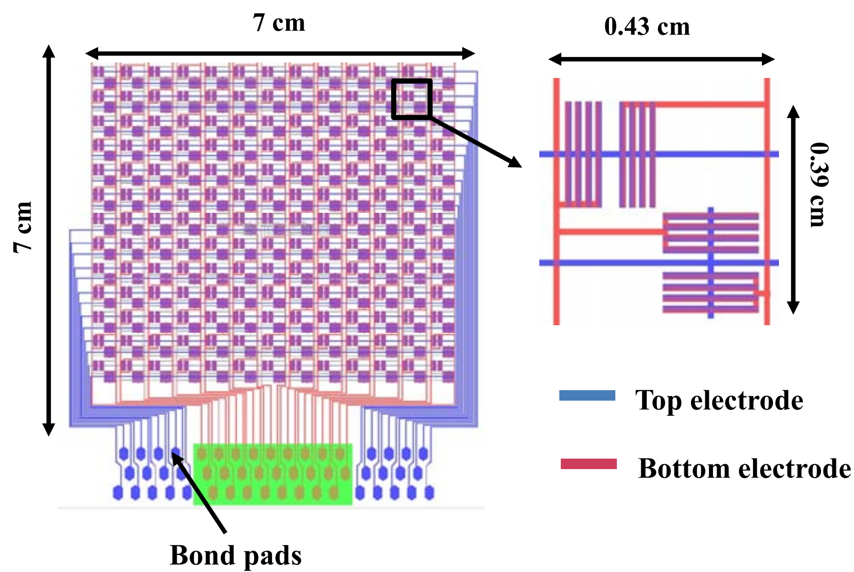

Figure 3.3. Schematic of L-edit layout of the entire FTI array and individual sensing cell.

measures 1900x100 μm^2. The theoretical capacitance of each half-cell capacitor is estimated as 897.2 fF (dielectric constant of 2.5 for PDMS, 15 μm of dielectric thickness and finger overlap area of 6.1x10^5 μm^2). The fabrication process flow for multifingered FTI is essentially identical to the fabrication of FTI based on thin-film metallization on a polyimide substrate (refer to section 2.2.3). Figure 3.5 shows a fabricated multifingered FTI and a detailed view of the finger cell, clearly depicting the offset between top and bottom electrodes.

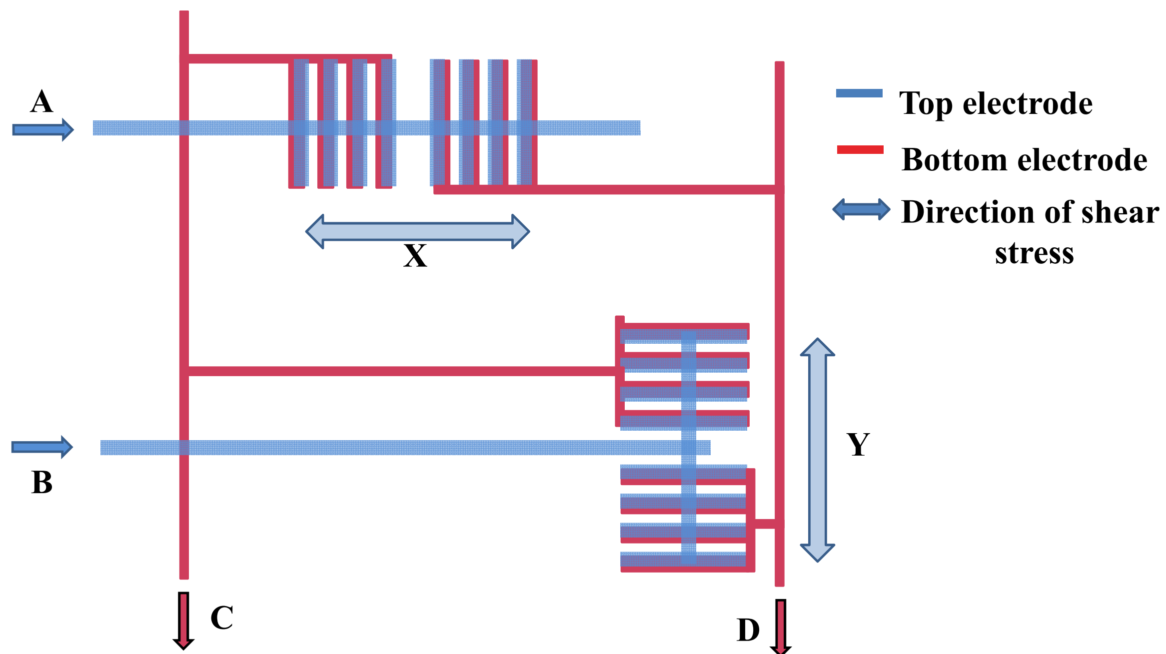

Figure 3.4. Addressing scheme of a single sensing cell in a multifingered FTI.

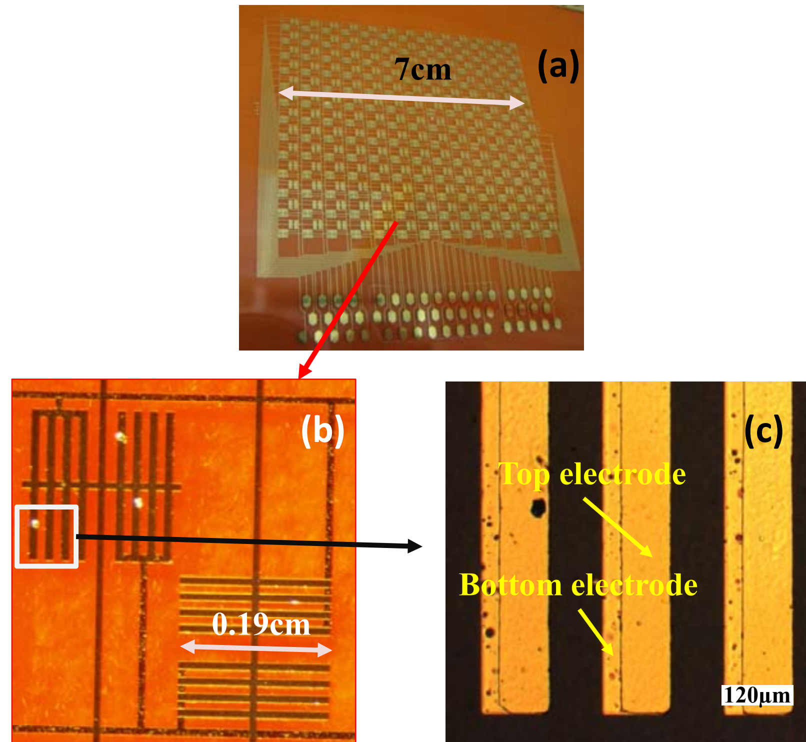

Figure 3.5. Images of the fabricated devices. (a) Image of entire fabricated multifingered FTI, (b) enlarged view of a single sensing cell, (c) detailed view of the fingers, identifying both top and bottom electrode.

3.3 Results and discussion

The capacitance of the finger structure cell and its variation on normal and shear stress are measured by a precision LCR meter (Agilent 4284A). The experimental setup discussed in section 2.3 is also used to test the multifingered FTI. The dependence of the finger cell capacitance on various normal and shear stresses are shown in Figure 3.6. A single capacitor of the multifingered FTI shows a sensitivity of 0.64 MPa^{-1} for normal stress and 0.16 MPa^{-1} for shear stress.

3.4 FTI to readout circuitry packaging

In order to characterize the entire FTI, the design incorporated bond pads at the end of electrical connections for each row and column, as shown in the design layout (see Figure 3.3). Initially, a wire bonding process was approached to connect the FTI to an intermediate readout circuit. Wire bonding works for rigid surfaces such as glass, silicon wafer or PCB. It does not work for polyimide surfaces due to its flexible nature. An alternative to this problem is to solder electrical wires carefully with a low temperature (< $300^{o}C$) solder rod to the bond pads. The other end of the wires are soldered to an intermediate readout circuit, as shown in Figure 3.7. This method of connecting the FTI to the readout circuit board presented two failure modes; firstly, the soldered wires were ultra-delicate and slight movement of the wires broke the solder (see Figure 3.7). The other failure mode was that the wires movement with respect to each other caused a change in capacitance even without application of external forces on the FTI.

To overcome these challenges, the electrical connection design was modified to incorporate soldering of a vertical flex cable connector (FH40-60S-0.5SV, from Hirose Electric Co., LTD.) on top of the FTI, as shown in Figure 3.8. Manual soldering of each connector pin was a difficult task and hence, automated soldering was chosen to solder the connector to the FTI. Since it was difficult to control the temperature in an automated soldering machine, the machine dissolved the gold bond pads, as shown in Figure 3.8 (b).

A conductive silver epoxy (EJ2189, from Epoxy Technology, USA) is formed by mixing EJ2189 Part A and EJ2189 Part B in a 10:1 ratio. This conductive silver epoxy is screen printed on the gold pads of the FTI. The screen-printing process forms silver epoxy bumps, as shown in Figure 3.9 (a). The connector pins of the vertical flex cable

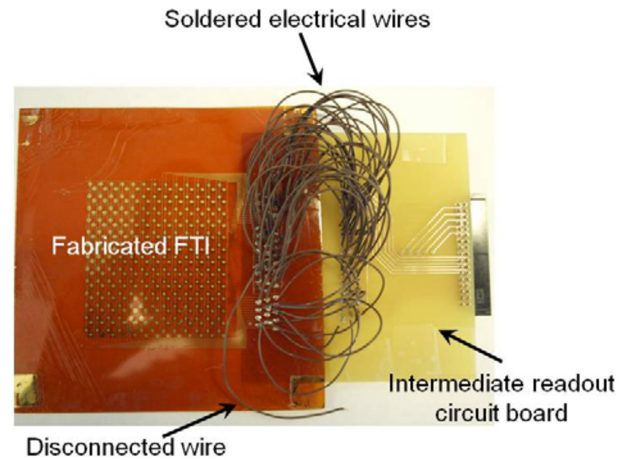

Figure 3.7. Fabricated FTI connected to intermediate readout circuit board via soldered electrical wires. The soldered wires are delicate to handle and the image identifies one such disconnected wire.

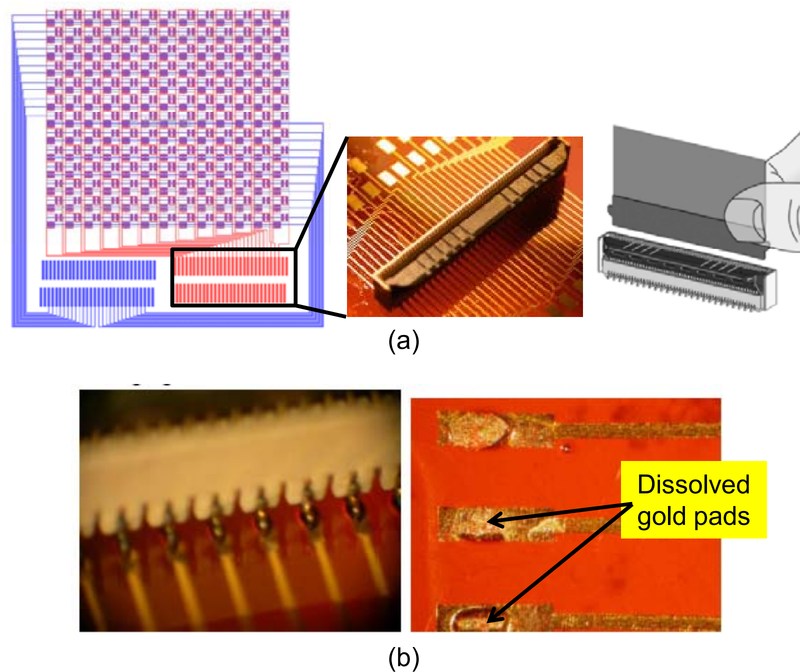

Figure 3.8. Integration of the connector to the FTI and issues during integration. (a) Modified layout to incorporate vertical flex cable connector. (b) Soldering the connector caused dissolving gold pad on the FTI due to excessive heat.

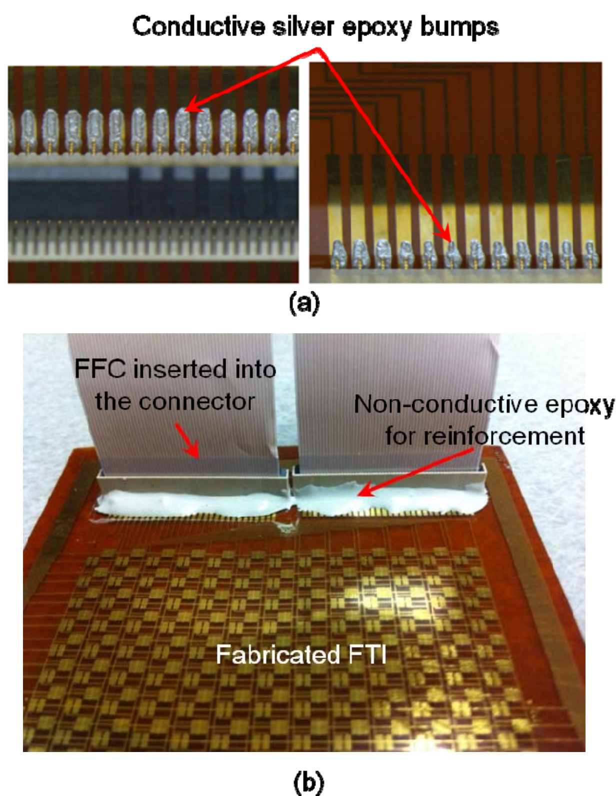

Figure 3.9. Successful integration of connectors to the fabricated FTI. (a) Connector pins placed on the conductive silver epoxy bumps and cured. (b) The connector is reinforced to the FTI using a nonconductive epoxy. The image also shows FFC inserted into the vertical connector for electrical connections.

connector are carefully placed on bumps and allowed to cure for one hour at 60°C. The vertical flex cable connector is reinforced onto the FTI using a nonconductive epoxy (Loctite Epoxi-Patch Adhesive 1C Hysol, from Henkel Corp., USA), as shown in Figure 3.9 (b). Flat Flex Cables (FFCs) that connect to the readout circuits are inserted into the vertical flex cable connectors to form electrical connections.

Despite the improved sensitivity and ability to characterize the entire FTI using a readout circuit, the electrical interconnects (on the PDMS) for the FTI failed after few deformation cycles (loading and unloading the cell). During deformation, metals deposited on top of compressible elastomeric material undergo large local expansions, as

shown in Figure 3.10 (a) (coefficient of elasticity of elastomeric material >> coefficient of elasticity of deposited metal). This leads to cracking of the top metal layer causing electrical failure, as shown in Figure 3.10 (b).

3.5 Summary

The successfully fabricated multifingered FTI evidently showed improvements in the shear sensitivity. Shear sensitivity increased by a factor of ~4 (also the number of fingers) as compared to the plate capacitor described in Chapter 2, while maintaining the normal stress sensitivity. Despite the improved sensitivity, the electrical interconnects failed due to metallization issues after few deformation cycles (loading and unloading the cell). A detailed explanation for the cause of metallization issues is discussed in the next chapter. The next two chapters will present viable alternative solutions to the metallization issues such as the use of a self-repairing metallization scheme and floating electrode scheme.

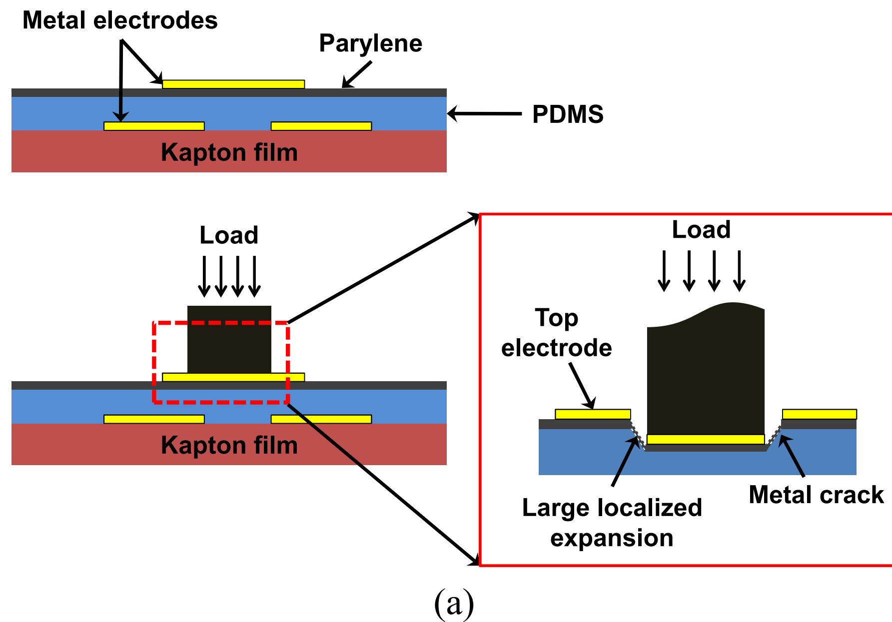

(a)

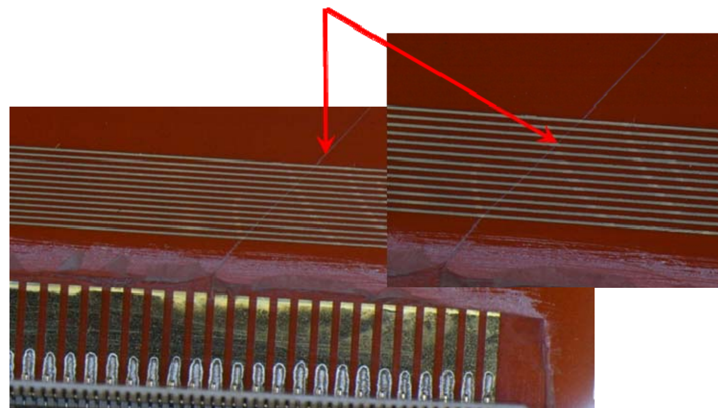

(b)

Figure 3.10. Metallization issues. (a) Schematics of a FTI cell during load application. A large localized expansion developing metal cracks. (b) Image of the microcracks that break the electrical connectivity of gold deposited on PDMS.

CHAPTER 4

A SELF-REPAIRING HIGH-RESOLUTION FLEXIBLE TACTILE IMAGER WITH LIQUID-METAL ELECTRODES

4.1 Introduction

In the previous chapter, we discussed the design and fabrication of an FTI with improved shear sensitivity while maintaining the normal stress sensitivity. The sensing cell in the developed FTI, however, failed during continuous extended deformation cycles (loading and unloading cycles) due to metallization issues. This chapter will discuss these issues and propose certain design modifications that can incorporate liquid-metal top electrodes which are nonsusceptible to metal cracking.

4.2 Metallization issues

Durable flexible mechanical sensors that can withstand millions of large deformation cycles are needed in many harsh “rubber-meets-ground” type applications. Some of the common applications include robotic grippers, wearable sensor systems, impact, tactile and other proximity sensors. These devices are generally difficult to produce because the periodic deformation during wear can break their vital components such as metal interconnects after just a few hundred or thousand cycles.

In particular, the fabrication of reliable interconnect schemes for flexible microsystems remains an open research problem [1]. During deformation cycles, metals deposited on top of compressible elastomeric material undergo large local expansions (coefficient of elasticity of elastomeric material >> coefficient of elasticity of deposited metal). This leads to cracking of the deposited metal during a deformation cycle. Lacour et al. in 2003 [2] developed a thin buckling-Au deposited over prestretched PDMS that could withstand large deformation cycles. This technique, however, could not be used in the case of FTIs, as they are built on a Kapton substrate that is not elastomeric (only the PDMS coated on the Kapton layer is elastomeric) which makes it impossible to prestretch the PDMS. The other possibility proposed by J. Engel and others [3-6] is the use of a conductive nanoparticle-laden elastomer to serve as interconnects. Although the methods discussed above were found to endure deformation cycles, these interconnects could not be used for high-speed electronics because of their high sheet resistances (~30 Ω/□).

Recently, the idea of using flexible interconnects using low-resistivity liquid metals has been used to fabricate flexible antennas [7]. Such metallization schemes are attractive to the ever-shrinking cellphone or other hand-held devices. By the virtue of liquid-metal, this scheme provides a continuous electrical connection during harsh deformation cycles. Liquid metals like Eutectic Gallium Indium alloy (EGaIn and Mercury (Hg) are found to exhibit self-healing properties [8-9].

In this chapter, a combination of thin Au and liquid-metal schemes are used to fabricate a FTI that can self-repair the Au broken connections. The liquid-metal used for the development of FTIs in this chapter is a eutectic mixture of (62%, 22%, 13% by weight) E-GaInSn (purchased from Alfa-Aesar, MA, USA). This alloy is liquid at

temperatures higher than 8 ^oC. The reliability of the liquid-metallization scheme has been tested prior to the FTI development. A PDMS channel of 140 mm×100 µm×42 µm which forms a wire loop is filled with liquid-metal (eutectic GaInSn), yielding a resistivity of 0.75×10^{-6} Ω-m and sheet resistance 18 mΩ/□. This structure is continuously subjected to periodic deformation of about 40% strain using a mechanical setup shown in Figure 4.1. The mechanical setup consists of a computer-driven relay connected to a lever that stresses the PDMS structure (the relay pulse frequency being 1 Hz). The wire resistance of the liquid-metal in the PDMS channel is measured during continuous stress application. Figure 4.2 shows the wire loop resistance liquid-metal channel for 750,000 bending cycles. It is clearly evident from the graph that wire loop resistance did not change despite continuous stress application. From this, it can be inferred that the metal cracking issue is not prominently seen in liquid-metal channel due to is self-repairing ability.

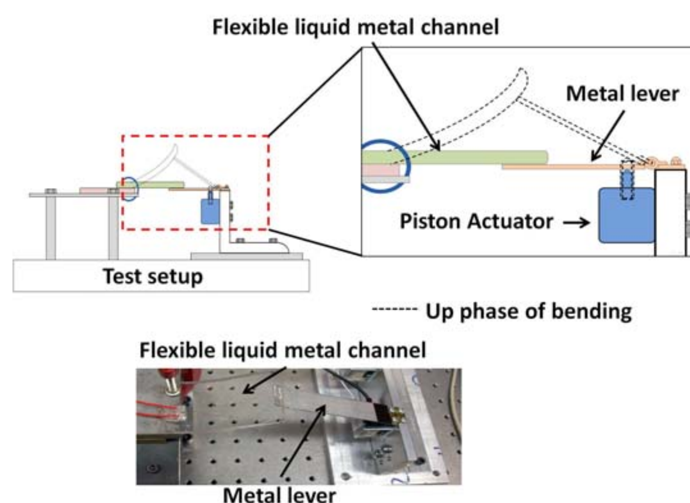

Figure 4.1. Setup for resistance characterization of liquid-metal in PDMS channels.

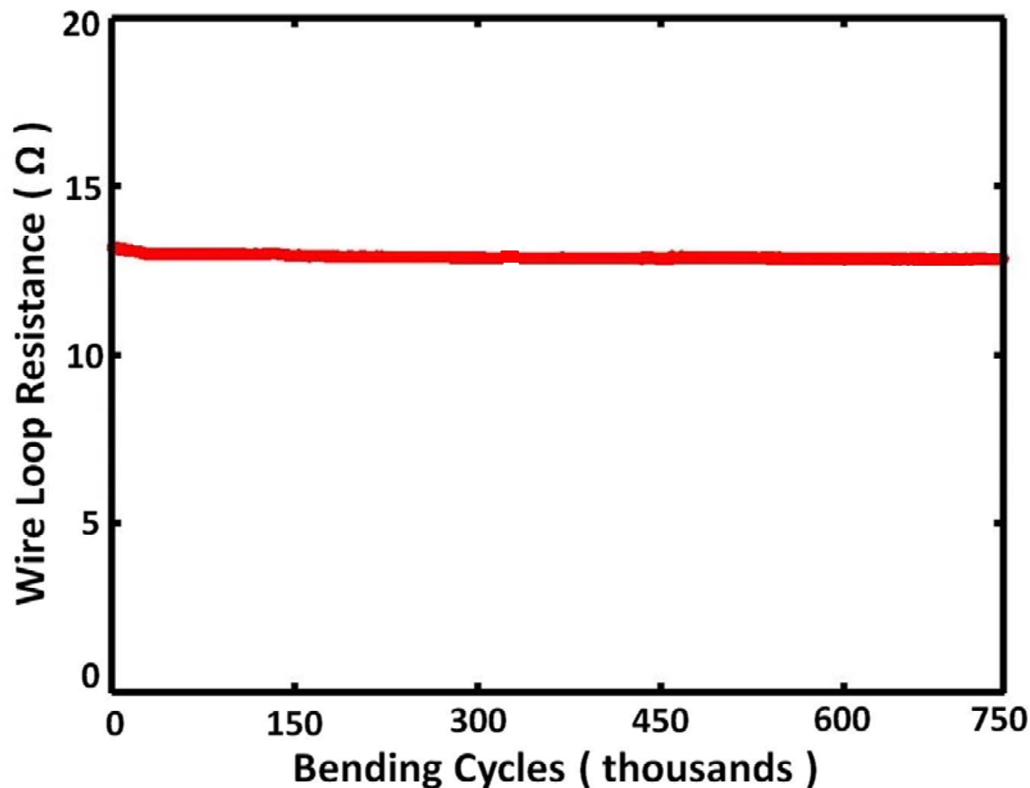

Figure 4.2. The wire loop resistance vs bending cycles. It is evident from the graph that the resistance even after 750,000 bending cycles remained unperturbed.

4.3 Sensor Design and Fabrication

The multifingered design discussed in Chapter 3 (see section 3.2) is slightly modified to incorporate the liquid-metallization scheme. Since the top electrodes in a row are connected in series, the top electrodes are formed by filling a serpentine channel with liquid-metal instead of the multifingers (however, the bottom electrodes are still multifingers). A schematic of a sensing cell is shown in Figure 4.3. Each sensing cell consists of a pair of half-cells that measure both normal and shear stress at the point of contact (for simplicity, only three fingers are shown in the schematic of Figure 4.3). When the cell is subjected to uniaxial force, the overlapping area of the channel with the

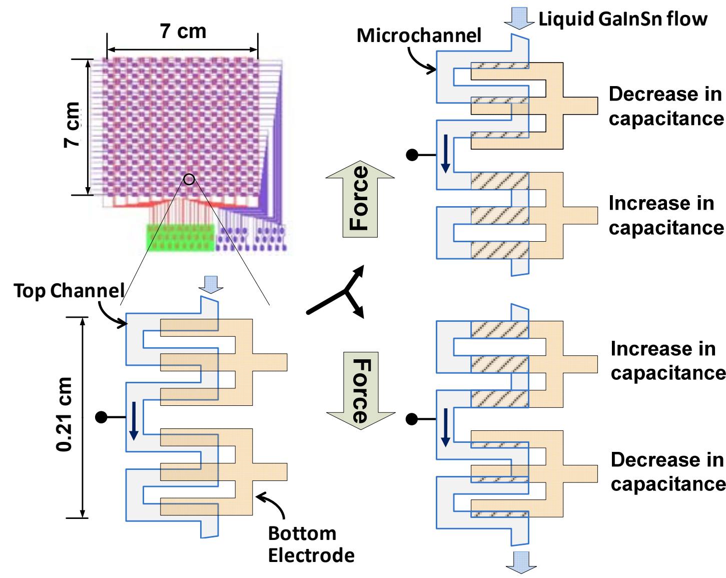

Figure 4.3. FTI with liquid-metal implementation via microfluidic overlay. The bottom electrode is formed by thin film metallization and bottom electrode is formed by a combination of thin film metallization and liquid-metal implementation.

bottom electrodes increase or decrease, changing the capacitance in each capacitor (depending on the direction of the force). In a sensing cell, the normal stress is determined from the sum of all the cell capacitances while shear stress is determined from the capacitance difference in a half-cell. The respective sensitivities to normal and shear stress are the same as multifingered structures' (see section 3.2) and are given by the equation:

$$S_N^{Cf} = \frac{1}{E};\ S_S^{Cf} = N_f \frac{t}{G \cdot w_f} \tag{4.1}$$

The FTI is constructed as shown in the process flow of Figure 4.4. The FTI bottom electrodes (Metal1) are patterned to form a Cr/Au layer (20/200 nm) on a 125 µm thick Kapton. A 20 µm thick PDMS (PDMS1), spin-coated over the bottom electrodes, acts as

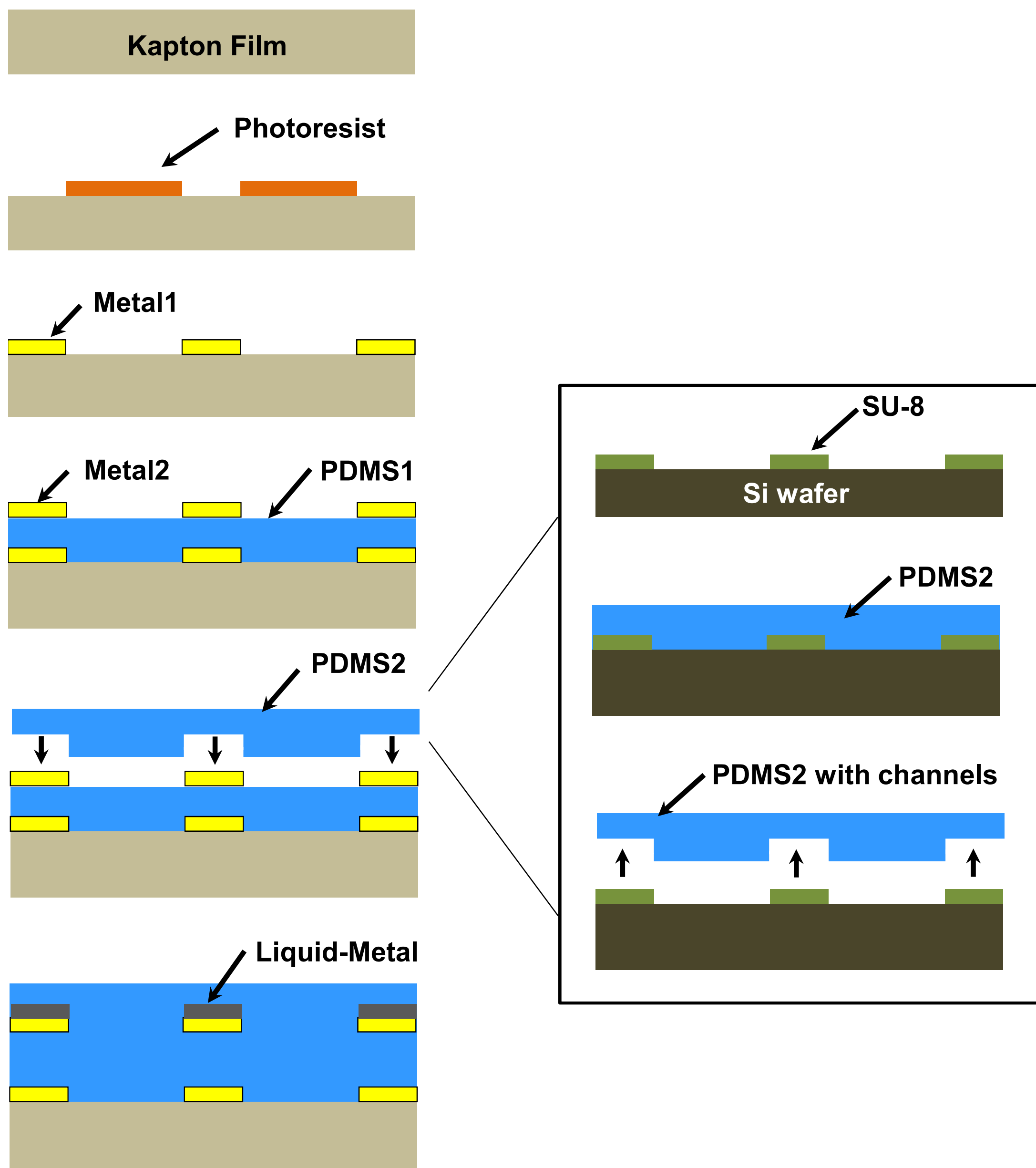

Figure 4.4. Simplified process flow for liquid-metal FTI. The insert (to the right) shows process flow for fabrication of PDMS with channels.

an elastic dielectric material. A Metal2 layer of Cr/Au layer (20/200 nm) is deposited and patterned (after alignment to Metal1). A Si-wafer-based soft-lithography process is used to realize microchannels (height: 40 μm) in a second layer of PDMS (PDMS2) [5]. Microholes are drilled through PDMS2 to access the underlying channel. PDMS 2 is bonded to PDMS1 such that the microchannels of PDMS2 are aligned to Metal2. The microchannels are next filled with the liquid-metal (E-GaInSn) through the microholes. The Metal2 layer and the channels filled with liquid-metal form the top electrodes of the FTI. Figure 4.5 shows the entire fabricated FTI, a single sensing cell and the detailed view of the top electrode and the bottom electrode offset.

4.4 Results and Discussion

Figure 4.6 shows initial experimental characteristics of capacitance versus normal and shear stress for a sensing cell. The capacitance of the top serpentine liquid-metal structure and its variation on normal and shear stress are measured by precision LCR meter. The experimental setup used to test FTI with thin-film metallization on polyimide substrate is also used for testing the FTI with liquid metallization scheme. A single capacitor of the FTI showed a sensitivity of 0.74 MPa^{-1} for normal stress and 0.22 MPa^{-1} for shear stress. However, the fabrication involved the alignment of PDMS2 (with microchannels) to the substrate. This step is difficult to achieve since there is no well-defined apparatus that can perform alignment step with good yield. Furthermore, electrical connection to the liquid-metal involved insertion of metal wires into the microholes and posed a failure mode (due to moving electrical connections).

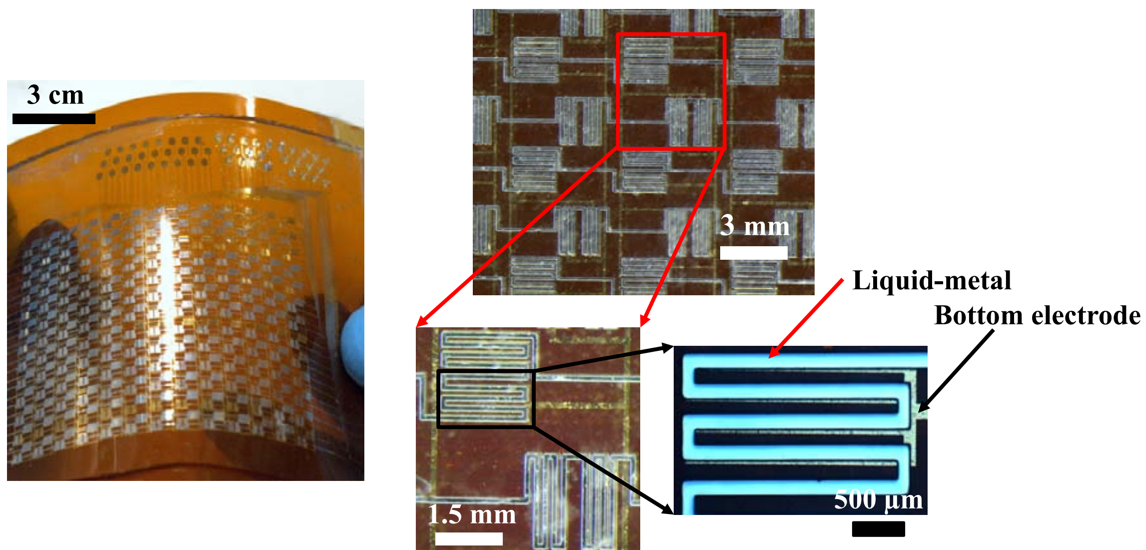

Figure 4.5. Chip photograph of the FTI, detailed view of sensing cells identifying liquid-metal layer and bottom electrode.

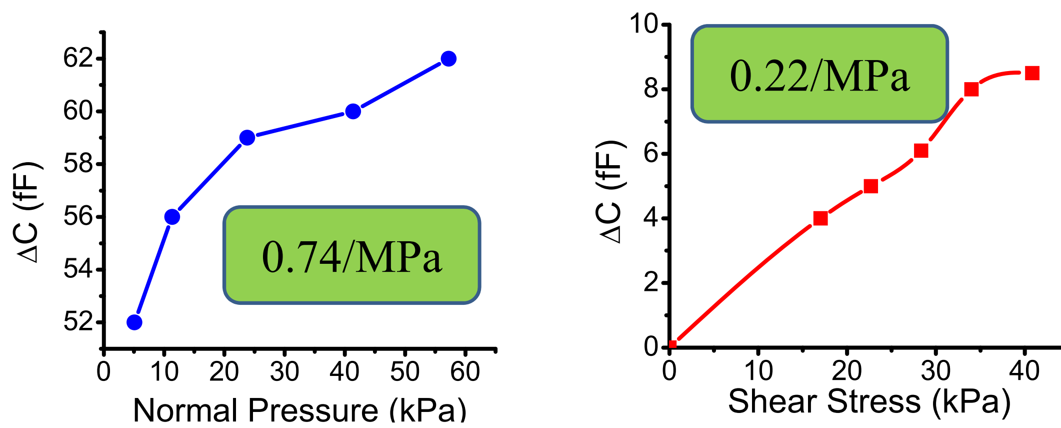

Figure 4.6. Measured capacitance for a range of normal and shear stress on a capacitor in the fabricated FTI.

4.5 Summary

A PDMS channel filled with liquid-metal is tested to check the metallization reliability, prior to the FTI development. Liquid-metal in the channels showed no influence on the resistivity and remained intact and continuous even after 750,000 cycles of large deformation strain (~40%). Based on these results, a FTI with self-repairing liquid-metallization scheme was successfully developed and fabricated. The measured normal and shear stress sensitivities of this scheme are 0.74 MPa^{-1} and 0.22 MPa^{-1}, respectively (comparable to sensitivities 0.64 MPa^{-1} and 0.16 MPa^{-1} measured from the previous design). Despite being highly reliable and sensitive, the complicated alignment procedure hampered its potential as an alternative to other FTI designs. The design presented a new set of alignment and electrical connection issues. Considering the above discussed issues, a new overhauled design is proposed in Chapter 5. The new design employing floating comb-electrodes also addresses the metal cracking due to localized expansion of the PDMS layer discussed in Chapter 3.

4.6 References

[1] Lacour S P, Jones J, wagner S, Li T and Suo Z 2005 Stretchable interconnects for elastic electronic surfaces *Proceedings of the IEEE* **93** 8

[2] Lacour S P, Huang Z, Suo Z, and Wagner S 2003 Stretchable gold conductors on elastomeric substrates *Appl. Phys. Lett.* **82** 2404–06

[3] Engel J M, Chen J, Chen N, Pandya S, and Liu C 2006 Multi-Walled Carbon Nanotube Filled Conductive Elastomers: Materials and Application to Micro Transducers *presented at IEEE International Conference on MEMS 2006*

[4] Niu X, Peng P, Liu L, Wen W and Sheng P 2007 Characterizing and Patterning of PDMS-Based Conducting Composites *Adv. Mater.* **19** 2682–86

[5] Huang D, Liao F, Molesa Redinger S D, and Subramanian V 2003 Plastic-Compatible Low Resistance Printable Gold Nanoparticle Conductors for Flexible Electronics *Journal of The Electrochemical Society* **150** G412-G417

[6] Cong H and Pan T 2008 Photopatternable Conductive PDMS Materials for Microfabrication *Adv. Funct. Mater.***18** 1912–21

[7] Cheng S, Rydberg A, Hjort K, and Wu Z, "Liquid metal stretchable unbalanced loop antenna", Adv. Funct. Mater. 2008, 18, 1912–1921.

[8] Siegel A C *et al*. 2007 Microsolidics: Fabrication of Three-Dimensional Metallic Microstructures in Poly(dimethylsiloxane) *Adv. Mater.* **19** 727–33

[9] Dickey M D *et al*. 2008 Eutectic Gallium-Indium (EGaIn): A Liquid Metal Alloy for the Formation of Stable Structures in Microchannels at Room Temperature *Adv. Funct. Mater.* **18** 1–8

[10] Surapaneni R *et al*. 2011 A highly sensitive flexible pressure and shear sensor array for measurement of ground reactions in pedestrian navigation *The 16th International Conference on Solid-State Sensors, Actuators and Microsystems*, Beijing, China pp. 906-09

[11] Wu H K *et al*. 2003 Fabrication of complex three-dimensional microchannel systems in PDMS J. Am. Chem. Soc. **125** 554–59

CHAPTER 5

A HIGHLY RELIABLE FLEXIBLE TACTILE IMAGER WITH FLOATING ELECTRODE SCHEME

5.1 Introduction

In the previous chapter, we discussed the design and fabrication of an FTI with the implementation of a liquid-metal scheme. The developed FTI was reliable and durable as it could withstand a large number of deformation cycles; however, the FTI failed to present itself as an alternative to other FTI designs due to complicated alignment procedures and electrical connection issues. This chapter will present a viable alternative to all the previous FTIs in the form of a highly reliable floating electrode scheme. A brief description of the concept of the floating electrodes and a proof-of-concept, testing is presented to verify the working principle. After the verification of the proof-of-concept an actual FTI is designed such that the fabrication involves MEMS and flexible printed circuit board (FPCB) techniques. The majority of the FTI is fabricated by standard FPCB manufacturing techniques by a FPCB supplier. This will reduce the fabrication complexity due to the need of less number of in-house fabrication steps (total number of in-house fabrications steps is limited to five steps). Furthermore, the FTI is designed such that it forms a FFC that can be connected to a low-profile flip-lock connector on the

Parts of this chapter are reprinted with permission from [5] of Journal of Micromechanics and Microengineering.

readout circuit. Individual sensing cell and the entire FTI is characterized using a high-speed readout circuit. This chapter will also discuss the FTI's ability to sense the position and motion of line of contact with the ground, when placed at the heel of a boot.

5.2 Floating electrode scheme and proof-of-concept testing

Boie in 1984 first introduced the concept of sensors with implementing floating electrodes [1]. The drive and the sense electrodes are placed on a polymer layer and the floating electrodes rest on the elastomeric dielectric. The floating electrodes split the capacitor into two series capacitors (one from the drive electrode to the floating electrode and the other from the floating electrode to the sense electrode). Since the floating electrodes do not require any wiring, this sensor readout is insensitive to the presence of metallization breaks on the floating electrodes. This is illustrated in the schemes shown in Figure 5.1. In the two-level wiring scheme of Figure 5.1 (a), metal breaks or cracks in the top level directly breaks the electric circuit, thus disconnecting the sensing cell (or consecutive cells) from the readout circuit. Contrary to this scheme, in the floating electrode scheme shown in Figure 5.1 (b), metal breaks or cracks in the top level/floating electrodes split the total capacitance in the sensing cell into multiple smaller ones. Since all of these small capacitors are connected to each other in parallel, the capacitance observed between the drive and sense electrodes remain unchanged. The break resistance comes at the expense of a 50% reduction on the observed capacitance change compared to that of two-level wiring sensors. Boie's original sensors only measured normal stress. Cheng *et al.* [2] modified the sensor to incorporate shear measurements. The modified sensor consists of floating differential electrodes patterned on a PDMS mold which is

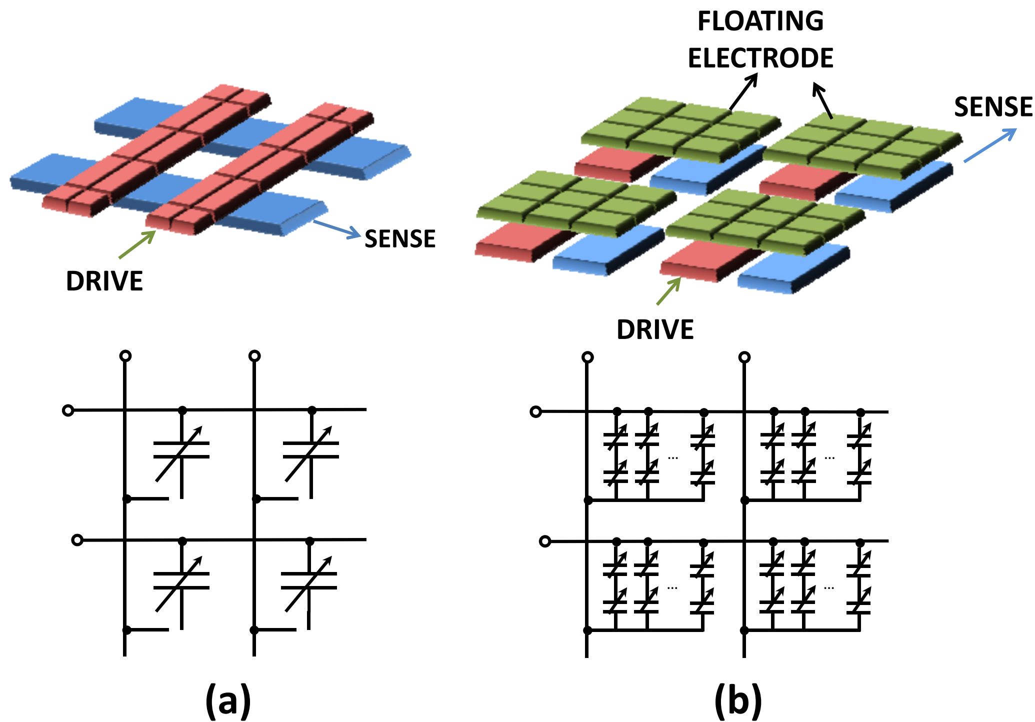

Figure 5.1. Floating electrode scheme. (a) Electrical failure due to cracking of the top layer during load application. (b) Formation of multiple small capacitors due to cracks in the floating electrodes with total capacitance unchanged [3].

then bonded to a flexible PCB layer with the sense/drive lines. Under the action of shear, the two floating electrodes are tilted, thus producing a differential capacitance signal. This type of sensor is, however, unable to measure shear when subjected to combined normal load and shear.

Prior to proposing a new design that will incorporate a floating electrode scheme, a proof-of-concept (POC) test was performed. The cross-sectional view of the device is shown in Figure 5.2. The L-edit layout file for the FTI is shown in Figure 5.3.

The sense electrodes represented in blue (see Figure 5.3) are formed on a Kapton HN-500 substrate. The 125 μm thick Kapton film (5” × 5”) is cleaned in DI water and thoroughly dried. A 20/200 nm Cr/Au layer is deposited by an e-beam evaporator and

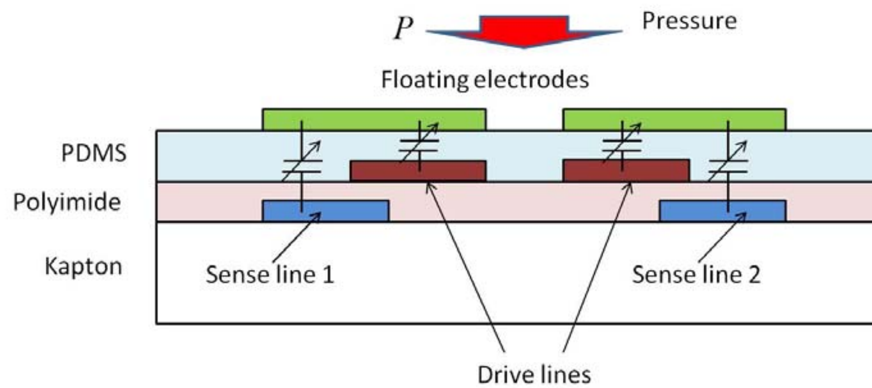

Figure 5.2. Cross-sectional view of the proof-of-concept FTI (POC FTI).

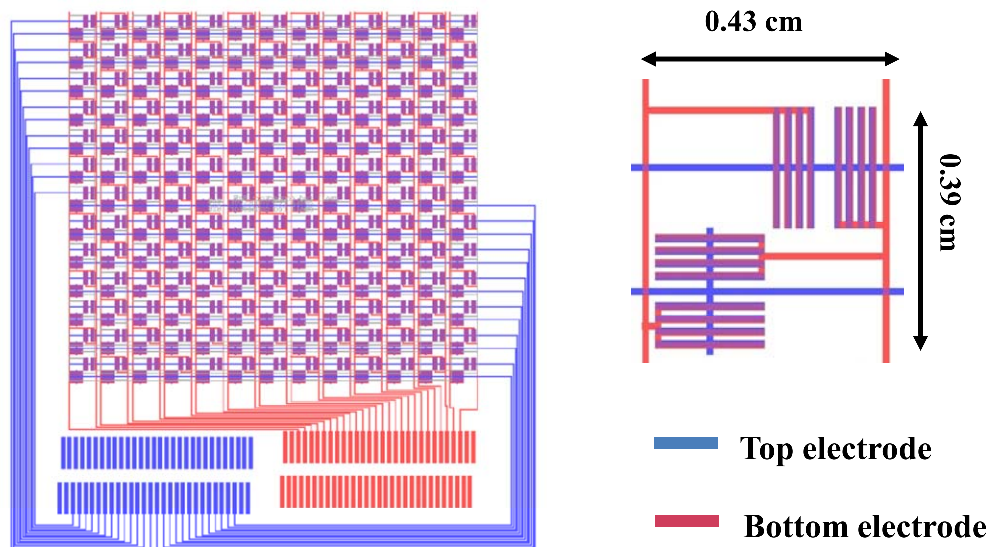

Figure 5.3. Schematic of L-edit layout of the entire POC FTI and individual sensing cell without the floating electrode. Floating electrodes are patterned on each four fingers of every half-cell.

patterned by a lift-off process (as discussed in the section 2.2.2). The adhesion promoter VM-652 is spin-coated on the Kapton film with a patterned metal layer. This improves the subsequent polyimide layer adhesion to the Kapton film. A 10 μm thick polyimide layer (PI2611) is spin-coated at 2800 rpm for 30 s and cured in an oven at 350°C for 30 minutes. Another 20/200 nm Cr/Au layer deposited by e-beam evaporator and patterned by lift-off process forms the drive electrodes (represented in red from Figure 5.3). A 20 μm PDMS layer is next spin-coated after application of adhesion promoter (VM-652). The adhesion promoter also improves the PDMS layer adhesion to the Kapton film. PDMS is cured overnight in an oven at 65°C. Parylene-C (1 μm), that acts as a buffer layer, is deposited over the PDMS after exposing the PDMS to parylene adhesion promoter (silane coating A-174). 200nm aluminum floating electrodes are patterned on top of the parylene layer by e-beam evaporator and lift-off process. A portion of the parylene layer is patterned and etched by oxygen plasma to expose the underlying PDMS over the connector region of the drive and sense electrodes. The remaining parylene layer acts as a mask to etch the exposed PDMS using Tetra-n-butylammonium fluoride. Polyimide etchant (HDMicrosystems, USA) is used to etch the window to access the sense electrodes. Vertical flex cable connectors are bonded and reinforced to the POC FTI near the etched windows to access drive and sense electrodes. The fabricated POC FTI and detailed view of a sensing cell is shown in Figure 5.4.

The capacitance of the individual half-cell is probed with a probe station using a precision LCR meter (Agilent 4284A). Figure 5.5 shows half-cell response to applied pressure. Pressure response of the half-cell is also recorded using a capacitance measurement circuit board and the evaluation software (AD7745/46 evaluation board

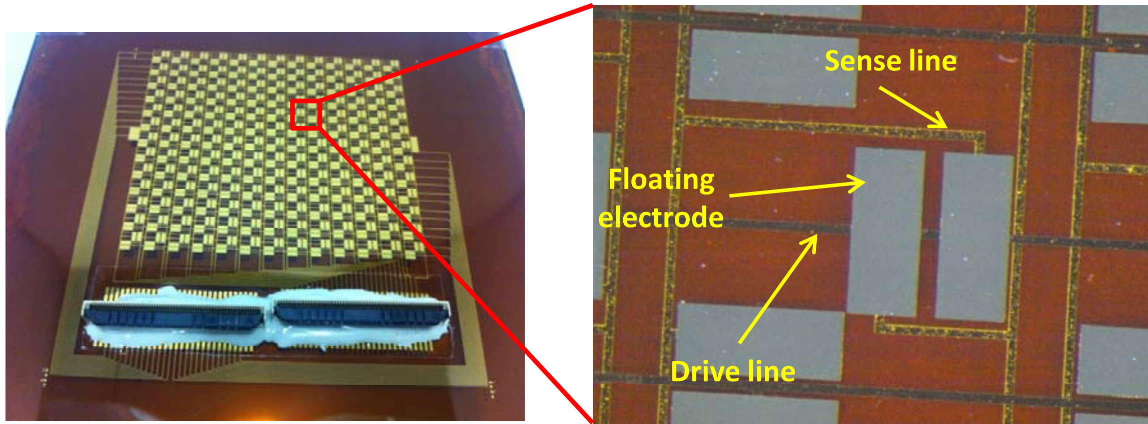

Figure 5.4. Fabricated POC FTI with vertical flex cable connectors and a detailed view of the sensing cell with floating electrodes.

with capacitive length sensor demo, Analog Devices, USA). The applied normal force was measured by a load-cell (Z2S-LM-44, Imada, USA). The testing was performed for a few hundreds of cycles, as shown in Figure 5.6 (a). The POC FTI was then subjected to normal stress by a flat object with a sharp tip on one end of it. The FTI response measured by the readout circuit is shown in Figure 5.6 (b). A brief description of the readout circuit is presented in Section 5.5 and detailed explanation in [4].

Based on the proof-of-concept testing, a flexible tactile imager that can measure both normal and shear stresses using floating electrodes under all load conditions is proposed. The new proposed design consists of comb-like floating electrodes resting on an elastomeric dielectric material with sense and drive lines on the more rigid FPCB substrate. The evolution of the floating electrode scheme (with the capability to measure both pressure and shear simultaneously) from its predecessors is shown in Figure 5.7.

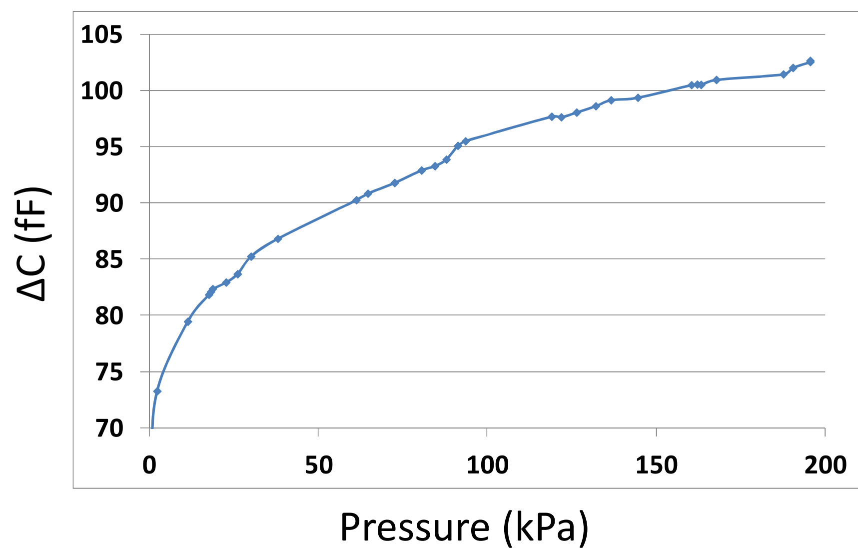

Figure 5.5. Measured half-cell response to applied pressure.

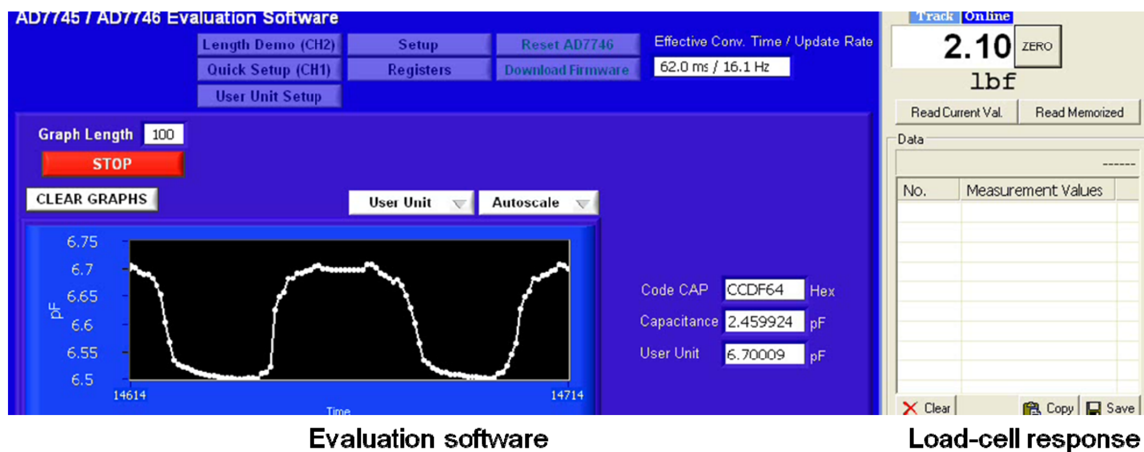

(a)

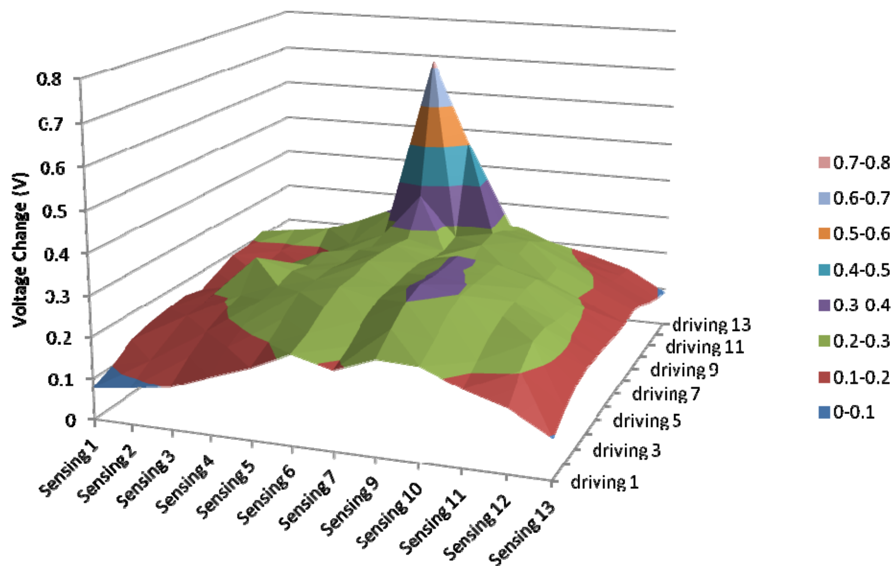

(b)

Figure 5.6. Experimental results for POC FTI. (a) Response of a half-cell displayed by AD7745/AD7746 evaluation software. The applied force on the half-cell is displayed by the load-cell software. (b) POC FTI response when subjected to normal stress by a flat object with a sharp tip on one end of it. The peak displayed is due to the force applied by the sharp tip.

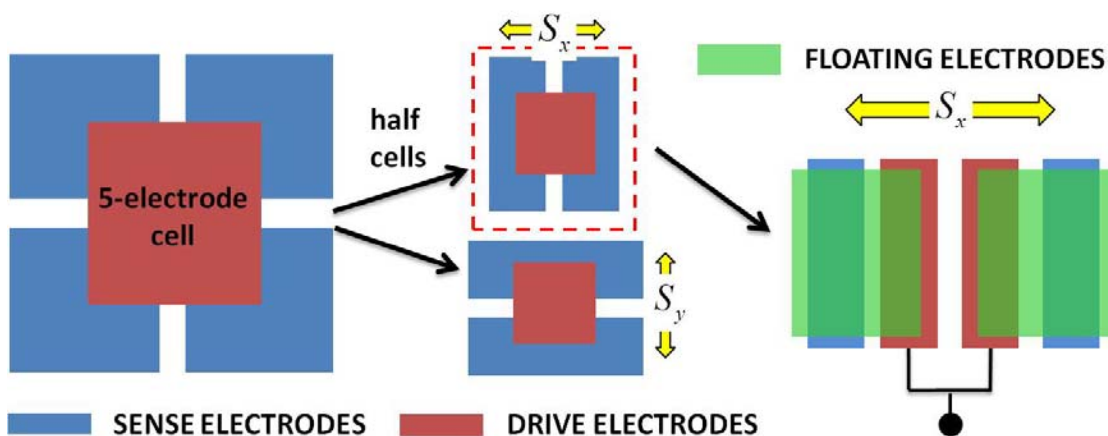

Figure 5.7. Evolution of a floating electrode multifingered structure from a five-electrode cell [3].

5.3 FTI design

The FTI is designed to pack a high-density array of 676 multifingered capacitors in an area of about 53×57 mm^2, thus providing high-resolution images of normal and shear stress distributions. The 676 multifingered capacitors are arranged into 169 sensing cells (four capacitors per sensing cell). A cross-sectional schematic of a sensing cell is shown in Figure 5.8 (a). Each sensing cell measures 4.28×4.16 mm^2, and it is composed of two half-cells called X-cell and Y-cell, as shown in Figure 5.8 (b). The X-cell is orthogonal to the Y-cell and a X-cell can measure shear in X-direction and Y-cell can measure shear in Y-direction (both independently can measure normal stress). Each X-cell and Y-cell consists of two multifingered capacitors. Each multifingered capacitor consists of a comb-like fingered drive, sense and floating electrodes (represented in blue, red and green, respectively). The drive and sense electrodes, each 150 µm wide, are patterned on the same layer of the FPCB, but drive electrodes in the same row are interconnected by the via holes (shown in Figure 5.8 (a)). The length of drive and sense electrodes in a X-

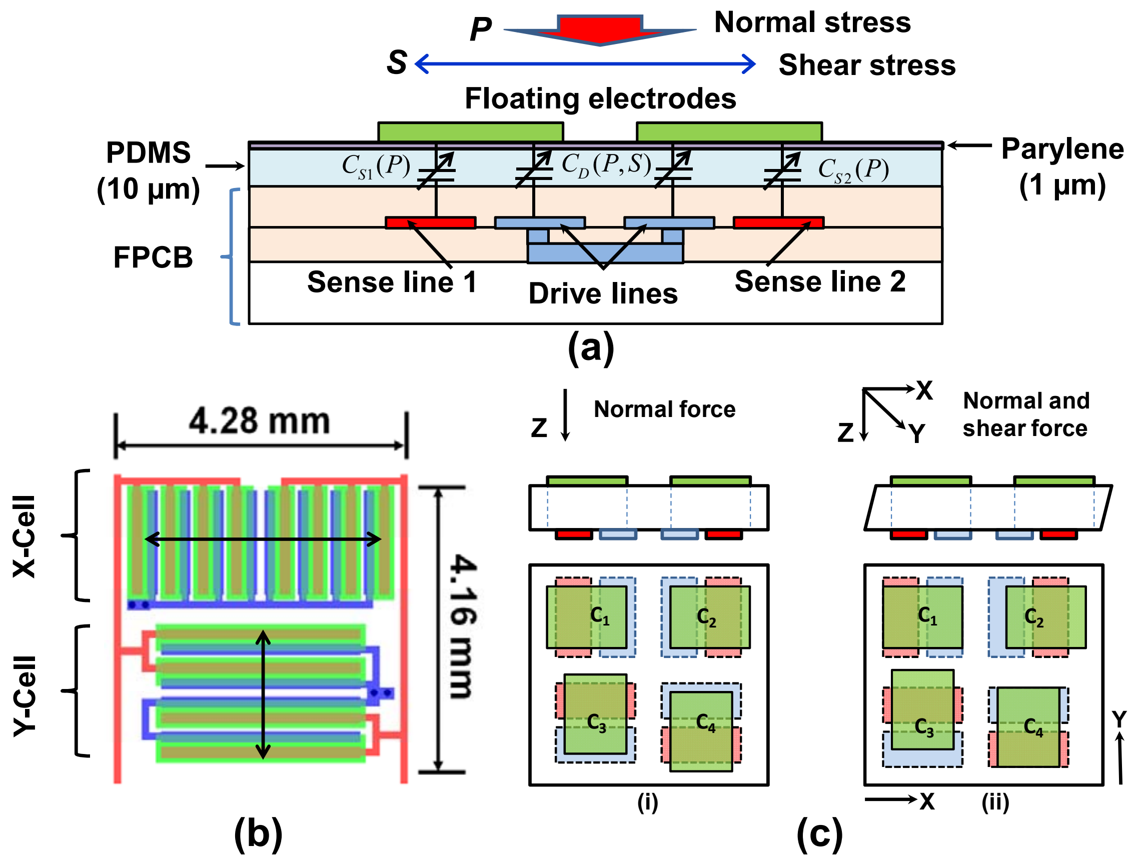

Figure 5.8. Floating electrode scheme. (a) Cross-sectional view of a sensing cell in the FTI with sense, drive and floating electrodes. (b) Each unit cell consists of a X-cell and a Y-cell which measure normal stress and shear in X and Y directions represented by the arrows, respectively. (floating electrodes are represented in transparent green to show the underlying drive and sense electrodes. (c) Capacitances C_1 and C_2 belong to the X-cell C_3 and C_4 belong to Y-cell. For ease of understanding, each capacitor of the sensing cell consists of one finger. (i) A sensing cell under only normal force and (ii) with both shear and normal force [5].

cell varies from a Y-cell such that the nominal capacitance of both match. Each floating electrode (400 µm wide) is patterned on top of a elastomeric dielectric material (such as PDMS) such that it completely covers a finger of the sense electrode and partially covers a finger of the drive electrode, as shown in Figure 5.8 (a) and Figure 5.8 (b). The calculated nominal capacitance for each X-cell/Y-Cell due to these design considerations is 1.2pF. Simulations based on finite element analysis (FEA) revealed 70% of this capacitance is contributed by the floating electrodes and the remaining is due to fringing capacitance. The floating electrode offset with respect to the drive line (represented by dotted line in Figure 5.8 (c)) is responsible for the shear output signal. In a multifingered capacitor, the capacitance is thus formed between the sense fingers and corresponding floating electrodes and floating electrodes and corresponding drive electrodes. In this sensing cell, under normal stress represented by the arrow in Figure 5.8 (c)-(i), capacitance of capacitors C_1, C_2, C_3 and C_4 increases equally. The normal stress is hence measured by capacitance addition of C_1 and C_2 or C_3 and C_4 or all four. When shear in the X-direction alone is applied, in addition to a normal load, the capacitance in C_1 increases but decreases in C_2. Similarly, when shear in the Y-direction is applied, the capacitance in decreases C_3 but increases in C_4. Shear in the sensing cell in a given direction is thus measured by the capacitance difference between C_1 and C_2 or C_3 and C_4, as shown in Figure 5.8 (c) (ii).

The corresponding sensitivities to normal and shear stress for sensing cell (S_P^{Cell}, S_S^{Cell}) are given by:

$$S_P^{Cell} = \frac{1}{C}\left(\frac{\partial C}{\partial P}\right) = \frac{1}{E}, \quad S_S^{Cell} = \frac{1}{C}\left(\frac{\partial C}{\partial S}\right) = \frac{2 \cdot N_f \cdot t}{G \cdot w_f} \tag{5.1}$$

where E and G are the Young's and shear modulus of the compressible dielectric material, t is dielectric thickness, w_f is the finger width and N_f is the number of fingers. While the normal stress sensitivity is independent of the capacitor geometry or area, the shear sensitivity increases with the number of fingers, or the ratio of the cell edge perimeter to the cell pitch. N_f for the X-cell (four) is not the same as N_f for the Y-cell (two). However, the sensing cell is designed to match the nominal capacitances for both half-cells and overlap area of the floating electrode with respect to the drive electrode in both the X-cell and Y-cell is equal.

The addressing of a sensing cell and sensing cell readout of the FTI is performed as shown in Figure 5.9. Because there is no overlap of any two same-axis finger capacitors along the vertical direction, the two orthogonal sensors at each site are interrogated using a dual row select, dual column readout multiplexing scheme developed in [4]. This efficiently reduces the number of required connections to the array and increases array density. The four capacitances of the sensing cell can be measured by individually addressing each of the two blue row lines (A,D) while reading on the vertical red lines (B,C). When row select line A is set to high, row select B is grounded. The pulsed current through capacitors C_1 and C_2 are measured using an integrator circuit discussed in section 5.5 and in detail in [4]. Note that the column readout lines B and C must be set to be virtual ground by its readout circuit in order to eliminate any contributions from C_3 and C_4 in this readout cycle. The readout circuit output would result in 338 normal stress sensing pixels and 169 shear sensing pixels in each direction (x/y).

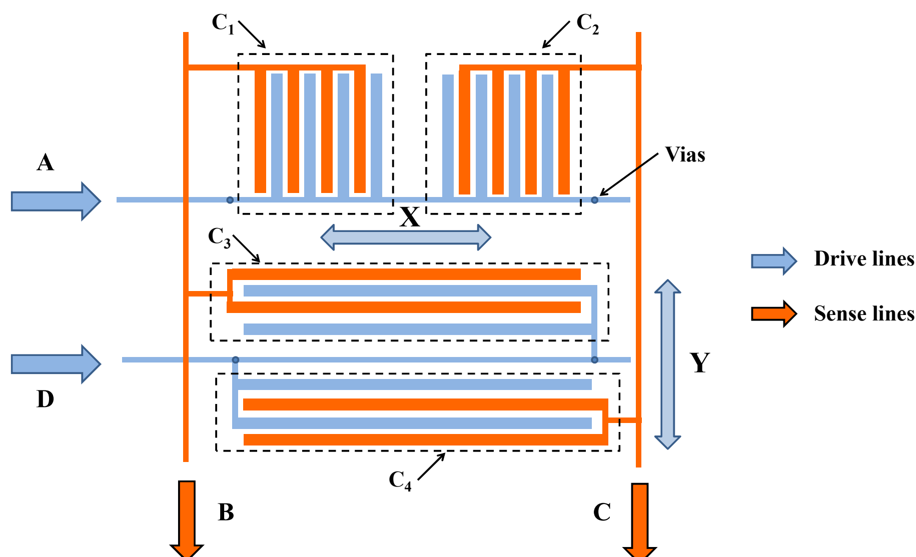

Figure 5.9. Finger structure of a single sensing cell without floating electrodes. The sensing cell is addressed by row drive lines *A* and *B* and readout on virtual ground column lines *B* and *C*.

5.4 FTI fabrication

A combination of flex circuit manufacturing and microfabrication techniques are used to realize the FTI. Figure 5.10 shows a simplified process flow for the fabrication of FPCB and the floating electrode over elastomeric dielectric material. A customized FPCB was manufactured (Uniflex Circuits, Ca) by building a flexible 25 µm Kapton base panel (AP7164E) with 12µm copper (1/3oz/ft^2) hard rolled with dry photoresist (from Dupont) and patterned with the circuit imagery. Drive and sense lines were formed by patterning the copper on the base panel. Another 25µm AP7164E (without copper) was adhered (heat-pressure process) to the existing flex substrate. Later, blind via holes were drilled through the second AP 7164E layer to connect all the drive lines in a row. A second layer of 12µm copper (1/3oz/ft^2) was adhered and patterned using the dry

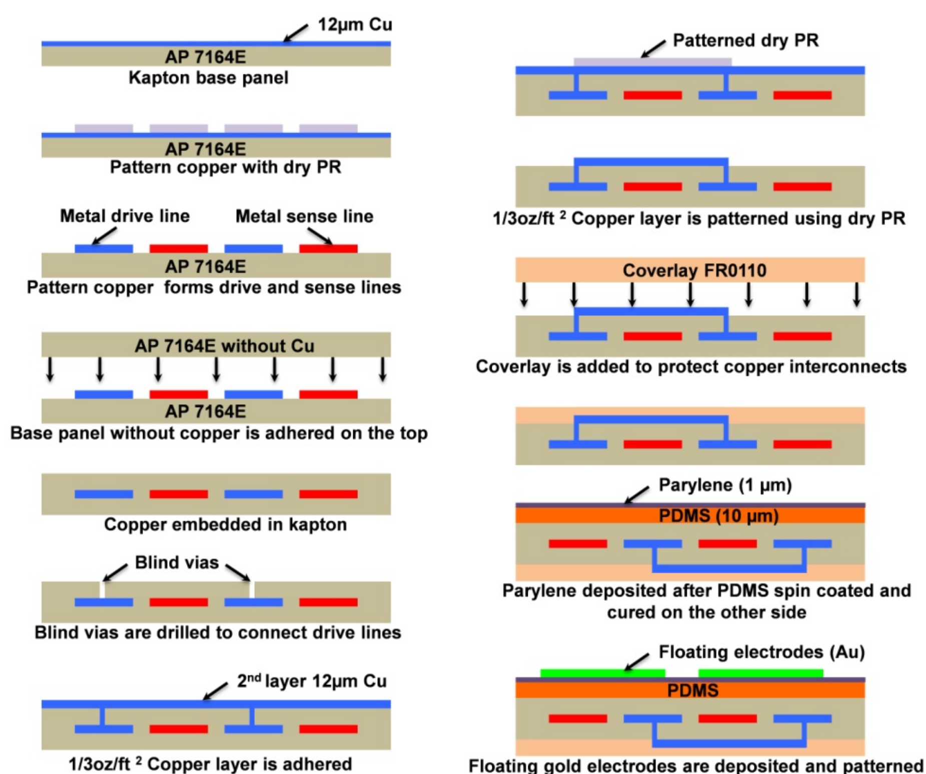

Figure 5.10 Fabrication process flow of the FTI. Last two steps depict in-house fabrication techniques to implement the floating electrodes over the FPCB.

photoresist. The second layer of copper was covered by a 25μm Pyralux FR coverlay (FR0110 from Dupont). This coverlay layer was applied on the entire surface except at the end of the cable to expose the metal lines for linking to a low-profile flip-lock zero insertion force (ZIF) connector (FH29B-120S-0.2SHW(05)) on the readout circuitry. A 0.3 mm stiffener was attached on the other side of the exposed metal, as shown in Figure 5.11 (a). The stiffener provides structural stability and adds required thickness to the end of the cable on the FTI. This ensures reliable connection of the cable with the low- profile flip-lock connector. During the fabrication of the FPCB assembly, the material undergoes multiple heat rolling steps and this may cause FTI shrinkage. Multiple masks to pattern

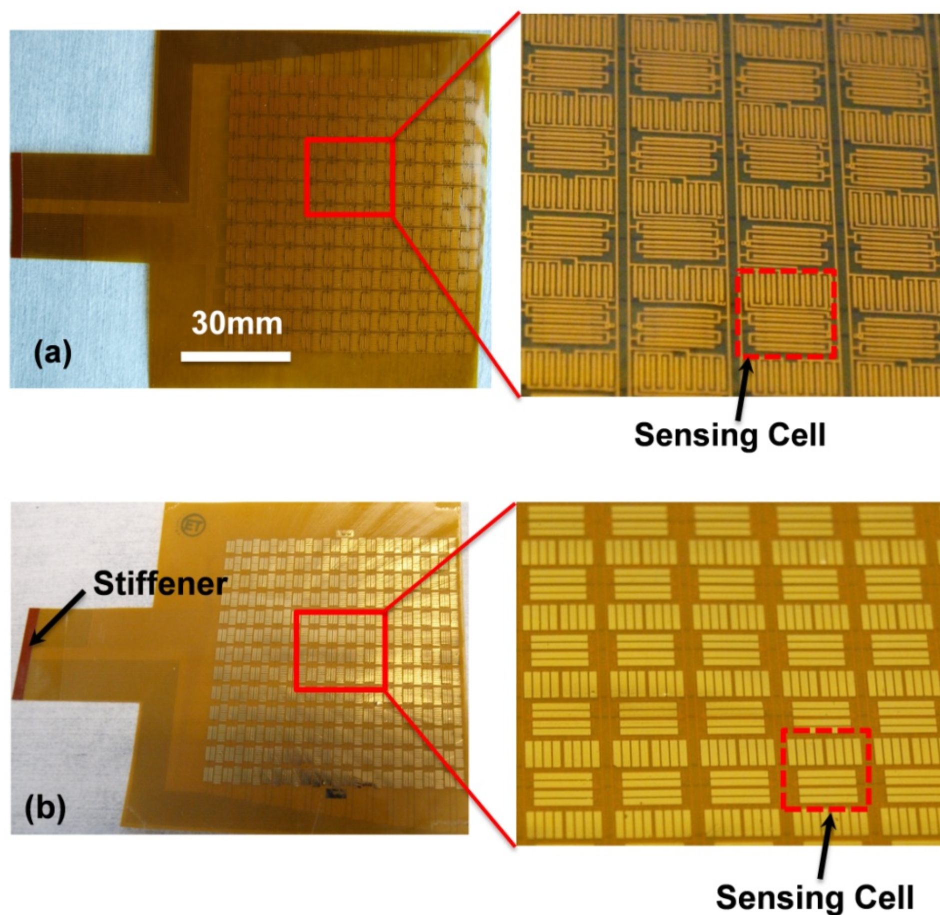

Figure 5.11. Fabricated devices. (a) FPCB and a close-up view of a sensing cell. (b) FPCB with gold floating electrodes patterned on PDMS layer.

the floating electrodes are prepared to compensate for this variable shrinkage and the mask that matches closest is chosen for the floating electrodes. The shrinkage in the FPCB assembly varied from 100 µm to 300 µm. Four masks in increments of 50 µm are prepared to compensate for the shrinkage due to heat cycles. This manufactured FPCB assembly needed further processing to realize the compressible layer and floating electrodes. 15 µm PDMS (Sylgard 184, polymer to curing agent of 10:1) with Young's modulus of ~800 kPa was spin-coated and cured (at 60°C, overnight) on the first layer of AP7164E forming the elastomeric dielectric material. A parylene layer (1 µm) was

deposited on the PDMS using Parylene Deposition System (SCS PDS 2010). A 2 µm photoresist (Shipley 1813) was spin-coated and and backed at 100°C for 5 minutes. It was patterned by a UV light exposure dose of 150mJ/cm^{3} and development using 352 developer. The parylene layer helps in adhesion of the photoresist to the surface. Chromium (20 nm) and gold (150 nm) floating electrodes were deposited by e-beam evaporation. Unnecessary Cr/Au (and underlying photoresist) is removed by ultrasonication of the structure in acetone. The parylene layer also helps adhesion of floating electrode to the structure. Figure 5.11 shows photographs of the three-level metal array. Figure 5.11 (a) shows the FTI without the top floating electrodes. Figure 5.11 (b) shows the FTI with the floating electrodes.

5.5 Readout circuitry

Figure 5.12 (a) shows the basic electronic detection system design architecture, consisting of a front-end multiplexer that can sequentially connect 169 individual sensing cells of the FTI to a capacitance-to-voltage (C/V) converter [6-7], followed by a 12-bit ratio-independent algorithmic analog-to-digital converter (ADC) with a sampling of 66.7 k-samples/s to digitize the output signal. The digital/timing block controls the system timing and also provides digital data with a synchronization clock.

Figure 5.12 (b) shows the schematic of the front-end C/V design. The capacitive sensing units can be configured by the switches to achieve differential shear strain sensing along the x- and y-axes and single-ended z-axis normal stress sensing. The single-ended z-axis normal stress sensing circuitry uses a programmable on-chip reference capacitor to provide a close matching (1.625 pF) to the sensing cell nominal

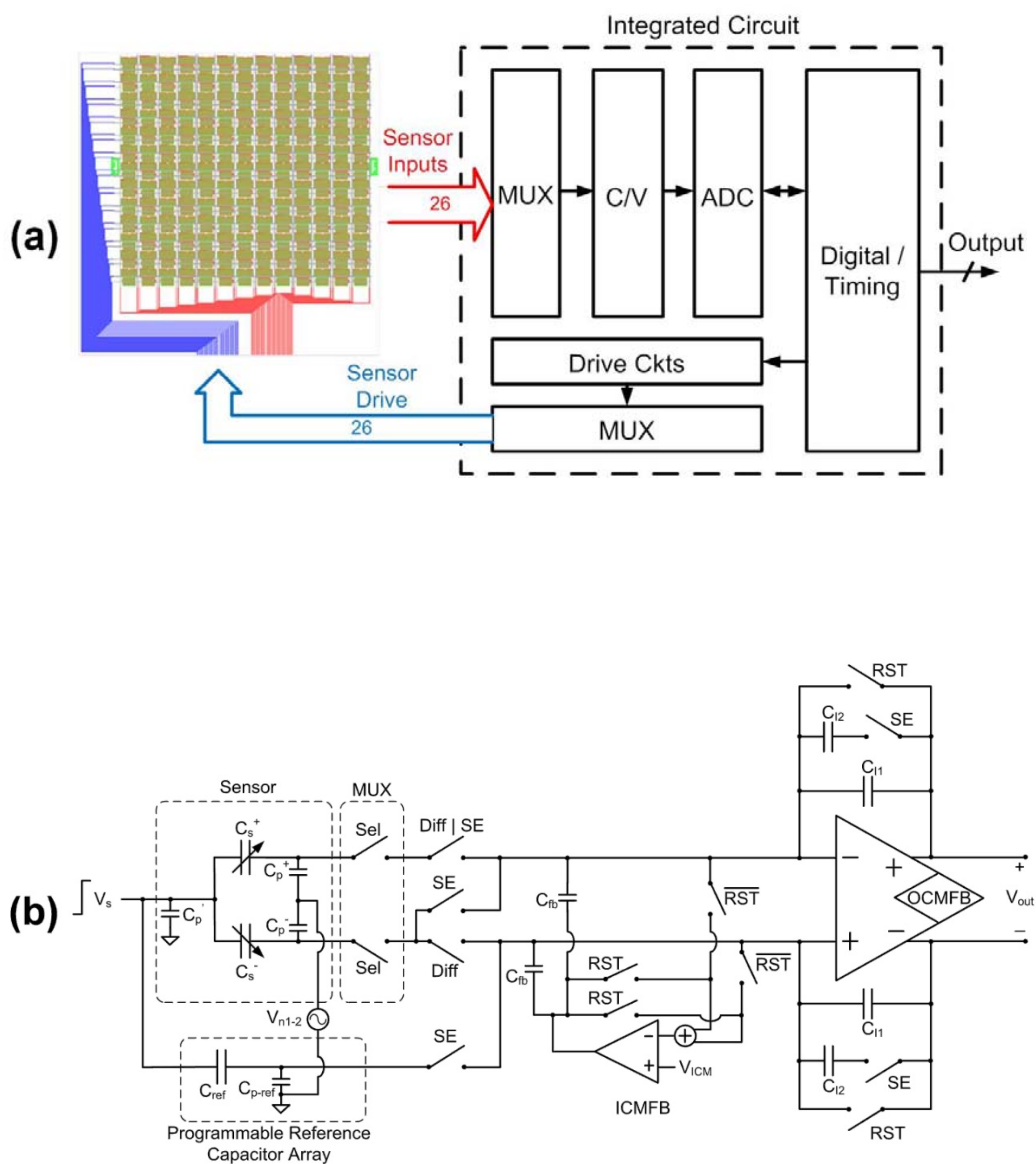

Figure 5.12. Readout circuitry. (a) Schematic of FTI scanning circuit. (b) Schematic of front-end of capacitance readout circuitry.

capacitance value. When the circuit is configured in single-ended mode, the voltage at the output of the first stage amplifier is expressed as:

$$V_{out-Z} = \frac{(C_S^+ + C_S^-) - C_{ref}}{C_{I1} + C_{I2}} \cdot V_S \tag{5.2}$$

When the circuit is configured in differential mode, the output of the first stage amplifier is expressed as:

$$V_{out-X} = \frac{(C_S^+ - C_S^-)}{C_{I1}} \cdot V_S \tag{5.3}$$

where C_s^+ and C_s^- are the sensor capacitances of a single node in the FTI, C_{I1} and C_{I2} are integrating capacitances of the C/V converter, C_{ref} is the programmable reference capacitor and V_s is the stimulation voltage amplitude. The amplifier is a two-stage fully differential design with 129 dB open-loop gain to satisfy requirements for 12-bit settling. The output of the first stage of the C/V converter is further amplified by a factor of 2.5 to achieve a signal amplitude matching the input range of the ADC. A fully differential 12-bit cyclic ADC sampled at 67 k-samples per second is designed to digitize the C/V converter output waveform [8-9]. The system is designed to read the 169 site FTI with a total scanning time of 10 ms. Further details of the readout circuitry are explained by Suster *et al.* [4]. The entire electronic detection system is designed in a 0.35 µm CMOS process while dissipating 3 mW from a 3V supply.

Figure 5.13 shows the customized IC readout board connected to the high-resolution FTI. The output of the FTI is an array of digitized voltages representing capacitance information. This information is converted to normal and shear stress via (5.2) and (5.3) and proportionality constants that are determined experimentally.

5.5 Object motion via centroid interpolation

The FTI can be used to detect the motion of an object placed on top of it, or alternatively the motion of the FTI relative to a stationary object in contact. The latter setup is applicable for measurement of ground velocity with respect to a moving foot, for example as a navigational aid for pedestrian navigation systems. In such an application, the capacitance measurements of the FTI must be converted to object location and velocity. A simple method is realized through the definition of centroid coordinates:

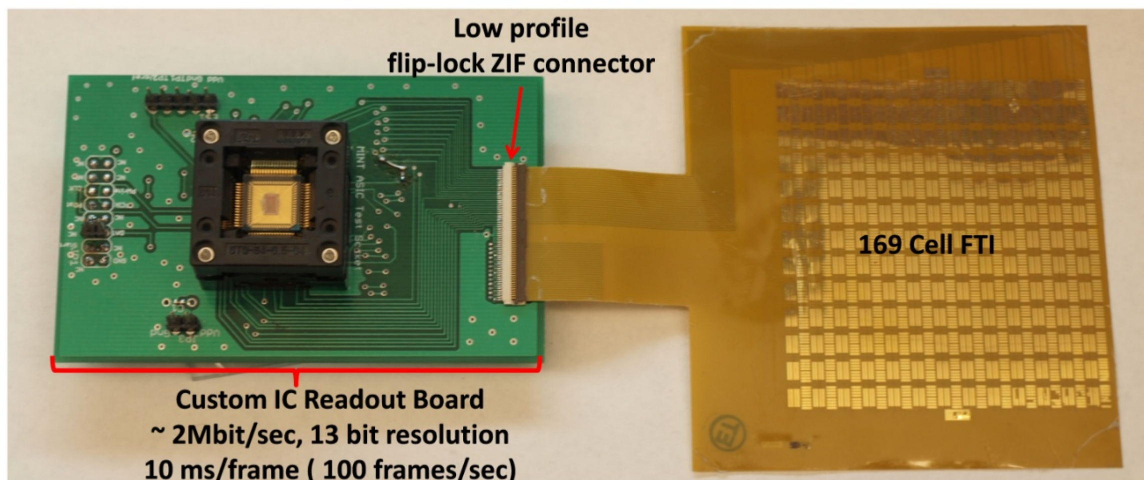

Figure 5.13. FTI connected to the custom IC readout board using a low-profile connector.

$$x_c = \frac{\sum x_i V_i}{\sum V_i}, \quad y_c = \frac{\sum y_i V_i}{\sum V_i} \tag{5.4}$$

where (x_i, y_i) are the coordinates of each sensing cell in the FTI. When the object moves, the capacitor voltages change and so does the centroid location. Equation (5.4) is one of many types of centroids that can be defined, and it works best for objects that have a footprint smaller than the FTI. The object velocity can next be obtained via numerical differentiation of smoothed versions of (5.4) [10-12]. In our implementation, we utilize a fourth-order polynomial fit with regular residual analysis, which provides a smooth estimate of the object velocity.

We also seek a formula that relates the sensing cell pitch and capacitance resolution to object location resolution. We can obtain such formula via interpolation. Let us suppose that an object is rolling on top of the FTI producing a normal stress profile between two adjacent sensing cells, labeled 1 and 2. We wish to define the edge of the object as the location where the normal stress profile is equal to a fixed normal stress threshold P_T. If we assume that the object is large compared to the sensing cell pitch, it approximately produces a linear gradient in normal stress. Due to linear approximation, the edge location is simply:

$$x_e = \frac{P_T - P_1}{P_2 - P_1} \cdot L = \frac{V_T - V_1}{V_2 - V_1} \cdot L \tag{5.5}$$

where x_e is measured with respect to the center of sensing cell 1 and L is the sensing cell pitch. Now we wish to determine the minimum detectable displacement Δx_e and its

relationship to the capacitance (and voltage) resolution of the readout circuitry. If we make the assumption that as the object moves, the normal stress P_2 is constant and if we further assume that $V_1 << V_2$, we can easily show that:

$$\Delta x_e = \frac{\Delta P_2}{P_2 - P_1} \cdot L \approx \frac{\Delta V_2}{V_2} \cdot L = \frac{L}{2^N} \tag{5.6}$$

where N is the number of bits in the readout ADC. The minimum resolvable displacement is thus the sensing cell pitch times the ADC resolution. If the profile spreads over several sensing cells instead of two, equation (5.4) should be modified accordingly, leading to a similar relation.

Using equations (5.4-5.6) we can also obtain estimates for the object velocity. For a given FTI scan time T_s, the minimum detectable average velocity is:

$$(\frac{\Delta x_e}{\Delta t})_{\min} \approx \frac{\Delta x_e}{T_s} \approx \frac{L}{2^N T_s} \tag{5.7}$$

The calculations outlined in equations (5.4-5.7) define a position; therefore, the velocity bound of (5.7) can be used in an averaged sense. The array data tell us that if the object displacement is greater than that specified in (5.6), it will be detected. Note that the above equations are based on an ideal situation, and the resolvable bounds are different than the actual noisy detection limits. When these measurements are subjected to noise and interference, the displacement detection limit becomes:

$$\Delta x_e \approx \frac{\Delta V_2}{V_2} \cdot L = \frac{L}{SNDR} > \frac{L}{2^N} \tag{5.8}$$

The detection limit depends on the overall signal-to-noise and distortion ratio (SNDR) of the system.

The centroid calculated from (5.4) generally is not close to the center of the pressure contours. This is due to the fact the linear centroid calculation pulls the centroid value towards the center of the array. Hence, the calculated centroid seems inaccurate. To avoid this problem, the centroid from the raw data is calculated using the nth order function given by equation:

$$x_c = \frac{\sum x_i V_i^n}{\sum V_i^n}, \quad y_c = \frac{\sum y_i V_i^n}{\sum V_i^n} \tag{5.9}$$

The user is provided with an option to choose a value of *n* to be 2, 4 or 6. The higher the value of *n* is, more is the noise dominance. The value of *n* thus should be carefully chosen to avoid centroid noise, and attain accurate centroid value.

In addition to the calculating centroid from the raw data given by (5.9), the developed software provides a choice of various functions that can be fitted to the data captured given by equation:

$$\in^2 = [\sum_{i=1}^{n} \sum_{j=1}^{n} (V_{i,j}) - f(a,b,c,...x_i, y_j)]^2 \tag{5.10}$$

These functions ($f(a,b,c,\ldots x_i,y_j)$) include reduced quadratic, full quadratic and bicubic fit functions. The functions represented by each fit is given by (5.11), (5.12) and (5.13), respectively.

$$f(a,b,c,\ldots x_i,y_j)=a(1)+b(x_i)+c(y_j)+d(x_i\cdot y_j)+e(x_i)^2+g(y_j)^2 \tag{5.11}$$

$$\begin{gathered}f(a,b,c,\ldots x_i,y_j)=a(1)+b(x_i)+c(y_j)+d(x_i\cdot y_j)+e(x_i)^2+g(y_j)^2+h(x_i^2\cdot y_j)+\\ k(x_i\cdot y_j^2)+l(x_i^2\cdot y_j^2)\end{gathered} \tag{5.12}$$

$$\begin{gathered}f(a,b,c,\ldots x_i,y_j)=a(1)+b(x_i)+c(y_j)+d(x_i\cdot y_j)+\\ e(x_i)^2+g(y_j)^2+h(x_i^2\cdot y_j)+k(x_i\cdot y_j^2)+l(x_i^2\cdot y_j^2)+m(x_i)^3+\\ n(y_j)^3+o(x_i^3\cdot y_j)+p(x_i\cdot y_j^3)+q(x_i^2\cdot y_j^3)+r(x_i^3\cdot y_j^2)+s(x_i^3\cdot y_j^3)\end{gathered} \tag{5.13}$$

Once the date is fitted to the functions, centroids are numerically calculated from the minimum of the fitted data.

5.6 Experiments and results

The experimental setup consists of a normal stress measurement system that is used to characterize normal stress on the entire FTI and a shear measurement system, which is used to characterize shear on individual sensing cells of the FTI. Each of these systems is explained in the sections 5.6.1 and 5.6.2.

5.6.1 Normal stress measurement system

Figure 5.14 (a) shows the custom experimental setup built to characterize normal stress acting on the FTI. The system consisted of two main components, (1) a normal stress application setup and (2) a motorized stage. The normal stress application setup consists of a translation stage setup vertically with a metal plate at 90° angle. This setup can move in Z-direction for application of normal load. The load is applied on a rectangular acrylic block ($30\times17.8\times14$ mm^3) resting on the FTI with the help of a screw gauge. The load applied on the block is measured by resistive load cell (RSP1-050M-A*C01, Loadstar Sensor, CA) placed on the bottom side of the metal plate, as shown in Figure 5.14 (a). The FTI is placed on a movable stage that is on a single-axis stepper motor. Using this setup, the voltage change versus applied load on an area covering six sensing cells is obtained and Figure 5.14 (b) presents the voltage change variation from cell to cell. The data are obtained from a software presented in Appendix A (the software is not only capable of mapping pressure contour but also capable of recording the pressure and shear values of every sensing cell in each frame). Initially, the measured voltage change is high for small stress, and the slope is reduced as the PDMS becomes stiffer with increasing stress. From the output voltage change, the Young's modulus of the elastomeric PDMS layer can be calculated and a relationship between Young's modulus and normal stress is plotted in Figure 5.15. The plot suggests that PDMS exhibits a highly nonlinear stress-strain relationship/Young's modulus and could be due to its visco-elastic nature [13]. Also, some of the initial surge in voltage change can be attributed to cross coupling of the dielectric acrylic block that is used to apply load on the FTI. Calculations showed ~0.2 V output voltage change just by contact of a material (of dielectric constant

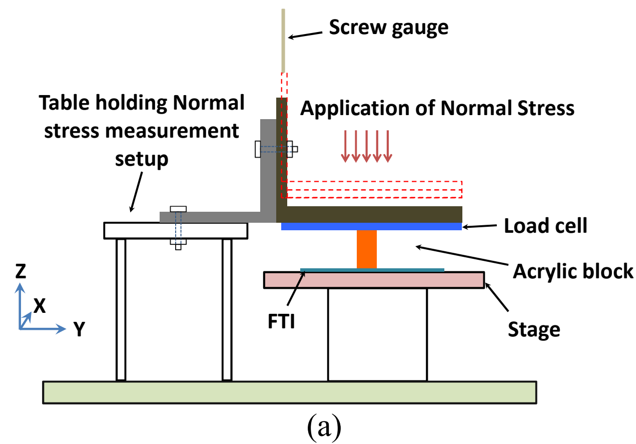

(a)

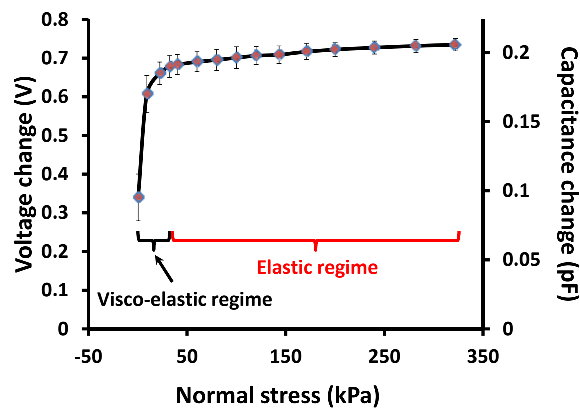

(b)

Figure 5.14. Experimental setup and results. (a) Schematic showing the normal stress measurement system. (b) Voltage change and capacitance change for 6 cells under uniform normal stress.

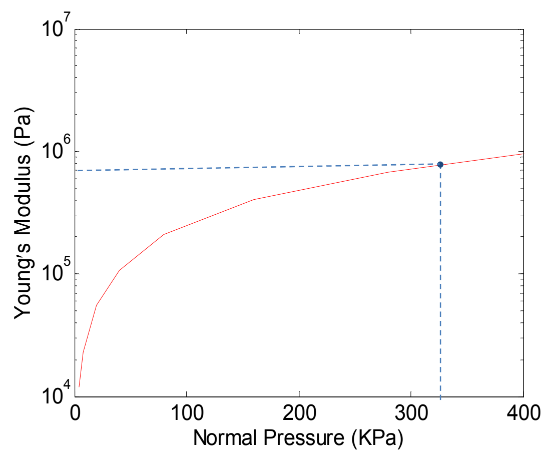

Figure 5.15. Change in Young's modulus of PDMS with change in applied normal stress.

3.1). Initially (<10 kPa), the sensitivity of the sensing cell is high and reduces with increasing normal stress. The Young's modulus is about 20 kPa for an applied normal stress of 8kPa and reaches to about 1 MPa for 400 kPa normal stress. The measured nominal capacitance of each X-cell/Y-cell is 1.65 pF. The additional capacitance (compared to calculated value) is likely contributed by residual parasitic capacitance associated with the measurement setup and/or reduced dielectric layer thickness during fabrication process. The change in capacitance due to a normal stress of 320 kPa (corresponding to the weight of a human ~100 kg) is 201 fF (a maximum capacitance change of 10% under maximum load). The young's modulus corresponding to the human weight (320 kPa) is about 760 kPa (shown in Figure 5.15) which is in agreement with previous published data [14]. The cumulative normal stress sensitivity for the sensing cell in visco-elastic and elastic regime thus calculated is 0.74/MPa comparable to similar structure (without floating electrode) [16]. The pressure sensitivity in the visco-elastic regime and elastic regime are 6.4/MPa and 0.11/MPa, respectively.

In order to achieve statically increasing normal stress, first the acrylic block is replaced by a soft ball (shown in Figure 5.16 (a)) and then gradually rotating the screw gauge pushes the metal plate with the load cell downward (in Z-direction) increasing the normal stress, causing the soft ball to deform and increase the area of contact. The response of the FTI array to different increasing normal stresses is shown in Figure 5.16 (b). Pressure contours at different time intervals are plotted using custom software (see Appendix A). Note that as the normal stress increases the number of response contours increases.

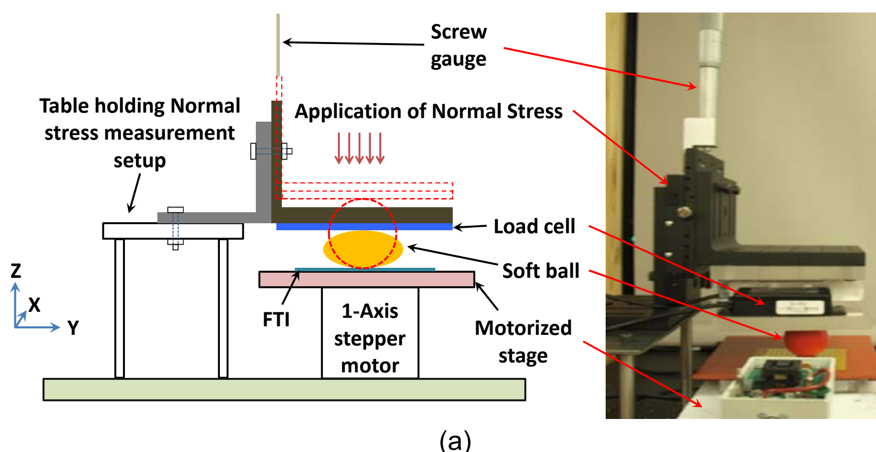

(a)

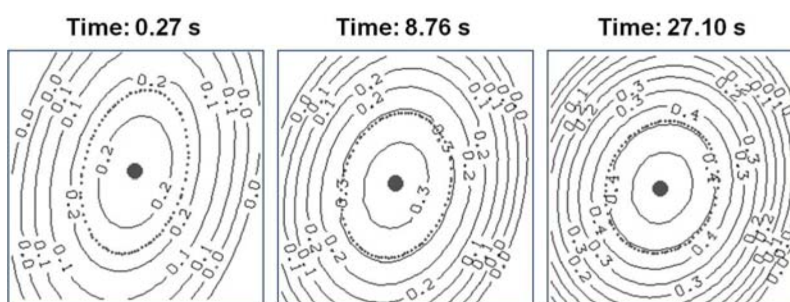

(b)

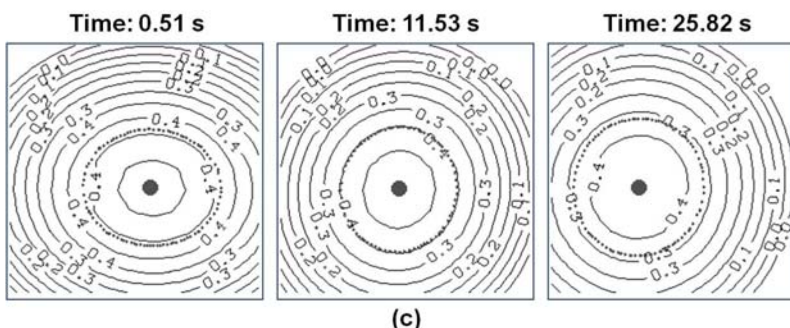

(c)

Figure 5.16. Experimental setup and results. (a) Schematic of the normal stress measurement system with a soft ball applying normal stress on the FTI. (b) Pressure contour of tactile imager under increasing normal stress of a fixed soft ball at different time intervals. (c) Pressure contour of tactile imager under constant normal stress of a rolling ball at different time intervals (the images represent the ball rolling at the center of the FTI). The dotted line in each of (b) and (c) represent the 90% contour of the normalized FTI data. The centroid is the calculated center of the dotted contour line. This method for centroid calculation produced the least jitter in the centroid data.

Another custom software was built to capture the data from the readout circuit (see Appendix B.1). The captured data are then plotted using a matlab program from Appendix B.2. Different forces exerted by the soft ball and its pressure profile are shown in Figure 5.17.

The response of the FTI to a rolling ball is measured. Rolling normal stress is achieved by applying a known load on the FTI while moving the stage along the X-direction using the single-axis stepper motor to articulate a rolling motion. The stage is controlled by a stepper motor board (1063- PhidgetStepper Bipolar 1-Motor, Phidgets Inc., Canada). A custom software is developed (see Appendix C) to control the stepper

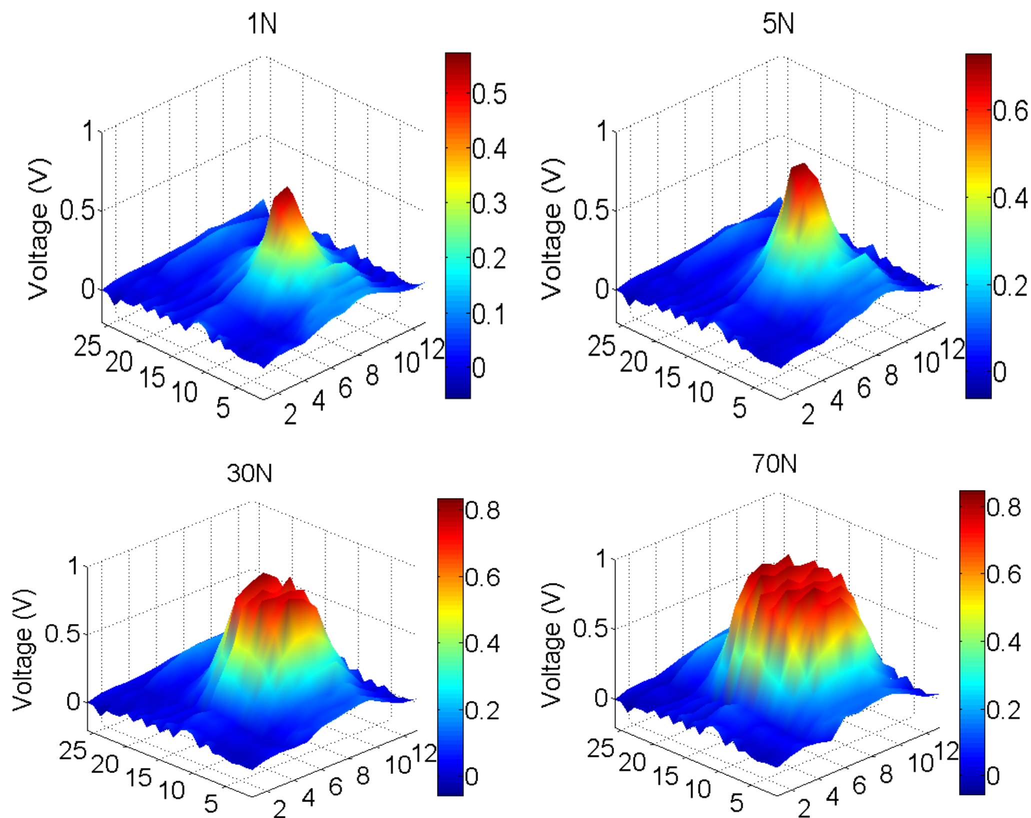

Figure 5.17. FTI response to different forces exerted by a soft ball [17].

motor via the control board. The stage moved a total of 150 mm, and the rolling ball contour is captured using the same custom software (discussed in Appendix A). Figure 5.16 (c) shows the ball rolling on the center of the FTI. Centroid position and velocity are calculated and displayed in Figure 5.18, where Cen_x and Cen_y represent the centroid position along X and Y axes, respectively, and Vel_x and Vel_y represent the velocity along X and Y axes, respectively. The ball rolled over the FTI with a velocity of about 4 mm/s, which is about the same as the single-axis stepper motor velocity. The calculated minimum resolvable displacement from equation (5.6) is 2.0µm. The minimum detectable displacement as measured by placing a stationary ball on the FTI (without increasing normal stress or rolling normal stress) is 60 µm, as shown in Figure 5.19. The variation of the centroid position is calculated and found to be 20 μm_{RMS}. This corresponds to a microvelocity sensing resolution of 100 µm/s. This value could improve with smaller pitch size of the sensing cell. The difference between the minimum resolvable and detectable displacement is caused by a measured electrical interference noise of approximately 5 mV in the system.

5.6.2 Shear stress measurement system

The shear experimental setup of Figure 5.20. (a) was built to measure shear forces in a single sensing cell of the FTI. The setup consisted of two main components (1) a shear application setup and (2) motorized stage. The shear application system used a metal L-joint with a flat rubber end-cap attached to a vertically mounted load cell (TUF-002-001-a*C01, Loadstar Sensor, CA). The rubber end cap helps in avoiding metal contact to the Au floating electrodes and also helps in providing sufficient friction to generate shear.

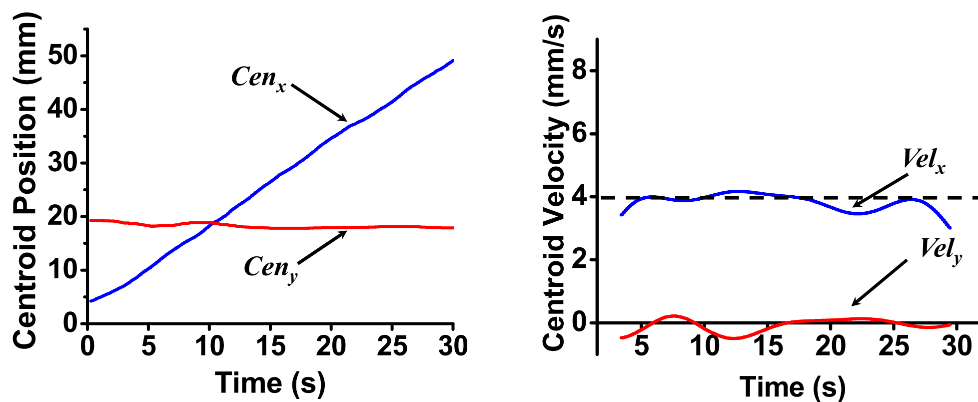

Figure 5.18. Calculated centroid position and centroid velocity of the rolling ball on the FTI. The dotted line represents the velocity of the stage.

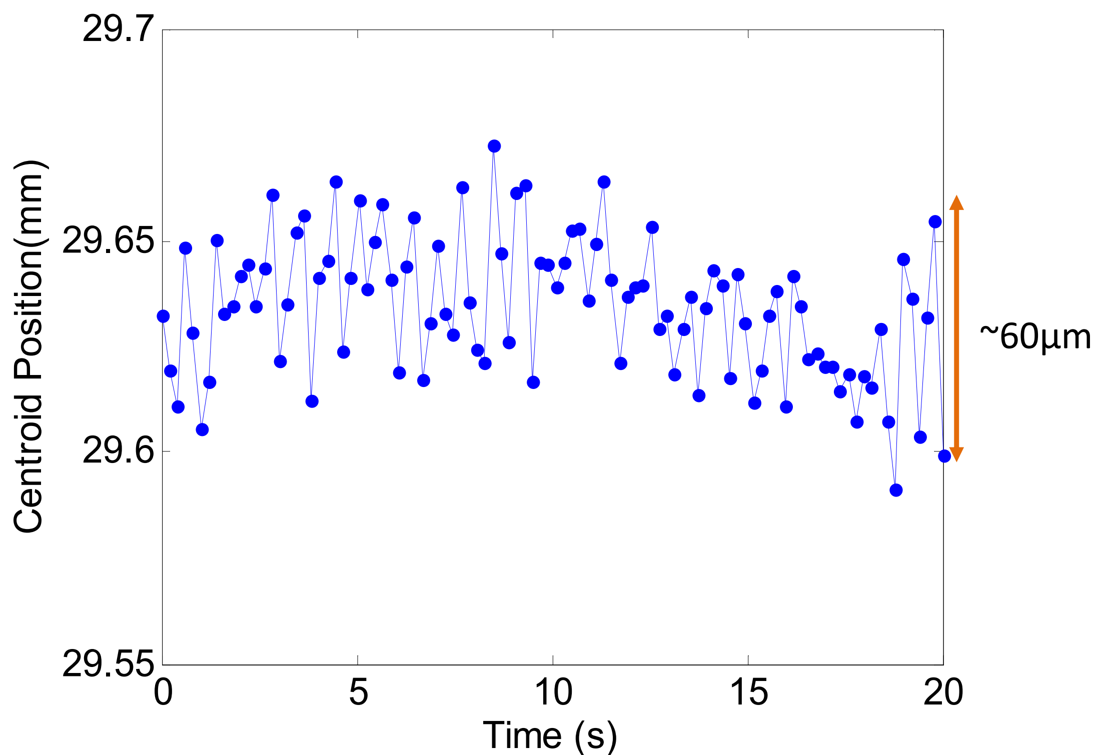

Figure 5.19. Variation of the centroid position of a stationary object over time [17].

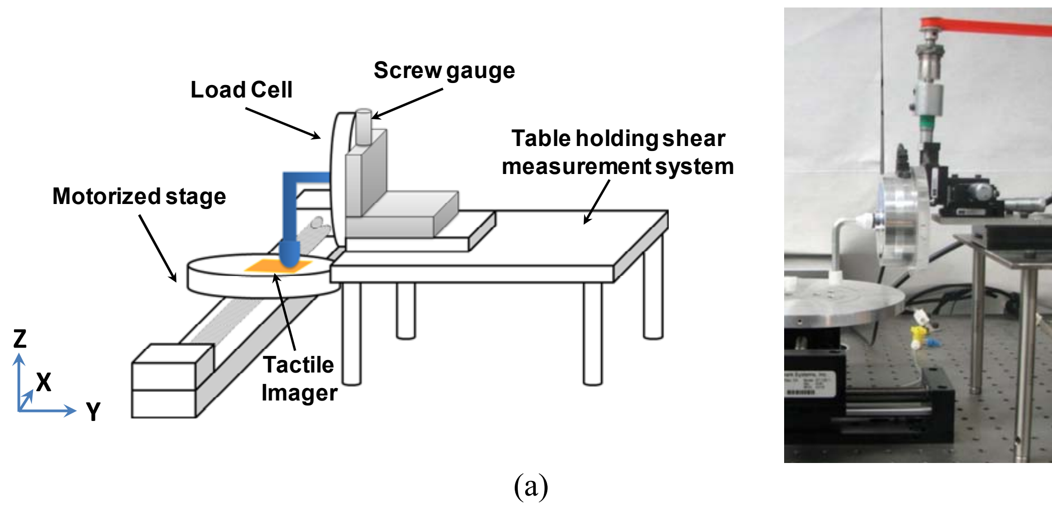

(a)

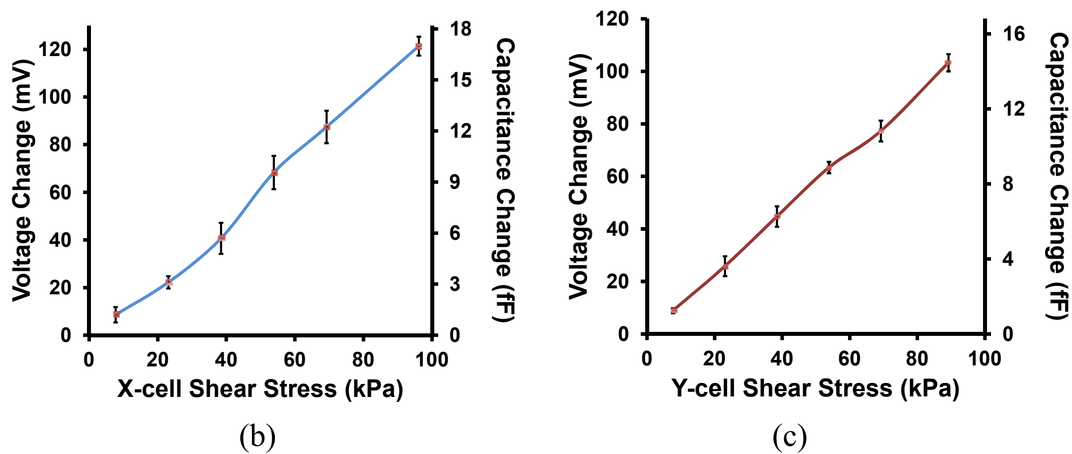

(b) (c)

Figure 5.20. Experimental setup and results. (a) Schematic showing the shear stress measurement system. (b) Voltage and capacitance change for a X-cell at various shear stresses applied in x-axis. (c) Voltage and capacitance change for a Y-cell at various shear stresses applied in y-axis.

Shear measurements were performed as follows. First, a known normal load was applied on the FTI (by moving the L-joint downward in Z-direction), and the reading on the load cell was reset to zero. Then, the single axis stepper motor moved the stage in small increments (in X-direction) in order to apply shear on the FTI. Shear values from the load cell and changes in output voltage value from the readout circuitry are plotted in Figure 5.20. (b) and Figure 5.20. (c) using the software presented in Appendix A. Since the readout circuitry measures the differential value of capacitances in the corresponding X-cell/Y-cell, the output voltage is independent of applied normal stress. In order to maintain sufficient friction between the rubber end-cap of the L-joint and the FTI top surface, the normal stress needs to be greater than 100 kPa. From the change in voltage versus nominal stress data, it is evident that the visco-elastic regime of PDMS does not exist after ~20 kPa (change in voltage is very small compared to load applied beyond 20 kPa). A comparison study of output voltages versus shear stress at various normal load conditions (>100 kPa to ensure friction) shows similar results, as shown in Figure 5.21. For the same nominal capacitance of 1.65 pF, the capacitance change due to shear stress of 128 kPa is 16.8 fF (a maximum capacitance change of 1% under maximum shear).

Shear modulus at various shear stress is plotted in Figure 5.22, revealing an average shear modulus of 240 kPa over the testing range (which is in agreement with [15]). The sensitivity of shear is calculated to be 79.5/GPa, which is slightly lower than similar structures (without floating electrode) [16]. This lower sensitivity of shear compared to [16] is due to the more number of fingers and bigger sensing cell size. Hysteresis analysis of the sensing cells for both normal and shear stresses is crucial; however, the experimental setup built in-house did not permit for such analysis. Tactile sensors

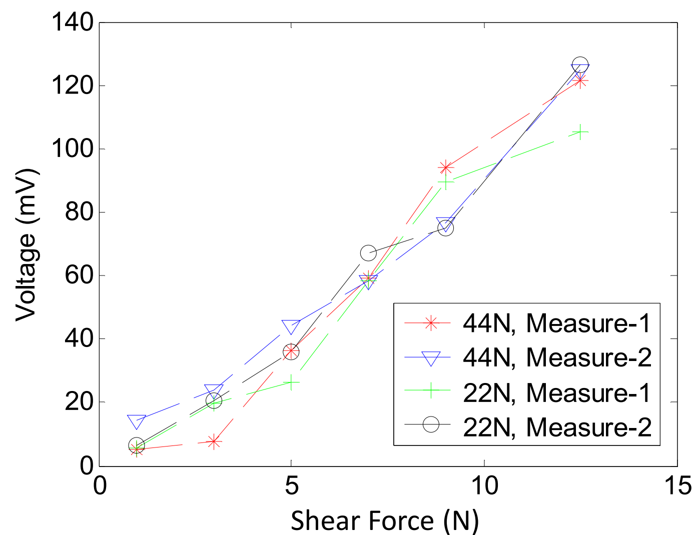

Figure 5.21. Change in voltages for an X-cell at different shear forces under two different normal loads (44 N and 22 N).

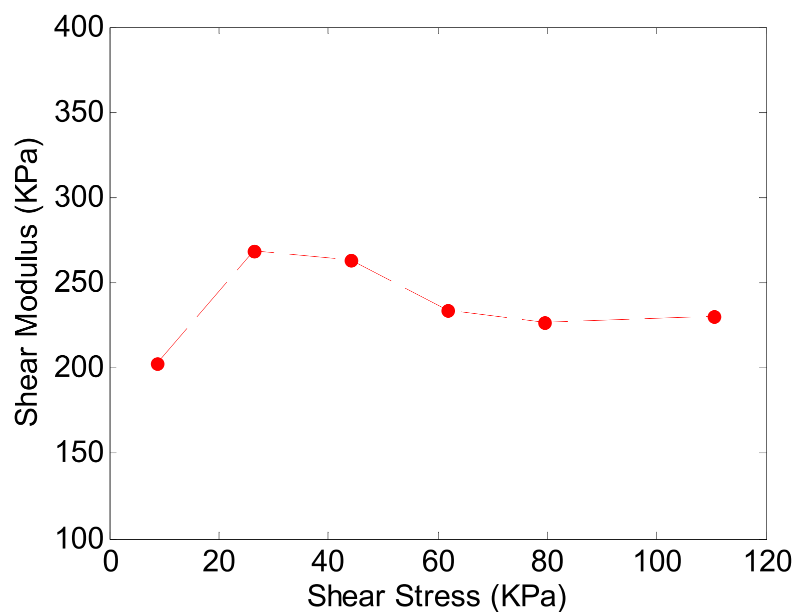

Figure 5.22. Change in shear modulus of PDMS with change in applied shear stress [17].

developed with PDMS as the elastic dielectric material demonstrated no appreciable effects. Next, the soft ball was placed on the FTI and manually twisted with increasing shear. The shear contours thus obtained (using the software presented in Appendix D) with respect to time are shown in Figure 5.23.

The FTI was tested for several hundreds of hours using a soft ball and loading and unloading using acrylic block. The FTI exhibited four different rows and three different columns broken after such elongated testing. It is assumed that the FTI could have failed near the cable end (close to the connector) due to constant usage of the flip-lock connector. To overcome this problem, future FTI designs can be implemented with the readout circuit placed directly on the FTI.

5.6.3 Testing during walk

In our final test, the FTI was mounted close to the rubber heel of a shoe (about 1 cm away from the ground). Real-time normal stress images were recorded while a person was walking on the FTI. The FTI was first enclosed in a 0.5 cm thick PDMS layer and

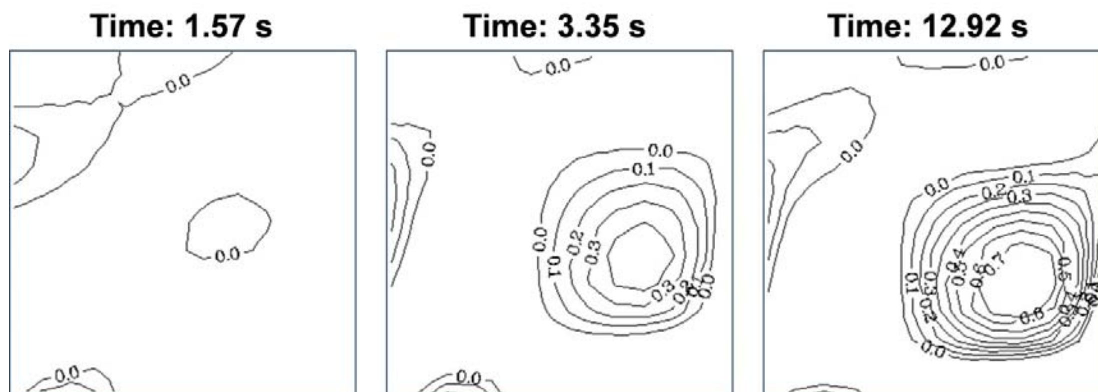

Figure 5.23. Shear contour of tactile imager under increasing shear applied on the soft ball at different time intervals.

then the outside of PDMS is wrapped with a layer of aluminum foil. The aluminum foil was grounded to provide a shielding layer from the parasitic capacitance of the human body (aluminum foil, 0.5 cm away from the FTI did not influence the output voltage). Figure 5.24 represents the centroid of the normal stress applied by the foot on the FTI. The centroid moved from the top end to the center while the foot position moved from heel strike to push off, shown in Figure 5.24. (b-e). Figure 5.25 shows the calculated centroid position and velocity with respect to time for two consecutive steps during the walk. From Figure 5.25, it can be inferred that the minimum velocity during walk occurs during midstance just before push-off (similar results were observed in [18-19]). Approximate walk velocities can also be obtained from the centroid velocities calculated previously. From the average velocity for the 2 steps shown in Figure 2.25, the angular velocity of the heel rolling on top of the FTI was calculated to be ~0.3 rad/s.

Assuming that the torso is 0.85 m away from the FTI, a walk velocity of 267 mm/s was calculated from the FTI data. This compares to an averaged walk velocity of 345 mm/s (measured by timing a walk of 4 m). The FTI information can thus be used to estimate the approximate velocity of the person and distance covered during a walk. Such auxiliary measurements can be utilized in aiding pedestrian navigation systems [18-19].

5.7 Summary

A highly reliable FTI with the floating electrode is successfully fabricated and tested. This system is proved to be a suitable candidate for detail measurements of reaction forces in robotic grippers and gait analysis. Each sensing cell consists of combed drive

(a)

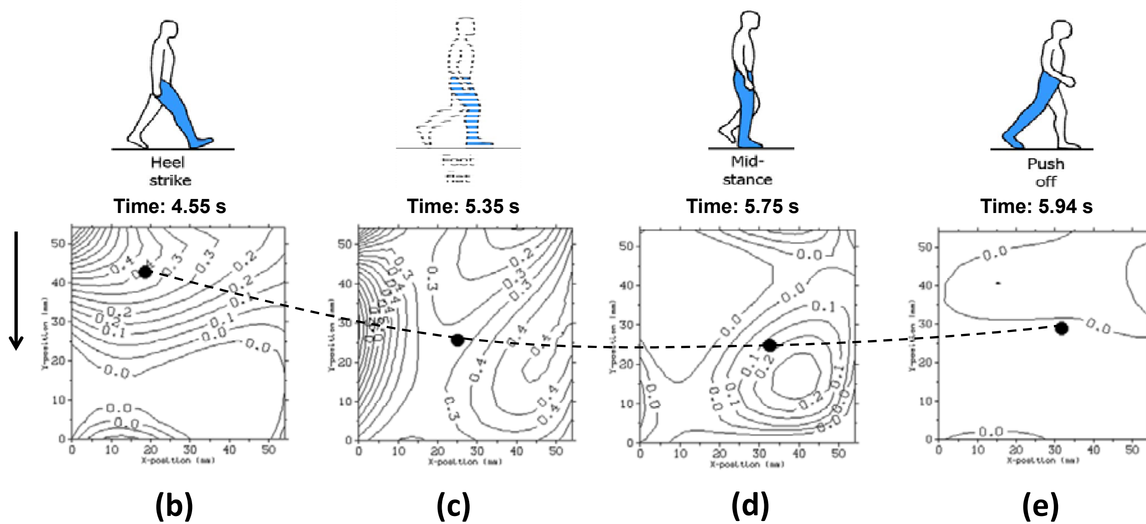

(b) (c) (d) (e)

Figure 5.24. Testing during walk. (a) Shows the shoe used for gait measurements. Measured experimental pressure contour corresponding to the key frames within a single step including: (b) heel strike, (c) foot flat, (d) midstance and (e) push off. The dot in each pressure contour map indicates the normal stress centroid and the arrow (on left of (b)) represents the direction of motion of the centroid during a single step.

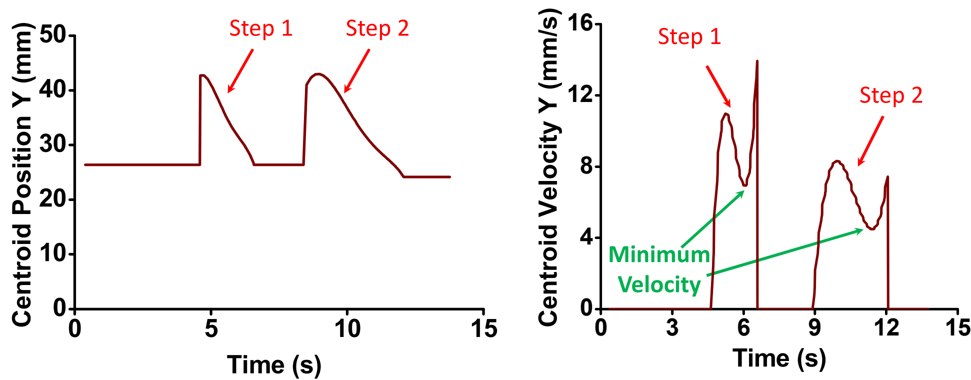

Figure 2.25. Calculated centroid position and velocity during two consecutive steps on the FTI.

and sense electrodes in the FPCB and floating electrodes placed at an offset on an elastomeric dielectric material spin-coated over the FPCB. The design incorporates multiplexing such that it reduces complexity of the tactile imager while maintaining high-resolution due to compactly packing 676 capacitors in about 53 X 57 mm^2. The readout circuitry and customized software are capable of measuring a statically increasing, rolling normal stress and applied shear on the FTI. The nominal capacitance of the X-cell/Y-cell in the FTI is 1.65pF and the normal and shear stress sensitivities for the FTI are 0.38/MPa and 79.5/GPa, respectively. The minimum resolvable object displacement measured by the FTI is as low as 60µm due to the system output voltage interference of 5 mV. Finally, the FTI is successfully used to capture pressure contours during walk and points of minimum velocity are obtained for each step during the walk.

5.8 References

[1] Boie R A 1984 Capacitive impedance readout tactile image sensor *Proc. IEEE Int. Conf. Robotics and Animation.* **1** 370-78

[2] Cheng M Y, Lin C L and Yang Y J 2010 Tactile and shear stress sensing array using capacitive mechanisms with floating electrodes *MEMS'10: IEEE 23rd Int. Conf. on Micro Electro Mechanical Systems* 228–31

[3] Surapaneni R, Xie Y, Guo Q, Young D J and Mastrangelo C H 2011 A high-resolution flexible tactile imager system based on floating comb electrodes *IEEE Sensors 2012* pp. 1-4

[4] Suster M, Mastrangelo C H and Young D J 2010 Low-Interference Sensing Electronics For High-Resolution Error-Correcting Biomechanical Ground Reaction Sensor Cluster *Proc. IEEE Sensors*. 1020-23

[5] Surapaneni R, Guo Q, Xie Y, Young D J and Mastrangelo C H 2013 A three-axis high-resolution capacitive tactile imager system based on floating comb electrodes *J. Micromech. Microeng.* **23** (2013) 075004

[6] Enz C C and Temes G C 1996 Circuit techniques for reducing the effects of op-amp imperfections: autozeroing, correlated double sampling, and chopper stabilization *Proc. IEEE* **84** 1584-14

[7] Oliaei O 2003 Noise analysis of correlated double sampling SC integrators with a hold capacitor *IEEE Transactions on circuits and systems I* **50** 1198-02

[8] Li P, Chin M J, Gray P R and Castello R 1984 A ratio-independent algorithmic analog-to-digital conversion technique *IEEE J. Solid-State Circuits* **19** 828-36

[9] Ginetti B, Jespers P and Vandemeulebroecke A 1992 A CMOS 13 bit cyclic RSD A/D converter IEEE J. Solid-State Circuits **27** 657-65

[10] Savitsky A and Golay M J E 1964 Smoothing and differentiation of data by simplified least squares procedures Analytical Chemistry **36** 1627-39

[11] Hamming R W 1983 Digital Filters 2nd ed.(Englewood Cliffs, NJ: Prentice-Hall)

[12] Ziegler H 1981 Properties of digital smoothing polynomial (DISPO) filters Applied Spectroscopy **35** 88-92

[13] Lei K F, Lee K F and Lee M Y 2012 Development of a flexible PDMS capacitive pressure sensor for plantar pressure measurement *Microelectronic Eng.* **99** 1-5

[14] Fuard D, Tzvetkova-Chevolleau T, Decossas S, Tracqui P and Schiavone P 2008 Optimization of poly-di-methyl-siloxane (PDMS) substrates for studying cellular adhesion and motility *Microelectronic Eng.* **85** 1289-93

[15] Lotters J C, Olthuis W, Veltink P H and Bergveld P 1997 The mechanical properties of the rubber elastic polymer polydimethylsiloxane for sensor applications *J.Micromech. Microeng.* **7** 145-47

[16] Dobrzynska J A and Gijs M A M 2013 Polymer-based flexible capacitive sensor for three-axial force measurements *J.Micromech. Microeng.* **23** 015009

[17] Guo Q, Suster M A, Surapaneni R, Mastrangelo C H and Young D J 2013 High-performance interface electronics system for a 13 × 13 flexible biomechanical groung reaction sensor array achieving a gait ground velocity resolution of 100μm/sec *IEEE Sensors J.* **PP** 1,1,0

[18] Bebek O, Suster M, Rajgopal S, Fu M J, Huang X, Cavusoglu M, Young D J, Mehregany M, Van Den Bogert A and Mastrangelo C H 2010 Personal navigation via high-resolution gait-corrected inertial measurement units Instrumentation and Measurement, IEEE Transactions on **59** 3018-27

[19] Bebek O, Suster M, Rajgopal S, Fu M J, Huang X, Cavusoglu M, Young D J, Mehregany M, Van Den Bogert A and Mastrangelo C H 2010 Personal navigation via shoe mounted inertial measurement units Proc. of the IEEE/RSJ International Conference on Intelligent Robots and systems (IROS) , Taipei, Taiwan 1052-58

CHAPTER 6

CONCLUSION

In this work, we presented different design considerations, fabrication schemes and sensor characterization to achieve highly reliable FTIs. The developed FTI were based on a capacitive sensing scheme and the prototype FTIs consisted of an array of 169 sensing sites fabricated by advanced microfabrication procedures. We also presented the FTI integration with an in-house developed readout circuit to achieve in-depth FTI analysis. The evolution of various design criteria to achieve both high pressure and high shear sensitivities, fabrication methods to make the FTI highly reliable and FTI characterization using testing stations and developed software tools have been discussed.

The initial design implemented multiplexing scheme while maintaining high-resolution and the FTI flexibility. The fabricated FTI demonstrated the capability to measure both pressure and shear simultaneously. Various materials to fabricate the FTI have been successfully evaluated for different fabrication schemes and the shortcomings of each method were carefully studied. Improvements to fabrication schemes have been proposed and implemented to achieve a functional FTI. The design showed promising results for simultaneous normal stress and shear stress loading of the FTI with measured pressure and shear sensitivities of 0.58/MPa and 0.052/MPa, respectively. The FTI

evidently demonstrated lower shear sensitivity compared to the pressure sensitivity. To overcome this problem, significant design modifications were required for the FTIs to achieve higher shear sensitivity.

An FTI design with the implementation of multifingered electrode arrays was proposed as a viable solution to the lower shear sensitivity. The multifingered structures theoretically proved to enhance the shear sensitivity by a factor of four (number of fingers) while maintaining pressure sensitivity. Measurement data from the successfully fabricated multifingered FTI evidently demonstrated improved shear sensitivity (~3-4 time improvement) from the previous version. The measured pressure and shear sensitivities of the multifingered FTI were 0.64/MPa and 0.16/MPa, respectively. Despite the improved sensitivity, the electrical interconnects illustrated failure mode in the form of metallization issues that occur during the first few hundred deformation cycles (loading and unloading the cell). The metallization issues occurred due to the localized expansion of PDMS at the boundary of surface that applied the load.

Concerns regarding the durability of the fabricated FTI were overcome by the implementation of liquid-metal in a microfluidic channels. The conductivity and fluidity of the liquid-metal proved to be a reliable solution for FTIs under stress. During sensor deformation due to extreme mechanical stress on the FTI, liquid-metal could maintain the continuity of the electrical interconnects by reflowing in the channel after the stress was released. The measured pressure and shear stress sensitivities of this scheme were 0.74/MPa and 0.22/MPa, respectively (comparable to sensitivities of 0.64/MPa and 0.16/MPa measured from the multifingered structure). Despite being highly reliable and sensitive, the complicated alignment procedure hampered its potential as an alternative to

other FTI designs. Furthermore, electrical connection to the liquid-metal involved insertion of metal wires into the microholes and posed a failure mode (due to moving electrical connections).

A new overhauled design employing floating comb-electrodes was proposed to address the durability issue and present a successful replacement to the liquid-metallization scheme. Each sensing cell of this design consisted of a combed drive and sense electrodes in the FPCB and floating electrodes placed at an offset on an elastomeric dielectric material spin-coated over the FPCB. The fabrication scheme designed to develop this FTI presented the advantage of connecting it effortlessly to the readout circuitry and customized software. This was due to the ability to form a FCC connection at the circuit end of the FTI. The normal and shear stress sensitivities for the FTI were 0.38/MPa and 79.5/GPa, respectively. The minimum resolvable object displacement and minimum detectable microvelocity measured by the FTI were as low as 60 μm and 100 μm/s, respectively. The FTI was also successfully used to capture pressure contours during a regular walk and points of minimum velocity were obtained for each step during the walk. This system has proved to be a suitable candidate for detail measurements of reaction forces in gait analysis and has the potential to be used for contact sensing and intelligent gripping in robotics.

The FTIs need extensive analysis on fringing capacitance between the floating electrodes and the drive and sense electrodes. Electrical and finite element simulation should be performed to better understand the effects of load application on the fringing capacitances in the FTI. The current setup does not accommodate hysteresis analysis of individual sensing cells in the FTI. An experimental setup needs to be constructed to

analyze hysteresis in the FTI. Also there is a large scope for use of wide-ranging soft elastomers (such as spinable latex) that can replace PDMS to achieve more linear stress-strain curves. Extensive material investigation is required to find such a suitable alternative to PDMS. Shielding the FTI from external paracitics is critical and needs to be addressed with extensive analysis. Such shielding layers can also double as a protective layer to the floating electrodes. With such a large scope to improve the performance of the FTI by the above-discussed modifications and its current caliber to achieve simultaneous measurements of pressure and two dimensional shear, flexibility and reliability, the FTI can outperform all currently available technology.

APPENDIX A

INSTRUCTIONS FOR EXPERIMENTAL SETUP

In Chapter 5 of this work, we presented two different experimental setups to characterize normal stress on the entire FTI and shear stress on individual sensing cells of the FTI (in Section 5.5). The experimental setup also facilitates the detection of microdisplacements and microvelocities of objects rolling on top of the FTI. The experiments performed using the setup include measurement of static pressure (in which pressure is continuously increased by a small soft ball on top of the FTI) , rolling ball pressure (a quantified pressure is applied on the ball which then rolls from one end to the other end of the FTI) and shear measurement (a static load is applied on the GRSC array and the array is set in motion on a movable stage). Detailed instructions on how to operate the stepper motor and the load-cells to achieve the experiment is discussed in this Appendix.

A.1 Software installation

A.1.1 Phidgets drivers installation

The single-axis stepper motor (ET-100-1, Newmark Systems, Inc, USA) is operated using the Phidget stepper motor control board (assembled in a black plastic box as

shown in Figure A.1). Before connecting the stepper motor control board to the PC, installation of the Phidgets drivers that are available in the Phidget webpage (http://www.phidgets.com/drivers.php) is necessary. After installation of the drivers, the control board can be used to control the motion of the stepper motor using an executable program (Stepper-full.exe) developed in-house described in Appendix B.

A.1.2 Load-cell drivers/software installation

In order to measure the pressure applied on the rolling ball using the "Loadstar Sensors Type RSP1 pressure sensor," LoadVUE program should be installed. The installation files are provided by the load-cell vendor (Loadstar Sensor, USA). Figure A.2 shows the installed program to display the applied load. First, the applied load is converted to stress information (load per unit area of contact of the object used to apply the stress).

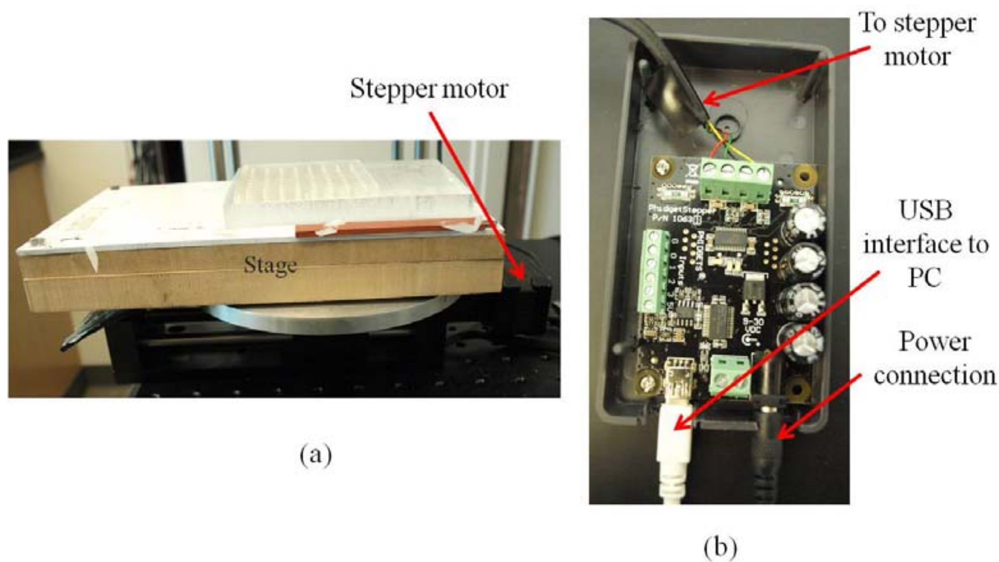

Figure A.1. Stage and stepper motor control. (a) Stepper motor with the stage fixed on the top. (b) Phidget stepper motor control board.

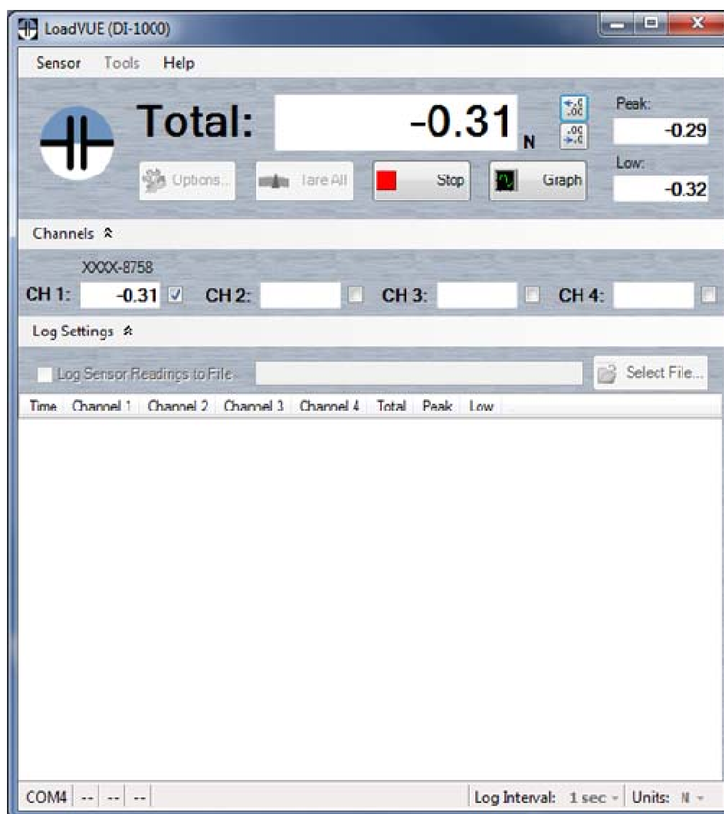

Figure A.2. Program to display the applied load using the load-cell.

A.1.3 Beagle and Aardvark I^{2}C/SPI cards drivers installation

Aardvark and Beagle cards are used to provide a start pulse (for the ASIC chip and the crystal oscillator on the readout circuit) and acquire the data (from the ASIC chip), respectively. Prior to connecting the cards to the PC, the drivers for these cards should be installed (the drivers are available from compact-discs provided by vendor Total Phase, USA). Dislin drivers are also needed to ensure proper working of the readout system and the associated software (Array Scan.exe). The Dislin drivers provide high level libraries of subroutines and functions that display the data using the in-house developed software (Array Scan.exe). These drivers are freeware and available from (http://dislin.softpedia.com/).

A.2 Load-cell software instructions to display applied load

Applied load is measured by the load-cell and displayed by the software DI-1000 LoadVUE. Following are the instructions for the software to display/record the measured load:

1. Connect the RSP1-050M-A*C01 (connected to the load-cell) to the PC using a USB connector.

2. Run the program "LoadVUE" that you installed using Section A.1.2. The program will complain if the sensor is not connected to the PC.

3. The bold "Total:" label shown in Figure A.2 represents the pressure applied on the sensor. The default units for the applied load is pounds (lb) and these units can be changed to Kg, N, kN, g or Oz. by clicking on the "Options..." button under the "Total " label.

4. Click on "Start" button to start the measurement. If the no-load value of the sensor is not zero, reset the sensor by clicking on the "Stop" button and then the "Tare All" button. Clicking on the "start" button now will display zero when there is no load applied on the sensor. Make sure the sensor is under no pressure when clicking on the "Tare All" button. Clicking on "Tare all" when a load is applied will also reset the value to zero and may result in obtaining the wrong load data.

5. To display a graph with time vs pressure, click on the "Graph" button. This will display a graph on a different window. You may choose to start and stop measurements directly from that window.

6. If you wish to save the measured values to a .CSV file, you may do so by checking the box "Log Sensor Reading to File" under the "Log Settings" dropdown menu (which is always displayed).

Further understanding of the software can be obtained from the "Help" Section of the software.

A.3 Controlling the motion of the stepper motor

The single-axis stepper motor (ET-100-1, Newmark Systems, Inc, USA) is operated using the Phidget stepper motor control board. The details of the in-house developed control to the stepper motor (Stepper-full.exe) are provided in Appendix B. Instructions to control the motor are provided as follows:

1. Connect power to the Phidget stepper motor control board and then connect the USB connector from the board to the PC (on which the drivers were installed).

2. Run the Stepper-full.exe application from windows operating system (developed in Appendix B).

3. Under the tab Set Velocity, motor status will provide information on whether or not the motor is successfully connected to the PC. If the status shows "True," as shown in Figure A.3, the motor is connected and "false" implies the motor is not connected.

4. If false is displayed, please check the connections and driver installations, disconnect the USB connector, close the program, connect the USB and rerun the program.

Figure A.3. Console of the stepper motor control program (stepper-full.exe).

5. Velocity of the motor in micron/second can be set by entering a value (less than 40000) and clicking the "Set Value" button. This will set the motor speed and initialize the motor in the stage.

6. Make sure the stage is about in the center of the screw (on which the stage moves) before articulating the stage.

7. To articulate the stage, click on the first button "Move Motor." This will move the motor from the center to one end of the screw it is moving.

8. Once the motor is at one of the ends of the stage, click on the second "Move Motor" button. This will move the stage to the other end of the screw.

9. Click on the "Initial Position" button to bring the stage to the initial position (which is at the center of the screw).

10. Clicking on any articulating buttons will move the stage to either end or to the initial position. Before exiting the program, make sure the stage is at the center of the screw.

Please make sure the stage is at the center position before disconnecting the USB connector or disconnecting power to the "Phidget Stepper Motor Control Board."

A.3.1 Bringing the stage to the center of the screw (if it is at either end)

If the user exited the program when the stage is at either end of the screw, restart the program, set the velocity value to 20000 and click the first or the second articulating buttons (first "Move Motor" second "move motor" or "initial position" button are called the articulating buttons). The user chooses the first or second button depending on the direction of the motion required to bring the stage to the center. Once the stage is at the center of the screw, set a different velocity value that is required and click on the "Set Value" button to initialize the stage again or exit the program.

A.3.2 Bringing the stage to the center of the screw (if it is not at either end or the center)

If the user exited the program or the program crashed when the stage is not at either ends of the screw, restart the program, set the velocity value to 15000 and click the first or the second articulating buttons. Disconnect the USB connector from the PC when you

think the stage is approximately at the center of the screw. (The user chooses the first or second button depending on the direction of the motion required to bring the stage to the center.) Once the stage stops at the center of the screw, restart the "stepper-full.exe" application.

A.4 Connecting the FTI to the readout circuitry

1. Writing the program into the microcontroller (ARM):
    - The user needs to install the IDE on a Win-XP computer from the link (http://leaflabs.com/docs/maple-ide-install.html)
    - Copy the program from Appendix C into the IDE and compile/write the program into the microcontroller.
    - When the IDE show “Searching for,” plug the ARM microcontroller board into the USB.
    - When the IDE show “Done,” the program has been successfully written into the microcontroller.
    - Unplug the microcontroller and replug it into a USB to power the ARM board.
2. Connecting the power supply and Aardvark/Beagle cards to the readout circuit:
    - Use a DC source to generate a 3.3V voltage and connect to the setup through a BNC cable.
    - Plug the USB cable of the microcontroller into a computer (to power the microcontroller).

- Connect the Beagle and Aardvark cards to the PC. The other ends of the cards consist of white flexible cables. These cables should be connected to the readout circuit at locations shown in Figure A.4.

3. Connecting the FTI to the readout circuit (via flat flex connector):

- Make sure the flex-cable of the FTI with gold connector is clean.
- With the gold connectors facing down, insert the cable straight into the 60 pin flat-flex connector and lock down the connector (using the flip-lock mechanism).
- Make sure the cable is connected properly.

A.5 Scanning the FTI

The array scan console application to capture data is built using the source files in Appendix D and/or Appendix E. Data are first captured using the source files from

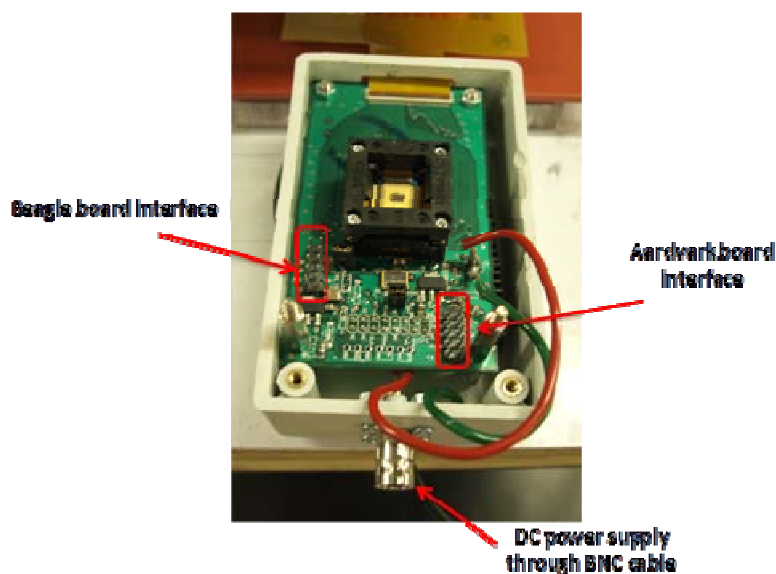

Figure A.4. Image of the readout circuit board indicating the connection interfaces for Beagle and Aardvark cards.

Appendix D.1. The captured data consist of both voltage changes from pressure and shear. These voltage data are mapped in 3-D to display the pressure and shear stress applied on the FTI using Matlab programs from Appendix D.2 and Appendix D.3, respectively.

Only pressure-related voltage data can also be displayed using the console application built by the source files from Appendix E. The program can, however, capture and save voltage changes pertaining to pressure and shear stresses in a .txt file. The instructions for using the console application built using source files from Appendix E are as follows:

- Before executing the program, make sure the power supply and the Beagle and Aardwark cards are properly connected to the readout circuit (shown in Figure A.4). Also make sure the microcontroller power (from USB) and the USB interfaces from the Beagle and Aardvark cards are connected to the PC. The user can make sure if the connections are successful by executing the console application. If MS-DOS prompt showing " '0' Beagle and '0' Aardvark devices found" appears, connections are incorrect. Disconnect all the cables and repeat Section A.4.
- Successful execution of the program will open a DOS prompt and a console as shown in Figure A.5.
- Before using the console, the microcontroller should be reset. This can be done by unplugging the USB cable to the microcontroller board and replugging it back to the PC.
- After resetting the microcontroller, Under the "Frame + Display" label, check the box "press here for data plot."

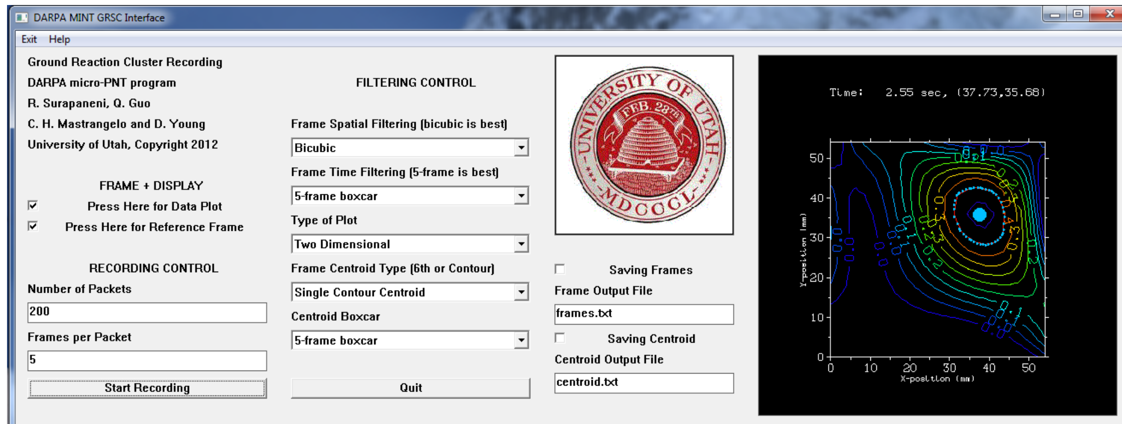

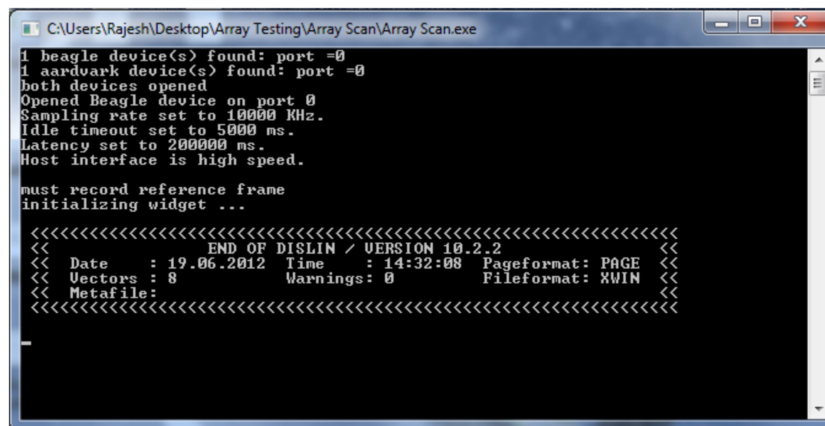

Figure A.5. Images of the array scanning program showing the console and DOS prompt.

- Make sure no load is applied on the FTI and then check the box "Press here for reference frame." Once the reference frame is obtained, "Fetching reference frame...

  Done

  Reference Voltage[1] = -0.2018"

  is displayed on the DOS prompt window. Proceed to the next step if you see this. Else the program complains that no reference frame was captured.

- Recording controls are chosen based on the time taken to conduct a test (higher "number of packets" are required for slow rolling pressure measurement, which is discussed later).
- Filtering controls are chosen depending on the filters required for plotting the graph (Best filters are mentioned beside each control. Choosing them will provide better plots and results).
- The frames data can be saved to a .txt file for further interrogation by checking the box " Saving Frames" and choosing a name for the file.
- The data for centroid of the applied load can be saved to a txt file for further interrogation by checking the box " Saving Centroid" and choosing a name for the file.
- The data recording commences only after clicking the "Start Recording" button. The plot is displayed in the console, as shown in Figure A.5.

APPENDIX B

PHIDGET STEPPER MOTOR CONTROLLER PROGRAM

//The following program is added to the source file and the corresponding form.CS is built as per Figure B.2

```
using System;
using System.Collections.Generic;
using System.ComponentModel;
using System.Data;
using System.Drawing;
using System.Text;
using System.Windows.Forms;
using Phidgets; //Needed for the Stepper class, Phidget base classes, and the PhidgetException class
using Phidgets.Events; //Needed for the Phidget event handling classes

namespace Stepper_full
{
  public partial class Form2 : Form
  {
    private Stepper stepper; //Declrea a Stepper object
    private ErrorEventBox errorBox;
    public Form2()
    {
      InitializeComponent();
      errorBox = new ErrorEventBox();
    }

    // initilize the stepper object and hook the event handlers
    private void Form2_Load(object sender, EventArgs e)
    {
      //timer1.Tick += new EventHandler(timer1_Tick);

      // Declare a Stepper object
      stepper = new Stepper();

      // hook the basic event handlers
       stepper.Attach += new AttachEventHandler(stepper_Attach);
      stepper.Detach += new DetachEventHandler(stepper_Detach);
      stepper.Error += new ErrorEventHandler(stepper_Error);


      //open the Stepper object for device connections
      stepper.open();
```

```
        //get the program to wait for a stepper device to be attached
            stepper.waitForAttachment();

            //Set the max velocity to start the stepper motor moving until it hits
            //the goal position
            stepper.steppers[0].VelocityLimit = 0; //Max velocity
            stepper.steppers[0].Acceleration = stepper.steppers[0].AccelerationMax;        //ensure the value
is between the AccelerationMin and AccelerationMax
            stepper.steppers[0].TargetPosition = 0;
            // stepper.steppers[0].Engaged = true;
        }


        //Stepper attach event handler...populate the available fields and controls
        void stepper_Attach(object sender, AttachEventArgs e)
        {
            Stepper attachedStepper = (Stepper)sender;

            attachedTxt.Text = attachedStepper.Attached.ToString();

        }

        //Stepper Detach event handler...Clear all the fields and disable all the controls
        void stepper_Detach(object sender, DetachEventArgs e)
        {
            Stepper detachedStepper = (Stepper)sender;

            attachedTxt.Text = detachedStepper.Attached.ToString();

        }

        //Stepper Error event handler...Display the details of the error in a message box
        void stepper_Error(object sender, ErrorEventArgs e)
        {
            Phidget phid = (Phidget)sender;
            DialogResult result;
            switch (e.Type)
            {
                case PhidgetException.ErrorType.PHIDGET_ERREVENT_BADPASSWORD:
                    phid.close();
                    TextInputBox dialog = new TextInputBox("Error Event",
                        "Authentication error: This server requires a password.", "Please enter the password, or
cancel.");
                    result = dialog.ShowDialog();
                    if (result == DialogResult.OK)
                        openCmdLine(phid, dialog.password);
                    else
                        Environment.Exit(0);
                    break;
                default:
                    if (!errorBox.Visible)
                        errorBox.Show();
                    break;
            }
            errorBox.addMessage(DateTime.Now.ToLongDateString() + " " +
DateTime.Now.ToLongTimeString() + ": " + e.Description);
```

```
}
private void Form2_FormClosed(object sender, FormClosedEventArgs e)
{
   stepper.Attach -= stepper_Attach;
   stepper.Detach -= stepper_Detach;
   stepper.Error -= stepper_Error;
   //run any events in the message queue - otherwise close will hang if there are any outstanding
events
   Application.DoEvents();

   if (stepper.Attached)
   {
      for (int i = 0; i < stepper.steppers.Count; i++)
      {
         stepper.steppers[i].Engaged = false;
      }
   }
   stepper.close();
}
//Parses command line arguments and calls the appropriate open
#region Command line open functions
private void openCmdLine(Phidget p)
{
   openCmdLine(p, null);
}
private void openCmdLine(Phidget p, String pass)
{
   int serial = -1;
   int port = 5001;
   String host = null;
   bool remote = false, remoteIP = false;
   string[] args = Environment.GetCommandLineArgs();
   String appName = args[0];
   try
   { //Parse the flags
      for (int i = 1; i < args.Length; i++)
      {
         if (args[i].StartsWith("-"))
            switch (args[i].Remove(0, 1).ToLower())
            {
               case "n":
                  serial = int.Parse(args[++i]);
                  break;
               case "r":
                  remote = true;
                  break;
               case "s":
                  remote = true;
                  host = args[++i];
                  break;
               case "p":
                  pass = args[++i];
                  break;
               case "i":
                  remoteIP = true;
                  host = args[++i];
```

```
                        if (host.Contains(":"))
                        {
                            port = int.Parse(host.Split(':')[1]);
                            host = host.Split(':')[0];
                        }
                        break;
                    default:
                        goto usage;
                }
            else
                goto usage;
        }
        if (remoteIP)
            p.open(serial, host, port, pass);
        else if (remote)
            p.open(serial, host, pass);
        else
            p.open(serial);
        return; //success
    }
    catch { }
usage:
    StringBuilder sb = new StringBuilder();
    sb.AppendLine("Invalid Command line arguments." + Environment.NewLine);
    sb.AppendLine("Usage: " + appName + " [Flags...]");
    sb.AppendLine("Flags:\t-n   serialNumber\tSerial Number, omit for any serial");
    sb.AppendLine("\t-r\t\tOpen remotely");
    sb.AppendLine("\t-s   serverID\tServer ID, omit for any server");
    sb.AppendLine("\t-i   ipAddress:port\tIp Address and Port. Port is optional, defaults to 5001");
    sb.AppendLine("\t-p   password\tPassword, omit for no password" + Environment.NewLine);
    sb.AppendLine("Examples: ");
    sb.AppendLine(appName + " -n 50098");
    sb.AppendLine(appName + " -r");
    sb.AppendLine(appName + " -s myphidgetserver");
    sb.AppendLine(appName + " -n 45670 -i 127.0.0.1:5001 -p paswrd");
    MessageBox.Show(sb.ToString(),       "Argument       Error",       MessageBoxButtons.OK,
MessageBoxIcon.Error);
    Application.Exit();
}
#endregion

private void label1_Click(object sender, EventArgs e)
{
}
private void SetVelocityButton_Click(object sender, EventArgs e)
{
    stepper.steppers[0].VelocityLimit = Convert.ToDouble(VelocityBox.Text) * 500.00 / 1000.00;
//corresponds to set value button
    stepper.steppers[0].Acceleration = stepper.steppers[0].AccelerationMax; //ensure the value is
between the AccelerationMin and AccelerationMax
    stepper.steppers[0].TargetPosition = 0;
    stepper.steppers[0].CurrentPosition = (long)0.95;
    stepper.steppers[0].Engaged = true;
}
private void MoveMotor1Button_Click(object sender, EventArgs e)
{
```

```
                stepper.steppers[0].TargetPosition = 7600; //corresponds to the first move motor button
            }
            private void MoveMotor2Button_Click(object sender, EventArgs e)
            {
                stepper.steppers[0].TargetPosition = -7600; //corresponds to the second move motor button
            }
            private void InitialPositionButton_Click(object sender, EventArgs e)
            {
                stepper.steppers[0].TargetPosition = 0; //corresponds to the initial position button
            }
            private void ExitButton_Click(object sender, EventArgs e)
            {
                stepper.steppers[0].VelocityLimit = 0; //Max velocity
                stepper.steppers[0].Acceleration = stepper.steppers[0].AccelerationMin; //ensure the value is
between the AccelerationMin and AccelerationMax
                stepper.steppers[0].Engaged = false;
                this.Close();
            }
            private void label2_Click(object sender, EventArgs e)
            {
            //corresponds to velocity text box
            }
        }
    }
```

Figure B.1. Image of Form.CS

APPENDIX C

PROGRAM FOR THE MICROCONTROLLER

```
// Copy this code into the IDE and compile/write the program into the microcontroller
int i;
int j;
void Data_Start(){
digitalWrite (35,HIGH);
}
void Data_End(){
digitalWrite (35,LOW);
}

void delay_v1(){
__asm__("nop\n\t");
__asm__("nop\n\t");
__asm__("nop\n\t");
__asm__("nop\n\t");
__asm__("nop\n\t");
__asm__("nop\n\t");
__asm__("nop\n\t");
__asm__("nop\n\t");
__asm__("nop\n\t");
__asm__("nop\n\t");
__asm__("nop\n\t");
__asm__("nop\n\t");
__asm__("nop\n\t");
__asm__("nop\n\t");
__asm__("nop\n\t");
__asm__("nop\n\t");
__asm__("nop\n\t");
__asm__("nop\n\t");
__asm__("nop\n\t");
__asm__("nop\n\t");
__asm__("nop\n\t");
__asm__("nop\n\t");
}
void delay_v2 (){
__asm__("nop\n\t");
__asm__("nop\n\t");
__asm__("nop\n\t");
}
void WriteHigh(){
```

```
__asm__("nop\n\t");
GPIOB_BASE->BSRR = BIT(11+16) | BIT(10);
delay_v1();
GPIOB_BASE->BSRR = BIT(11) | BIT(10);
delay_v2();
__asm__("nop\n\t");
}
void WriteLow(){
GPIOB_BASE->BSRR = BIT(11+16) | BIT(10+16);
delay_v1();
GPIOB_BASE->BSRR = BIT(11) | BIT(10+16);
delay_v2();
}
void end_Prog_CLK(){
GPIOB_BASE->BSRR = BIT(11+16) | BIT(10+16);
__asm__("nop\n\t");
__asm__("nop\n\t");
__asm__("nop\n\t");

}
void Prog_Write(){
digitalWrite(28, HIGH);
}
void Prog_Write_end(){
digitalWrite(28, LOW);
}

void setup() {
pinMode(D28, OUTPUT);
pinMode(D29, OUTPUT);
pinMode(D30, OUTPUT);
pinMode(27, PWM);
pinMode(35, OUTPUT);
}

void loop() {
//generating programming signal
Prog_Write();
WriteLow();

WriteLow();
WriteLow();
//00 for cv2adc
//01 for cv
//10 for adc
//
WriteLow();
WriteLow();
WriteLow();
WriteLow();
WriteLow();
//
//WriteLow();
//WriteLow();
//WriteLow();
//WriteHigh();
```

```
//WriteHigh();

//WriteHigh();
//WriteHigh();
//WriteHigh();
//WriteHigh();
//WriteHigh();

//MSB
//

WriteLow();
WriteLow();
WriteLow();
WriteHigh();
WriteHigh();
WriteLow();
// pad 5 ue 24
//MSB

end_Prog_CLK();
Prog_Write_end();
//delay(1);
//Data_Start();
//Timer3.resume();
while(1)
{
  delay(10000);
}
void Data_End();
}
```